

A study on the physical characteristics of  
quasi-2-day waves in the tropical atmosphere  
with global data analysis

(全球データ解析による熱帯大気準二日振動の  
物理特性に関する研究)

SUMI, Yukari  
(角 ゆかり)

A dissertation for the degree of Doctor of Science  
Department of Earth and Environmental Sciences,  
Graduate School of Environmental Studies,  
Nagoya University

(名古屋大学大学院 環境学研究科  
地球環境科学専攻 学位論文 博士 (理学))

2017



## Acknowledgments

I would like to express my deepest gratitude to my adviser, Prof. Hirohiko Masunaga, for his guidance, patience, generous support, and continuous encouragement throughout my study life. In the discussion with him, I learned how to think critically and how to write a scientific paper logically. His advice and comments always improve my research and lead me to the right direction. I am so lucky to receive guidance directly from him.

I would like to thank to my committee, Prof. Kazuhisa Tsuboki, Prof. Nobuhiro Takahashi, and Prof. Hatsuki Fujinami, for reading my thesis and giving me insightful comments and suggestions. Prof. Takahashi and Prof. Fujinami also provide me with meaningful comments in the laboratory seminar. I thank Dr. Fumie Akimoto, Dr. Hironari Kanamori, and Dr. Yoshiki Fukutomi for technical supports and giving me useful advice and comments in the seminars. Their kind words always help me.

I thank Ms. Tomoko Tanaka for her warmful support throughout my grad student life. I also thank all the members in Hydrospheric Atmospheric Research Center (HyARC) in Nagoya University for helping my everyday life in the laboratory. They always encourage me and tell me the interest of the atmospheric science.

The global-merged IR brightness temperature data were provided by the National Centers for Environmental Prediction (NCEP) Climate Prediction Center (CPC). The TRMM PR (2A25) datasets were provided by the Japan Aerospace Exploration Agency (JAXA). ECMWF ERA-Interim data were provided by ECMWF.

# Contents

<b>Abstract</b>	<b>7</b>
<b>1 Introduction</b>	<b>9</b>
1.1 Background	9
1.1.1 Tropical climatology	9
1.1.2 Tropical dynamics	12
1.2 Convectively coupled equatorial waves	13
1.2.1 Physical characteristics of CCEWs	13
1.2.2 Wave-convection coupling mechanism of CCEWs: vertical modes and tropospheric moisture	15
1.2.3 Mechanism of slowdown of CCEWs	19
1.2.4 Quasi-2-day wave	19
1.3 Theoretical background: equatorial waves	22
1.3.1 Model and basic equations	22
1.3.2 Dispersion relations of equatorial waves	23
1.3.3 Horizontal structure of equatorial waves	26
1.4 Theoretical background: vertical mode transform	28
1.4.1 Governing equations	28
1.4.2 Simplified governing equations and the vertical differential operator	30
1.4.3 The vertical mode transform	31
1.5 Outline of the thesis	34
<b>2 Data and Methodology</b>	<b>35</b>
2.1 Data description	35
2.1.1 Satellite data	35
2.1.2 Reanalysis data	36
2.2 Methodology	36
2.2.1 Spectral analysis	36
2.2.2 Filtering analysis	37
2.2.3 Definition of the peak of WIG wave	39
2.2.4 Composite analysis	40
2.2.5 Radon transform	40
2.2.6 Vertical mode	42

<b>3</b>	<b>Thermodynamic process of quasi-2-day wave</b>	<b>47</b>
3.1	Goal of this chapter . . . . .	47
3.2	Gross features of composite WIG waves . . . . .	47
3.3	MSE budget analysis . . . . .	49
3.3.1	Budget analysis . . . . .	49
3.3.2	Vertical structure of the budget terms . . . . .	51
3.3.3	Decomposition of advection terms . . . . .	52
3.3.4	Zonal wind effect . . . . .	56
3.3.5	Gross moist stability . . . . .	57
3.4	Discussion . . . . .	60
3.4.1	Comparison with the other CCEWs and MJO . . . . .	60
3.4.2	Comparison with 2 mode model . . . . .	61
3.4.3	Propagation characteristics of 2-day waves . . . . .	61
3.5	Summary . . . . .	62
<b>4</b>	<b>Vertical mode and effective stability of quasi-2-day wave</b>	<b>64</b>
4.1	Goal of this chapter . . . . .	64
4.2	Phase speed of composite WIG wave . . . . .	65
4.3	Vertical mode transform . . . . .	66
4.3.1	Vertical mode transform . . . . .	66
4.3.2	Phase speed of the vertical mode . . . . .	67
4.4	Effective static stability . . . . .	69
4.4.1	Definition of $\alpha_n$ . . . . .	69
4.4.2	Estimating of $\alpha_n$ . . . . .	71
4.5	Discussion . . . . .	74
4.5.1	The Doppler effects . . . . .	74
4.5.2	$\alpha_n$ versus $\tilde{\alpha}_n$ . . . . .	76
4.5.3	The reduced stability mechanism . . . . .	78
4.6	Summary . . . . .	79
<b>5</b>	<b>Summary</b>	<b>80</b>
<b>6</b>	<b>Supplement to theoretical background</b>	<b>82</b>
6.1	Shallow water equations . . . . .	82
6.2	Vertical mode transform of temperature, pressure velocity, and heating rate	84
6.2.1	Temperature . . . . .	84
6.2.2	Pressure velocity . . . . .	85
6.2.3	Heating rate . . . . .	85
6.3	Eigenvalue equation in discrete form . . . . .	86
6.4	Boundary conditions in discrete form . . . . .	88
6.5	Temperature, pressure velocity, and heating rate in discrete form . . . . .	88
6.5.1	Temperature . . . . .	88
6.5.2	Pressure velocity . . . . .	89
6.5.3	Heating rate . . . . .	90
6.6	Budget equations of DSE, moisture, and MSE . . . . .	91
6.7	Vertical MSE advection and a large-scale circulation . . . . .	92

**References**

# Abstract

In the tropics, moist convection is prominent during the year. Organized convective systems (cloud clusters) are constantly generated and brings a large amount of precipitation. The primary energy source of atmospheric motion is the latent heating from organized convection, which drives large-scale disturbances (equatorial waves). A large-scale equatorial wave coupled with convection (clouds and precipitation) is known as a convectively coupled equatorial wave (CCEW).

The present study focuses on the quasi-2-day waves which are the most fundamental element of the hierarchy of CCEWs. The 2-day waves are large-scale atmospheric disturbances moving westward near the equator with a period of about 2 days. Their dynamics is explained by that of the convectively coupled westward inertia-gravity wave (WIG wave). The relationship between moist convection and large-scale dynamics of the waves is examined by using satellite and reanalysis data. Convective peaks of the 2-day wave are detected by WIG filtering of infrared brightness temperature data, and various global data are composited around the peaks to extract the statistical properties. The present study consists of two parts as summarized as follows.

In the first part of the present study, the interaction between moist convection and large-scale dynamics is examined in the thermodynamic context. The thermodynamic properties of 2-day wave are analyzed using moist static energy (MSE), which is nearly conserved in moist adiabatic process. The column-integrated MSE budget is useful to diagnose MSE recharge-discharge process at work in association with the wave activity. Net change of the column MSE is explained by MSE advection due to a large-scale circulation and diabatic fluxes (radiative and surface heat fluxes). The recharge-discharge process of 2-day waves is investigated by calculating the budget terms from reanalysis data. MSE increases before the buildup of deep convection (recharge process) and decreases during and after the convection (discharge process). MSE variability is mainly dominated by the advection term, while radiative heating and surface heat fluxes make only a minimal contribution. The advection term is further separated into the horizontal (zonal and meridional) and vertical components. The horizontal advection is roughly in phase with the MSE tendency and is mainly accounted for by the zonal advection, where the amplitude of zonal advection is nearly the same as that of vertical advection. An increase of negative vertical advection associated with deep convection is remarkable, while that of positive vertical advection due to shallow convection is relatively smaller in amplitude. The advection terms are further separated into the mean and perturbation fields of wind and MSE to investigate the causes of variability of MSE advection. Vertical advection is found to be mainly dominated by a large-scale vertical motion of 2-day wave. Advection by the mean zonal wind across the perturbation MSE gradient gives the largest contribution to zonal advection, while this term plays little role in driving the

recharge-discharge process. As the easterly (westerly) mean wind becomes stronger, the amplitude of zonal advection is more larger (smaller) with that of vertical advection being nearly unchanged. From these results, it is suggested that MSE recharge-discharge process during the active phase of 2-day wave is mainly driven by the vertical advection due to the large-scale vertical motion. This result is qualitatively consistent with existing theoretical models of CCEW. To examine the relationship between large-scale circulation and convective intensity, normalize gross moist stability (NGMS) is adopted from the previous studies, defined as the ratio of MSE vertical advection to moisture vertical advection. NGMS decreases to 0 before deep convection. According to the development of deep convection, NGMS increases and reaches its maximum after the convective peak. This result is consistent with the previous study indicating that the temporal variability of NGMS is more prominent for the waves with short time scale such as 2-day waves.

As described above, the large-scale vertical motion plays an important role in modulating the thermodynamic properties of the 2-day wave. It is known that the large-scale dynamical field is well explained by a few vertical modes (congestus, deep, and stratiform modes). The deep mode (the first baroclinic mode) has a single-signed structure. The congestus and stratiform modes (the second and third baroclinic modes) have a dipole-like structure. Each dry vertical mode propagates fast but is known to be slowed down when coupled with convection. Hence, it is required to examine the role of the vertical modes to understand the propagation dynamics of 2-day waves, in particular the mechanisms controlling the phase speed.

In the second part of the present study, the slowing down mechanism of 2-day waves is examined focusing on the phase speed of vertical modes associated with the wave dynamics. Vertical mode transform analysis shows that the large-scale dynamical field of 2-day waves is well represented by the superposition of the first four modes. This result is qualitatively consistent with the known multi-mode model consisting of congestus, deep, and stratiform modes. Phase speed of moist vertical modes is estimated by using their mode transform coefficient, showing that different modes propagate at a similar phase speed. It is suggested that the 2-day waves are only weakly dispersive. In the theoretical model, a slowdown of the first mode is explained by a reduction of effective static stability ( $S_e$ ) due to latent heating, which is known as the effective stability mechanism. The present study, based on a simple theoretical consideration, derives a diagnostic equation to evaluate the relationship between a degree of reduction of  $S_e$  and that of equivalent depth of vertical mode. The degree of reduction of  $S_e$  is estimated as a degree of partial cancellation of diabatic cooling due to upward motion by latent heating ( $\alpha_n$ ). The decrease in  $S_e$  becomes larger in the lower mode than in the higher mode, partially explaining the weak dispersiveness of the moist vertical modes. The relationship between  $S_e$  and reduced equivalent depth is examined for each vertical mode by using the above diagnostic equation. In the first mode, as expected from the theoretical model, the shallow equivalent depth is qualitatively explained by the reduction of  $S_e$ . In the higher modes, however, discrepancy from the theoretical prediction becomes large, implying that the effective stability mechanism alone is not sufficient to explain the slowdown of those modes. This discrepancy remains even with the Doppler effect considered. The discrepancy may be associated with uncertainties in the estimation of  $\alpha_n$ , where  $\alpha_n$  is assumed to be a time-independent and vertically uniform by design. These assumptions are valid for the first mode, while in need of improvements for the higher modes.

# Chapter 1

## Introduction

### 1.1 Background

#### 1.1.1 Tropical climatology

The tropics are a region of largest solar radiation of the earth, where high tropospheric temperature and humidity are observed during the year. The tropics play an important role to maintain the global energy balance. Figure 1.1 shows the energy balance at the top of the atmosphere (TOA). Absorbed solar radiation is largest in the tropics and smaller in the higher latitude. Outgoing longwave radiation (OLR) is lowest in the polar regions, and . The net radiation at TOA, sum of solar radiation and OLR, is positive in the tropics and negative in the higher latitudes. Since the annual-mean net flux at TOA is balanced by a transport of horizontal energy flux, the net radiative heating (cooling) is transported poleward (equatorward) by the flux of energy in the atmosphere and the ocean, which leads to a reduction of temperature gradient.

The solar energy absorbed by the land-sea surface warms the tropical atmosphere, where deep cumulus clouds with cloud top height near the tropopause frequently arise (Fig. 1.2). This is consistent with that OLR is slightly lower in the tropics than in the subtropics due to the deep cloudiness (Fig. 1.1). Figure 1.2 illustrates the trimodal structure of tropical convection found by Johnson et al. (1999): shallow cumulus, cumulus congestus, and deep cumulus. These clouds are known to be associated with precipitation activity in the tropics. Figure 1.3 shows horizontal distribution of the precipitation climatology obtained from the Tropical Rainfall Measuring Mission (TRMM) Precipitation Radar (PR). The strong precipitation is observed in the Indo-Pacific warm pool region, Maritime Continent, and Amazon. The elongate precipitation area near the equator is called the intertropical convergence zone (ITCZ), where the low-level wind converges into the region (Fig. 1.4a) and the air is rising (Fig. 1.4b). Horizontal distributions of precipitation and sea surface temperature (SST) roughly resembles each other (Fig. 1.4c,d). It is well known that precipitation monotonically increase with respect to SST up to about 27-29°C, while the monotonic relationship fails beyond the threshold (e.g., Graham and Barnett 1987; Waliser et al. 1993; Zhang 1993).

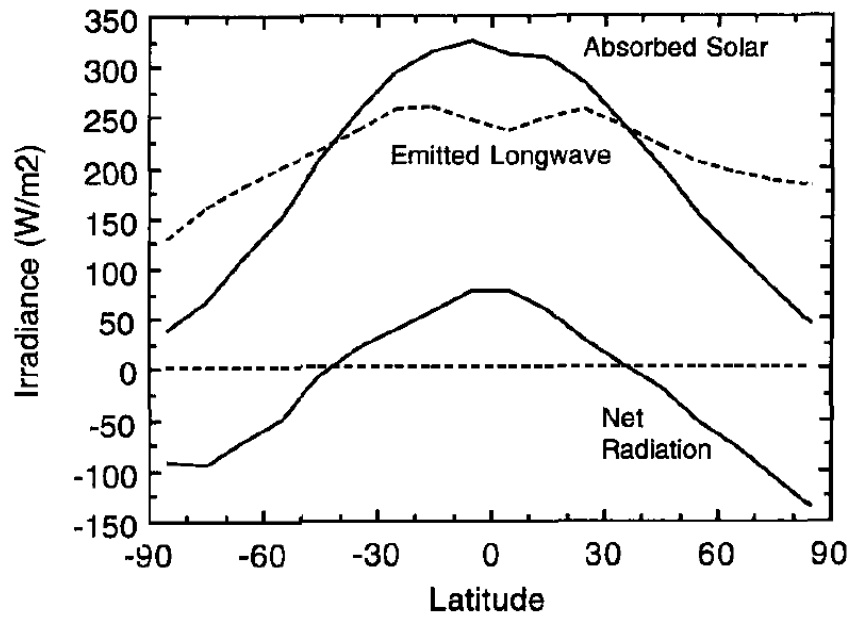


**Fig. 1.1:** Annual-mean absorbed solar radiation, OLR, and net radiation averaged around latitude circles. From [Hartmann \(2015\)](#).

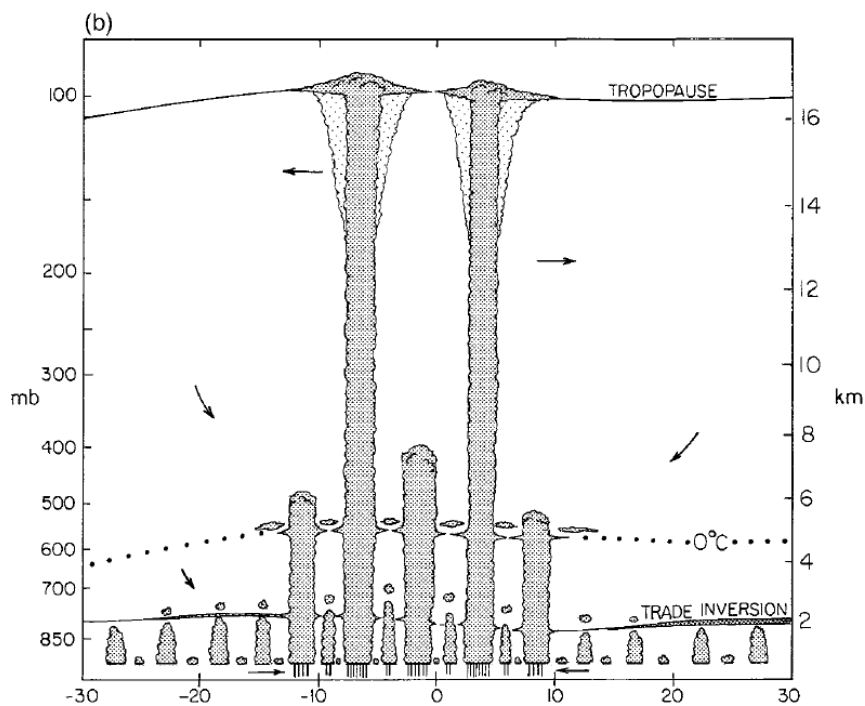


**Fig. 1.2:** A schematic of north-south slice through the tropical atmosphere. From [Johnson et al. \(1999\)](#).

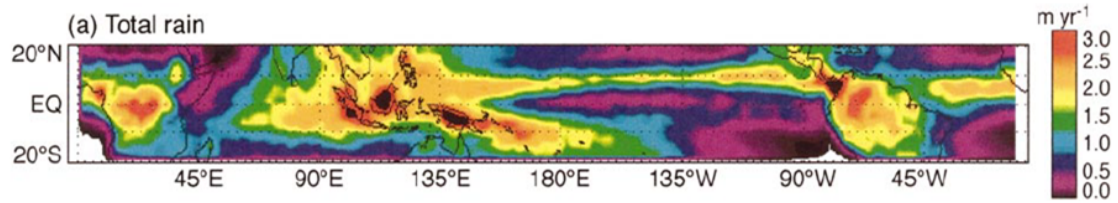


**Fig. 1.3:** The PR total rain based on a  $2.5^\circ$  grid averages for 1998-2000. From [Schumacher and Houze Jr \(2003\)](#).

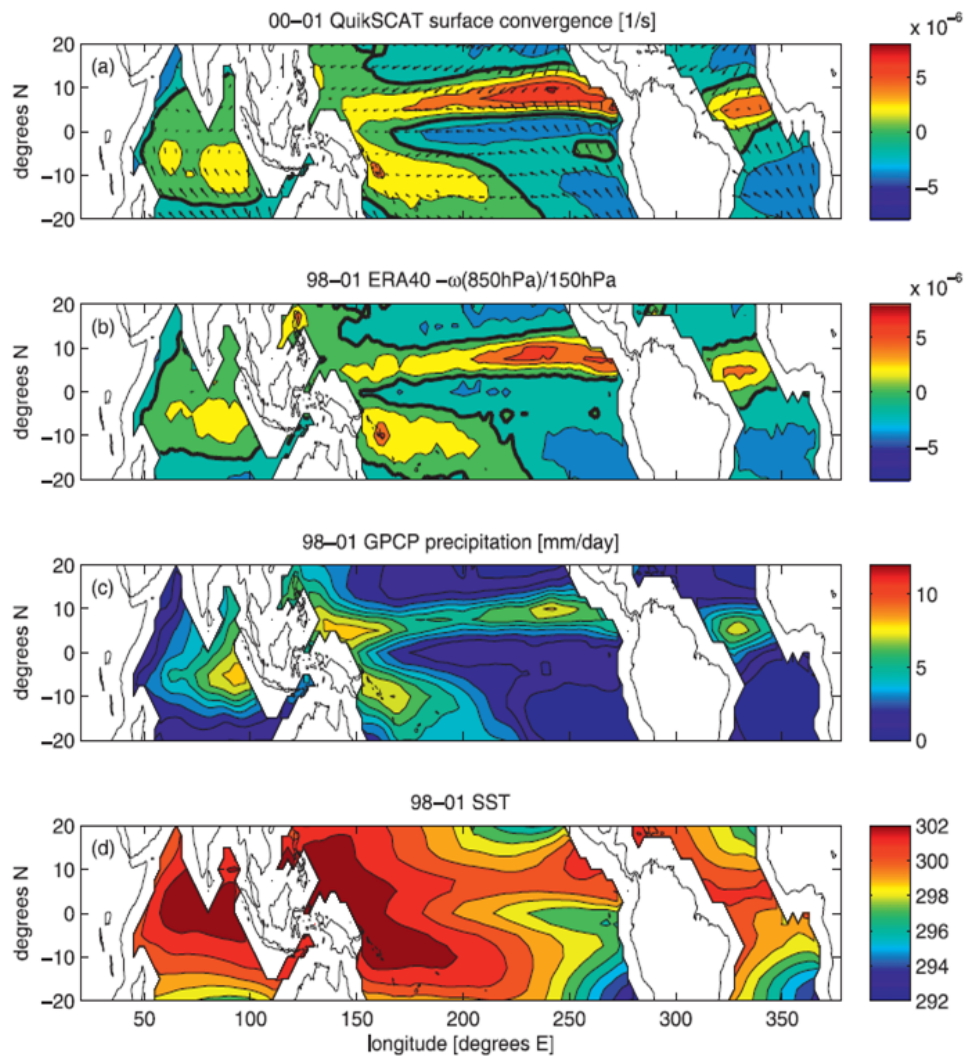


**Fig. 1.4:** (a) 2000-01 surface convergence from QuikSCAT with contours of  $2 \times 10^{-6} \text{ s}^{-1}$ , (b) 1998-2001 ERA-40 pressure velocity, (c) GPCP precipitation, and (d) ERA-40 SST. From [Back and Bretherton \(2009\)](#).



## 1.2 Convectively coupled equatorial waves

### 1.2.1 Physical characteristics of CCEWs

It is well known that organized convective cloud systems (cloud clusters) are frequently observed in the tropics. They have meso- to synoptic-scale time period and structure. A longitude-time cross section of infrared temperature reveals that the convective cloud systems propagate in various directions (Fig. 1.6). These systems are often associated with the convectively coupled equatorial waves (CCEWs) and the intraseasonal oscillation which control the precipitation variability in the tropics and have a large impact on the global circulation in the atmosphere. The horizontal structures and dispersion characteristics of CCEWs are qualitatively explained by the dry equatorial waves, Kelvin, equatorial Rossby, mixed Rossby-gravity, and inertigravity waves, derived from shallow water equations linearized in equatorial  $\beta$  plain by Matsuno (1966) (see section 1.3). However, the physical characteristics of the CCEWs are more complicated than expected from shallow water theory because of their moist processes. A understanding of CCEWs still remains a challenging problem in the atmospheric science.

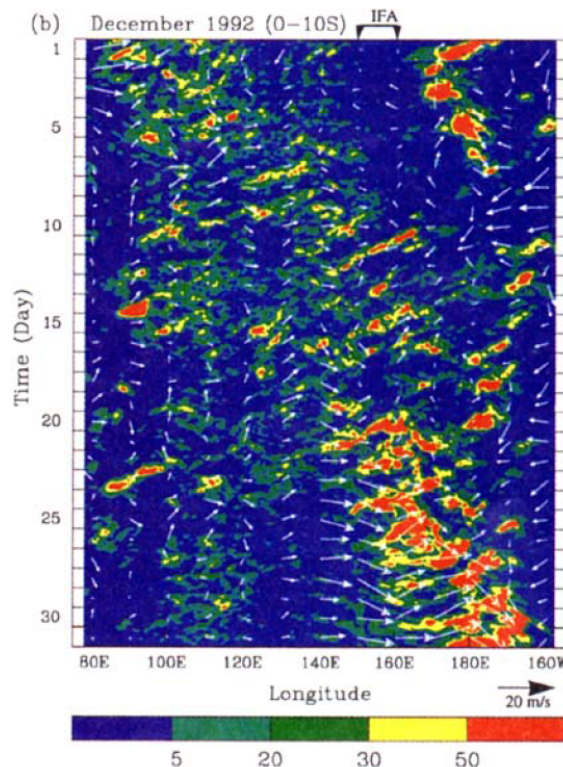


**Fig. 1.6:** A longitude-time cross section of infrared temperature (IR) lower than 208 K for December 1992. IR data at each longitude are averaged in meridional band between  $0^\circ$  and  $10^\circ$ . The colors are the number of pixels colder than 208 K. Red colored area corresponds to convective active area. Vectors are 850 mb total wind. From Chen et al. (1996).

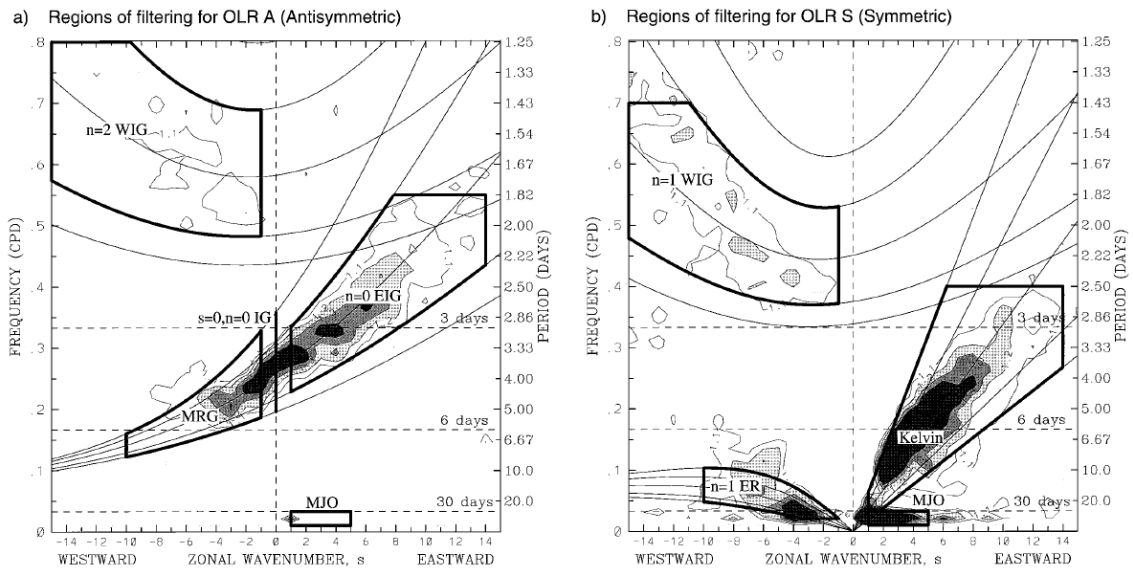


**Fig. 1.7:** The antisymmetric and symmetric OLR power divided by the red-noise background. Thin lines are the dispersion relationships of equatorial waves for the equivalent depths of 8, 12, 25, 50, and 90 m (Matsuno 1966). Thick boxes are the filters to identify the waves. From Wheeler and Kiladis (1999).

Based on various satellite observational data, it is revealed that the power spectrum of tropical convection, using cloudiness, precipitation, and column water vapor, is well explained by the theoretical dispersion relation of the waves with an equivalent depth of about 12-50 m (Takayabu 1994a; Wheeler and Kiladis 1999; Wheeler et al. 2000; Roundy and Frank 2004; Kiladis et al. 2009; Yasunaga and Mapes 2012, and many others). Figure 1.7 shows that the power spectrum of CCEWs peaks around the dispersion curves with the equivalent depth of 12, 25, and 50 m. It is indicated that the CCEWs have a slower phase speed (or shallower equivalent depth) than their dry counterparts. For example, the equivalent depth of 12-50 m is much shallower than that of the first vertical mode ( $\sim 200$  m). While the shallow equivalent depth of 12-50 m is widely observed among various CCEWs, what decreases the equivalent depth has yet to be clarified. As will be described in section 1.2.3, the slowdown of the waves is considered to be related to the coupling between convection and the wave dynamics. It is also well known that CCEWs have a self similarity among different space-time scales (e.g., Kiladis et al. 2009): 1) dynamical fields (e.g., winds and geopotential) represent a baroclinic structure where the anomalies vertically tilts with height. 2) Temperature field has a boomerang-like structure. 3) The convective life cycle consists of distinct developing stages associated with progress in the representative cloud types from shallow cumuli to deep convective and stratiform clouds. 4) Column moisture increases in the lower to middle troposphere preceding convective peak of CCEWs. The above features are also seen in Madden-Julian Oscillation (MJO) which is a synoptic-scale disturbance moving eastward with a period of about 30-90 days at a speed of  $\sim 5 \text{ m s}^{-1}$  (e.g., Madden and Julian 1971 1972).

## 1.2.2 Wave-convection coupling mechanism of CCEWs: vertical modes and tropospheric moisture

To better understand the physical characteristics of CCEWs, it is important to examine a mechanism of the interaction between convection and a large-scale motion of the waves. The wave-convection coupling mechanism of CCEWs has been proposed in different ways (see good review in [Wheeler et al. 2000](#); [Straub and Kiladis 2003](#); [Kiladis et al. 2009](#)). In past 15 years, theoretical models of the coupling mechanism have been developed with focus on multiple vertical modes having different heating profile ([Mapes 2000](#); [Majda and Shefter 2001](#); [Majda et al. 2004](#); [Khouider and Majda 2006a](#); [Kuang 2008b](#)). Figure 1.8 shows idealized structure functions of vertical velocity (Fig. 1.8a) and heating rate (Fig. 1.8b). The first baroclinic mode (or deep convective mode) has a single-sign structure and the second baroclinic mode (or stratiform mode) has a dipole-like structure. The shallow convective mode has a single peak between the boundary layer and the lower troposphere. As will be mentioned in section 1.4, the higher mode has faster phase speed. These modes are sometimes used to explain the coupling mechanisms as shown below.

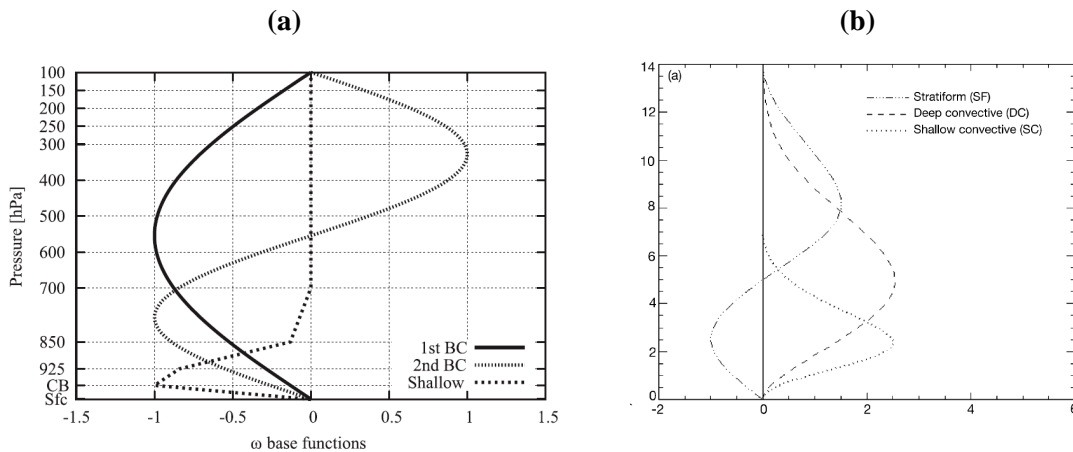


**Fig. 1.8:** (a) Idealized structure functions of vertical velocity for the first baroclinic, the second baroclinic, and shallow modes. From [Masunaga and L'Ecuyer \(2014\)](#). (b) Idealized structure functions of heating rate for stratiform, deep convective, and shallow convective modes. From [Schumacher et al. \(2004\)](#).

A “stratiform instability” mechanism is originally proposed by [Mapes \(2000\)](#), where a lower tropospheric cooling by the second baroclinic mode decreases convective inhibition (CIN) and could give rise to an unstable growth working together with upper-tropospheric heating in stratiform precipitation (Fig. 1.9). The vertical mode with shallower equivalent depth (e.g., the second mode) is considered to set slower phase speed (see section 1.2.3 for more detail). [Kuang \(2008b\)](#) proposed the “moisture stratiform instability” mechanism that relies on a moisture increase in the middle troposphere preceding deep convection as a driver of CCEWs, where shallow updraft due to the higher mode (e.g., congestus mode) increases the tropospheric moisture (Fig. 1.10).

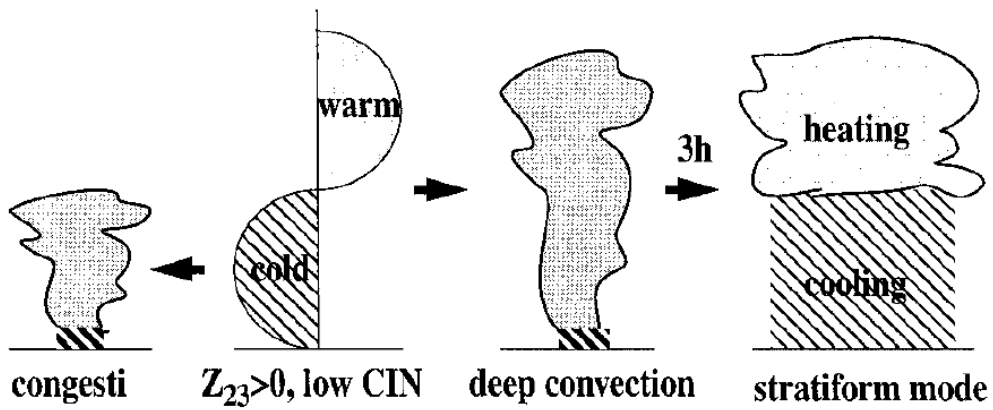


**Fig. 1.9:** A schematic of stratiform instability mechanism. From [Mapes \(2000\)](#)

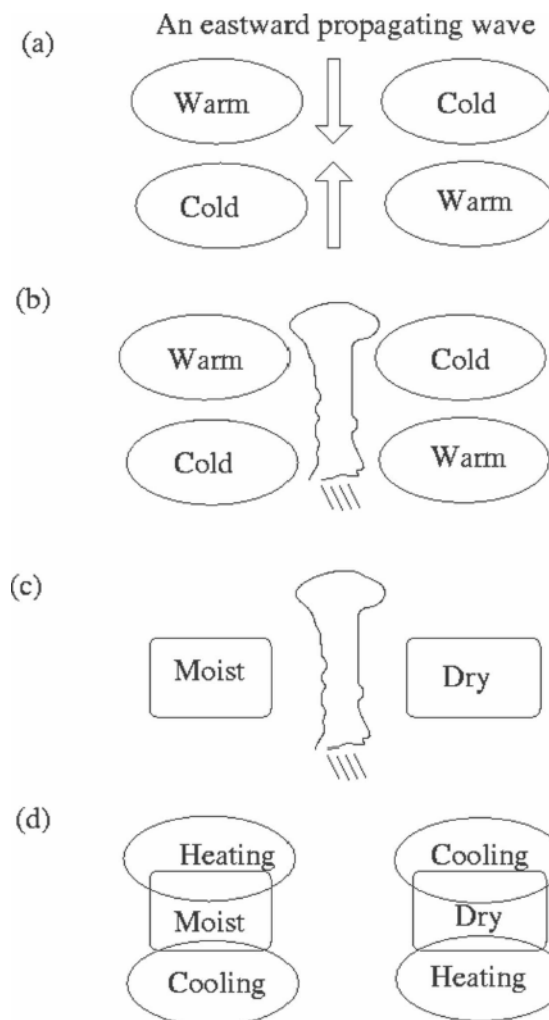


**Fig. 1.10:** A schematic of moisture stratiform instability mechanism. From [Kuang \(2008b\)](#)

The concept of the possible coordination of the multiple vertical modes has been extensively explored in the literature in the context of CCEWs. The vertically tilted top-heavy structure is captured by the superposition of a few baroclinic modes (Straub and Kiladis 2003; Haertel and Kiladis 2004; Peters and Bretherton 2006; Tulich et al. 2007; Tulich and Mapes 2008; Haertel et al. 2008; Kuang 2008a; Tulich and Kiladis 2012). For example, dynamical fields of 2-day waves produced by a linear model are well reproduced by the first and second baroclinic modes (Fig. 1.11). Shallow circulation due to the second mode could moisten the middle troposphere, which may trigger the subsequent deep convection (Kuang 2008b; Peters and Bretherton 2006; Haertel et al. 2008). Some theoretical studies have suggested that the second mode is a response to the first mode (Frierson 2007; Raymond and Fuchs 2007).

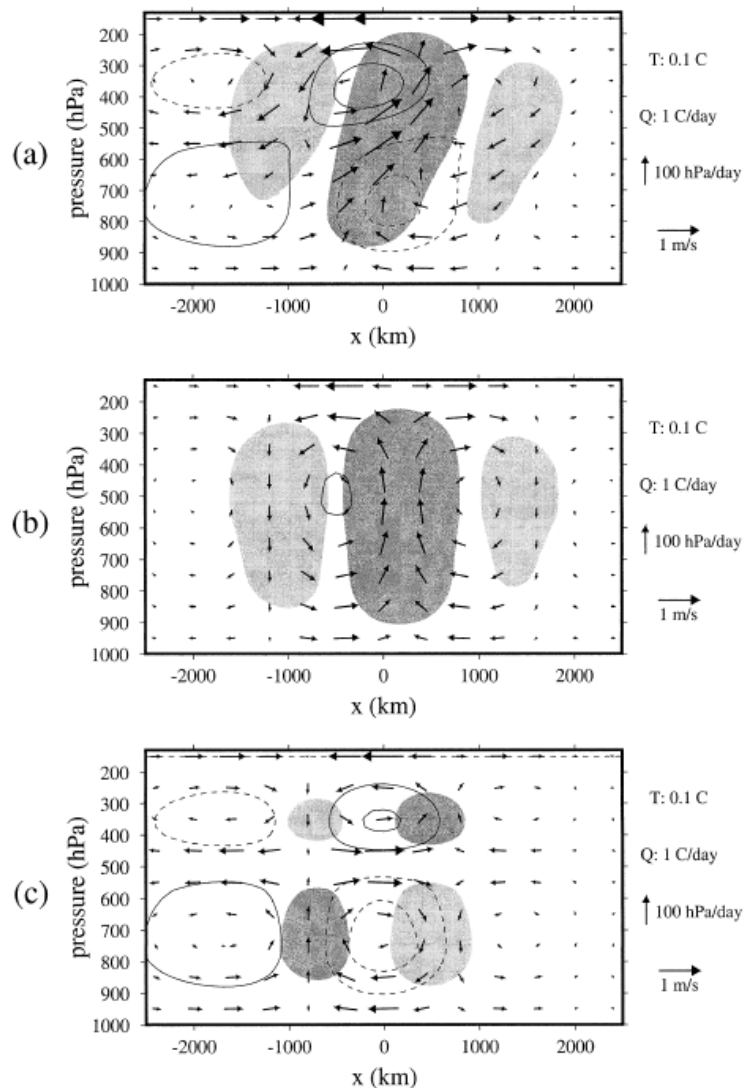


**Fig. 1.11:** A longitude-pressure cross section of 2-day wave produced by a linear model at  $-6$  h for (a) a superposition of the first and second modes, (b) the first mode, and (c) the second mode. Positive (negative) heating rate are shaded by dark (light) color. Positive (negative) temperature perturbation is contoured with solid (dash) lines with interval of  $0.1$  C. Arrow denotes vertical and zonal wind. From Haertel and Kiladis (2004)

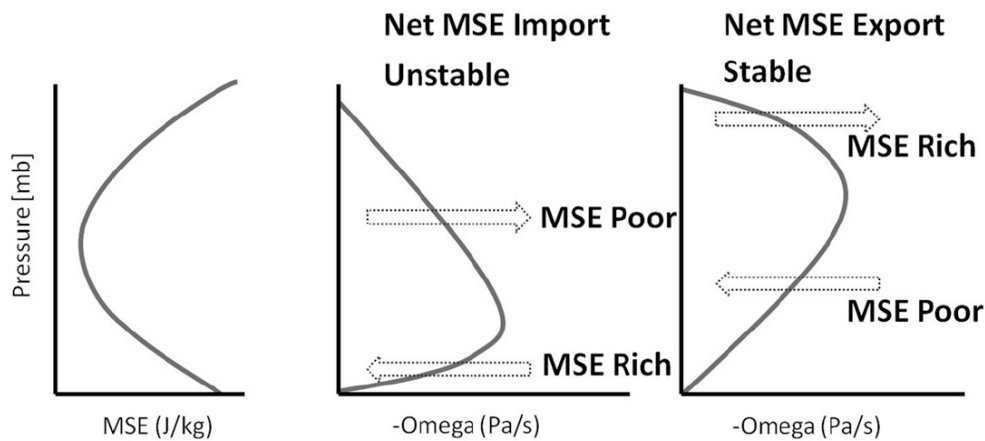


**Fig. 1.12:** A schematic of MSE profile (left) and vertical velocity profiles (middle and right). The leftward (rightward) arrows denote wind divergence (convergence). A bottom-heavy (top-heavy) profile of vertical velocity is connected with net MSE import (export) in the column. From [Inoue and Back \(2015b\)](#)

The moisture stratiform instability mechanism emphasizes an importance of tropospheric moisture in the coupling mechanism, which is consistent with observational facts that tropical deep convection is closely linked to tropospheric moisture ([Sherwood 1999](#); [Bretherton et al. 2004](#); [Peters and Neelin 2006](#); [Holloway and Neelin 2009](#); [Neelin et al. 2009](#); [Masunaga 2012b](#)). It is also known from observational investigations that a moisture increase in the middle troposphere plays a key role in convective development of CCEWs and MJO ([Benedict and Randall 2007](#); [Kiladis et al. 2009](#)). Although the relationship between the moistening in the troposphere and convective amplification is a chicken-and-egg problem, tropospheric moisture is considered to be a key for the coupling mechanism.

In line with the above observational investigations, recent theoretical models of CCEWs and MJO have examined the thermodynamic process by using moist static energy (MSE) nearly conserved in moist adiabatic process ([Neelin and Yu 1994](#); [Sobel et al. 2001](#); [Peters and Bretherton 2006](#); [Fuchs and Raymond 2007](#); [Kuang 2008b](#); [Maloney 2009](#); [Raymond et al. 2009](#); [Maloney et al. 2010](#); [Andersen and Kuang 2012](#); [Kiranmayi and Maloney 2011](#); [Kim et al. 2014](#); [Hannah and Maloney 2014](#); [Benedict et al. 2014](#); [Inoue and Back 2015a](#), and many others). The budget equation of vertical integrated MSE is a useful tool to diagnose the relationship between tropical convection and the large-scale circulation (e.g., [Back and Bretherton 2006](#); [Inoue and Back 2015ab](#)). Figure 1.12 shows that MSE recharge-discharge process changes with the large-scale vertical motion profile during convective life cycle. The recharge (discharge) process due to a bottom-heavy (top-heavy)  $\omega$ -profile is related to the amplification (dissipation) of convection. Assuming temperature anomaly is negligible small in the tropics (e.g., [Sobel et al. 2001](#)), variation of column MSE is nearly identical to that of column moisture. Equatorial disturbances destabilized by the moisture increase in the troposphere, associated with bottom-heavy profile of vertical velocity, are often called a “moisture mode”. A series of recent investigations have discussed the MJO dynamics in terms of the moisture mode ([Neelin and Yu](#)

1994; Raymond et al. 2009; Sobel et al. 2001; Fuchs and Raymond 2007; Kuang 2008b).

### 1.2.3 Mechanism of slowdown of CCEWs

As described in section 1.2.1, CCEWs have shallower equivalent depth (or slower phase speed) than the dry counterpart. Different lines of theory have been proposed to explain the slowdown of phase speed. One of the well-established ideas explains the suppressed phase speed in terms of the reduced static stability (Neelin and Held 1987; Neelin and Yu 1994; Emanuel et al. 1994; Tian and Ramanathan 2003; Sobel and Bretherton 2003; Frierson et al. 2004; Raymond et al. 2009). This approach emphasizes the prominent role of the first baroclinic mode (deep convective mode). Adiabatic cooling due to strong upward motion is partially canceled out by diabatic heating due to the release of latent heat. The cancellation effectively reduces static stability in the atmosphere, leading to a slower phase speed than the dry first mode ( $\sim 50 \text{ m s}^{-1}$ ). The effective static stability is sometimes related to the gross moist stability (GMS), which was originally introduced by Neelin and Held (1987). It has been proposed that the square of the phase speed is proportional to GMS (Neelin and Yu 1994; Emanuel et al. 1994; Tian and Ramanathan 2003; Frierson et al. 2004) or the normalized GMS (NGMS) (Sobel and Bretherton 2003; Raymond et al. 2009). Another school of theory discusses the stratiform instability mechanism (Mapes 2000; Majda and Shefter 2001; Majda et al. 2004; Khouider and Majda 2006a; Kuang 2008b), which focuses on the roles of the second baroclinic mode or the stratiform mode as a key ingredient of instability as mentioned above. The second mode is considered to make CCEWs propagate at a similar phase speed as the dry second mode ( $\sim 25 \text{ m s}^{-1}$ ). It should be noted that the reduced static stability mechanism does not necessarily contradict the stratiform instability: a slowdown of the first mode may be caused by a reduction of static stability, whereas the second mode could concurrently play an independent role. Hence, a comprehensive theoretical framework including these two theories is needed to better understand mechanism of the slowdown of CCEWs.

### 1.2.4 Quasi-2-day wave

A quasi-2-day wave is a synoptic-scale disturbance in the tropical atmosphere, which is accompanied by organized cloud clusters propagating westward with a period of about two days (Takayabu 1994ab; Takayabu et al. 1996; Chen et al. 1996; Chen and Houze 1997; Haertel and Johnson 1998; Haertel and Kiladis 2004; Haertel et al. 2008) (Fig. 1.13). The disturbance is often associated with the active phase of the MJO (Nakazawa 1988; Chen et al. 1996; Clayson et al. 2002) (Fig. 1.14). The 2-day waves have been analyzed using sounding observations in Tropical Ocean and Global Atmosphere Coupled Ocean-Atmosphere Response Experiment (TOGA-COARE) intensive operative period (IOP) during the period from November 1992 to February 1993 (e.g., Takayabu et al. 1996; Haertel and Johnson 1998; Haertel and Kiladis 2004; Haertel et al. 2008). Although the observational area and period is limited, high-resolution COARE soundings have revealed the prominent features of quasi-2-day waves. First, COARE 2-day wave has a propagation speed of about  $10\text{-}30 \text{ m s}^{-1}$  and a zonal wavelength of about 1,000-4,000 km. Second, the dynamical fields represent a vertically tilted top-heavy structure. The tilting structure is common among various CCEWs and MJO (e.g., Kiladis et al.

2009). Third, the temperature anomaly shows a boomerang-like structure. Fourth, the waves have distinct developing stages in their life cycle, which are associated with different cloud types: a shallow convective, deep convective, and stratiform clouds. These stages are common to CCEWs, MJO, and mesoscale convective systems (e.g., Houze 2004; Kikuchi and Takayabu 2004; Mapes et al. 2006).

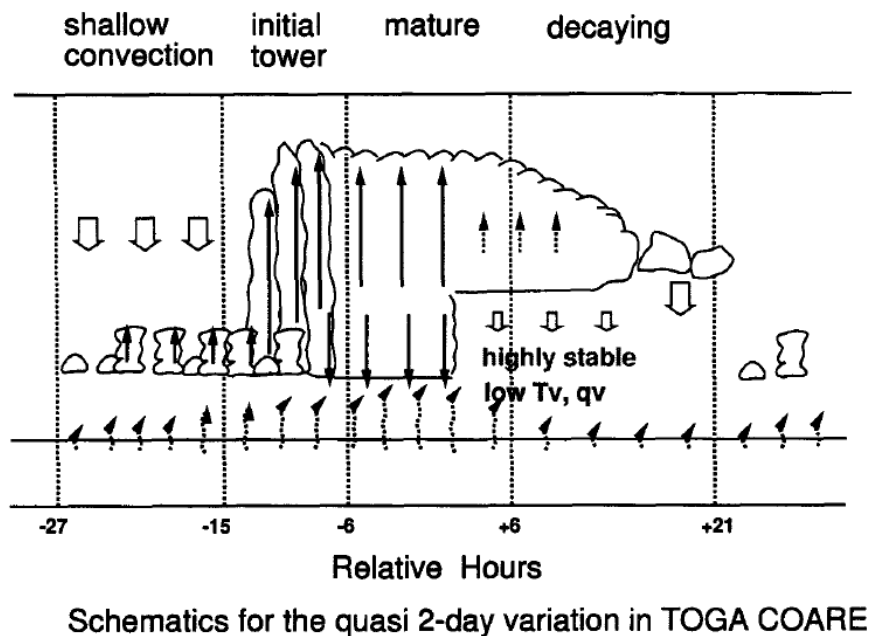


**Fig. 1.13:** A schematic of convective developing stages in quasi-2-day wave. From Takayabu et al. (1996).

It is argued that the dynamics of the 2-day waves are explained by  $n = 1$  convectively coupled westward inertia gravity (WIG) wave (Takayabu 1994b; Takayabu et al. 1996; Haertel and Johnson 1998; Wheeler and Kiladis 1999; Wheeler et al. 2000; Haertel and Kiladis 2004; Haertel et al. 2008; Kiladis et al. 2009; Tulich and Kiladis 2012; Sumi and Masunaga 2016). The dry WIG wave, not coupled with convection, is one of the equatorial waves derived from the shallow water equation linearized in equatorial  $\beta$  plain by Matsuno (1966). The above studies have shown that the horizontal structure of 2-day waves is qualitatively consistent with that of WIG waves. WIG filtering of cloudiness further shows that the WIG wave is most prominently occurred in the Indo-Pacific Ocean region (e.g., Wheeler and Kiladis 1999; Kiladis et al. 2009; Tulich and Kiladis 2012; Sumi and Masunaga 2016), while the WIG filters are designed in slightly different ways. As shown in Fig. 1.7, spectrum signal of the WIG waves peaks along the theoretical dispersion curves with an equivalent depth of about 12-50 m (Takayabu 1994a; Wheeler and Kiladis 1999; Wheeler et al. 2000; Roundy and Frank 2004; Kiladis et al. 2009; Yasunaga and Mapes 2012). This means that convectively coupled WIG wave has

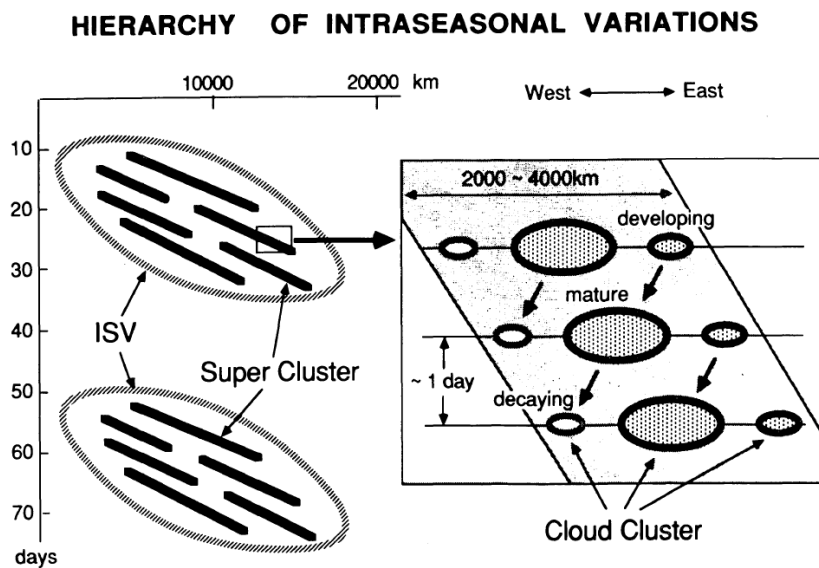


**Fig. 1.14:** Hierarchical structure of intraseasonal variations. From Nakazawa (1988).

a shallower equivalent depth (or slower phase speed) than the dry counterpart.

Despite recent theoretical improvements (see section 1.2.2), the coupling mechanisms of 2-day waves have been less examined, in the light of both the multiple vertical modes and the tropospheric moisture, than that of the other CCEWs and MJO. As a few exceptions (e.g., Haertel and Kiladis 2004; Haertel et al. 2008), the dynamical fields in 2-day waves are analyzed by using the multiple mode model whose basic states are given by COARE soundings. Haertel and Kiladis (2004) showed, for 2-day waves produced by a linear primitive equation model, that their dynamical structures are well reproduced by a superposition of the first and second baroclinic modes. Haertel et al. (2008) also showed that the dynamical fields of COARE 2-day waves are explained by a superposition of the first three baroclinic modes and that shallow updraft due to the higher modes contributes to an increase of tropospheric moisture preceding deep convection. These results are roughly consistent with stratiform instability mechanism (e.g., Mapes 2000) or moisture stratiform instability mechanism (e.g., Kuang 2008b). The relationship between tropospheric moisture and strong convection in COARE 2-day waves is further examined by using budget equation of column MSE, suggesting that MSE variability is mainly regulated by a large-scale vertical motion of the waves (Inoue and Back 2015a). This is nearly consistent with MSE recharge-discharge process predicted by multi-mode model (e.g., Peters and Bretherton 2006). Cross spectral analysis showed a significant coherence between precipitation and mid-tropospheric divergence in WIG waves, suggesting an importance of the second mode to the wave dynamics (Yasunaga and Mapes 2012; Yasunaga and Mapes 2014). It is also showed that precipitation is significantly (less) correlated with moisture in the lower (middle) troposphere, implying that stratiform instability mechanism would be more adequately than moisture stratiform instability in WIG waves.

Although the above studies confirmed multi-modes structure in 2-day wave dynamics, more observational investigations are still required to reveal the coupling mechanism. This study examine the coupling mechanism of 2-day waves in terms of tropospheric

moisture and vertical modes. In chapter 3, the relationship between tropospheric moisture and a large-scale dynamics of 2-day waves is analyzed by using budget equation of column MSE. In chapter 4, the dynamical structure and propagation dynamics are analyzed by using vertical mode decomposition technique.

## 1.3 Theoretical background: equatorial waves

In this section, the dispersion relationships and horizontal structure of dry equatorial waves are summarized following shallow water theory in Matsuno (1966). In section 1.3.1, governing equations are briefly summarized. In sections 1.3.2 and 1.3.3, dispersion relationships and horizontal structure of the waves are derived from eigen-value equation by analogy with Schroedinger equation for a simple harmonic oscillator.

### 1.3.1 Model and basic equations

We consider shallow water system with the depth of the undisturbed layer of homogeneous incompressible fluid in Fig. 1.15. Here  $h$  is the small deviation of the elevation of the top surface, and  $H$  is the mean value of the top surface. In the tropical atmosphere, shallow water approximation is good for representing the wave motion with synoptic-scale zonal wave length ( $L_x \ll H$ ).

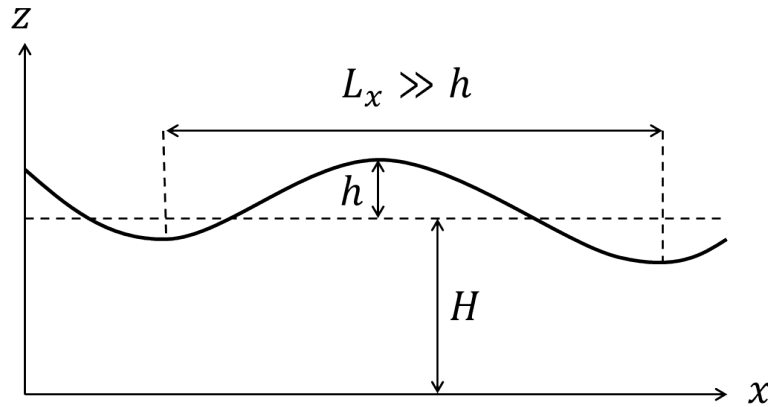


**Fig. 1.15:** Schematic picture of shallow water system.  $H$  is a mean value of the elevation of the top surface,  $h$  is the small deviation of the mean, and  $L_x$  is the zonal wave length.

The equations of motion and the mass conservation in the shallow water system are written as follows (see section 6.1 for more detail):

$$\begin{aligned}
 \frac{\partial u}{\partial t} - fv + g\frac{\partial h}{\partial x} &= 0 \\
 \frac{\partial v}{\partial t} + fu + g\frac{\partial h}{\partial y} &= 0 \\
 \frac{\partial h}{\partial t} + H\left(\frac{\partial u}{\partial x} + \frac{\partial v}{\partial y}\right) &= 0
 \end{aligned} \tag{1.1}$$

where  $f$  is Coriolis parameter and  $g$  is the acceleration of gravity. Here, we assume that Coriolis parameter  $f$  is linearly proportional to the latitude ( $\beta$ -plane approximation):

$$f = \beta y \quad (1.2)$$

where  $\beta$  is Rossby parameter and assumed to be constant. We rewrite Eqs. (1.1) by using the geopotential height  $\phi = gz$ .

$$\begin{aligned} \frac{\partial u}{\partial t} - \beta y v + \frac{\partial \phi}{\partial x} &= 0 \\ \frac{\partial v}{\partial t} + \beta y u + \frac{\partial \phi}{\partial y} &= 0 \\ \frac{\partial \phi}{\partial t} + c^2 \left( \frac{\partial u}{\partial x} + \frac{\partial v}{\partial y} \right) &= 0 \end{aligned} \quad (1.3)$$

where  $c = \sqrt{gH}$  is the velocity of pure gravity waves. By taking the units of time and length as follows

$$\begin{aligned} [T] &= (1/c\beta)^{1/2} \\ [L] &= (c/\beta)^{1/2} \end{aligned} \quad (1.4)$$

Eqs. (1.1) are transformed into non-dimensional form;

$$\begin{aligned} \frac{\partial u}{\partial t} - y v + \frac{\partial \phi}{\partial x} &= 0 \\ \frac{\partial v}{\partial t} + y u + \frac{\partial \phi}{\partial y} &= 0 \\ \frac{\partial \phi}{\partial t} + \frac{\partial u}{\partial x} + \frac{\partial v}{\partial y} &= 0 \end{aligned} \quad (1.5)$$

### 1.3.2 Dispersion relations of equatorial waves

Assume that all solutions in Eqs. (1.5) have the factor  $e^{i(\omega t + kx)}$ ,

$$\begin{pmatrix} u(x, y, t) \\ v(x, y, t) \\ \phi(x, y, t) \end{pmatrix} = \begin{pmatrix} \hat{u}(y) \\ \hat{v}(y) \\ \hat{\phi}(y) \end{pmatrix} e^{i(\omega t + kx)} \quad (1.6)$$

where  $\omega$  is frequency and  $k$  is zonal wave number. Substituting Eqs. (1.6) into (1.5) yields

$$\begin{aligned} i\omega u - y v + ik\phi &= 0 \\ i\omega v + y u + \frac{d\phi}{dy} &= 0 \\ i\omega\phi + ik u + \frac{dv}{dy} &= 0 \end{aligned} \quad (1.7)$$

Here  $y$ -dependent valuables  $\hat{u}, \hat{v}$ , and  $\hat{\phi}$  are replaced by  $u, v$ , and  $\phi$ , respectively for simplicity. Eliminating  $u$  and  $\phi$ , we finally obtain the equation to  $v$  as follows;

$$\left( \frac{d^2}{dy^2} - y^2 \right) v = \left( \omega^2 - k^2 + \frac{k}{\omega} \right) v \quad (1.8)$$

Since the wave is trapped near the equator ( $y \sim 0$ ), the boundary condition is

$$v \rightarrow 0; \quad \text{when } y \rightarrow \pm\infty \quad (1.9)$$

Eq. (1.8) with boundary condition Eq. (1.9) poses an eigen-value problem, which is just the same as Schroedinger equation for a simple harmonic oscillator. The boundary condition (1.9) is satisfied only when the constant  $(\omega^2 - k^2 + k/\omega)$  is equal to an odd integer:

$$\omega^2 - k^2 + \frac{k}{\omega} = 2n + 1 \quad (n = 0, 1, 2, \dots) \quad (1.10)$$

The solution of Eq. (1.8) is expressed as;

$$v(y) = Ae^{-\frac{1}{2}y^2} H_n(y) \quad (1.11)$$

where  $A$  is standard orthogonal coefficient and  $H_n(y)$  is the Hermite polynomial of the  $n$ -th order.

Now, the dispersion relations of equatorial waves are derived. Since Eq. (1.10) is a cubic equation to  $\omega$ , we have three roots when  $n$  and  $k$  are specified. We consider three cases ( $n \geq 1$ ,  $n = 0$ , and  $n = -1$ ) as shown below.

**(i)  $n \geq 1$**

Eq. (1.10) is rewritten as;

$$\frac{\omega^2}{k^2} + \frac{1}{k\omega} = \frac{k^2 + 2n + 1}{k^2} \quad (1.12)$$

The approximate values of three roots of  $\omega$  for very large  $k$ , are given as;

$$\begin{aligned} \omega_{1,2} &\sim \pm\sqrt{k^2 + 2n + 1} \quad (\text{for } \omega \gg k) \\ \omega_3 &\sim \frac{k}{k^2 + 2n + 1} \quad (\text{for } \omega \ll k) \end{aligned} \quad (1.13)$$

$\omega_{1,2}$  are identified as the frequency of inertia-gravity wave, and  $\omega_3$  is that of Rossby wave. Their phase speeds are expressed as;

$$\begin{aligned} c_{1,2} &\sim \pm c_g \sqrt{1 + \frac{1}{k^2} \frac{\beta}{c_g} (2n + 1)} \\ c_3 &\sim \frac{\beta}{k^2 + \frac{\beta}{c_g} (2n + 1)} \end{aligned} \quad (1.14)$$

where  $c_g$  is the velocity of pure gravity wave.

**(ii)  $n = 0$**

Putting  $n = 0$  in Eq. (1.10) gives

$$(\omega - k)(\omega^2 + k\omega - 1) = 0 \quad (1.15)$$

Three roots of Eq. (1.15) is

$$\omega = \begin{cases} -\frac{k}{2} - \sqrt{1 + \left(\frac{k}{2}\right)^2} < 0 \\ -\frac{k}{2} + \sqrt{1 + \left(\frac{k}{2}\right)^2} > 0 \\ k > 0 \end{cases} \quad (1.16)$$

Notice that Rossby wave has lower frequency than inertia gravity (IG) wave. Comparing  $\omega = k$  and  $\omega = -k/2 + \sqrt{1 + (k/2)^2}$  yields

$$\begin{aligned} k \text{ (Rossby)} &< -\frac{k}{2} + \sqrt{1 + \left(\frac{k}{2}\right)^2} \text{ (IG)} \quad (k \leq 1/\sqrt{2}) \\ k \text{ (IG)} &> -\frac{k}{2} + \sqrt{1 + \left(\frac{k}{2}\right)^2} \text{ (Rossby)} \quad (k \geq 1/\sqrt{2}) \end{aligned} \quad (1.17)$$

Then  $\omega$  is classified as follows;

$$\begin{aligned} \omega_1 &= -\frac{k}{2} - \sqrt{1 + \left(\frac{k}{2}\right)^2} \\ \omega_2 &= \begin{cases} -\frac{k}{2} + \sqrt{1 + \left(\frac{k}{2}\right)^2} & (\text{for } k \leq 1/\sqrt{2}) \\ k & (\text{for } k \geq 1/\sqrt{2}) \end{cases} \\ \omega_3 &= \begin{cases} k & (\text{for } k \leq 1/\sqrt{2}) \\ -\frac{k}{2} + \sqrt{1 + \left(\frac{k}{2}\right)^2} & (\text{for } k \geq 1/\sqrt{2}) \end{cases} \end{aligned} \quad (1.18)$$

where  $\omega_1$  is identified as the frequency of eastward IG wave,  $\omega_2$  is that of westward IG wave, and  $\omega_3$  is that of Rossby wave. Here we should notice that  $\omega = k$  should be rejected, because  $u$  and  $\phi$  are infinitely diverges (see Eqs. (1.23)). Therefore,  $\omega$  is reclassified as follows;

$$\begin{aligned} \omega_1 &= -\frac{k}{2} - \sqrt{1 + \left(\frac{k}{2}\right)^2} \text{ (Eastward IG)} \\ \omega_2 &= \begin{cases} -\frac{k}{2} + \sqrt{1 + \left(\frac{k}{2}\right)^2} & (\text{for } k \leq 1/\sqrt{2}) \text{ (Westward IG)} \\ -\frac{k}{2} + \sqrt{1 + \left(\frac{k}{2}\right)^2} & (\text{for } k \geq 1/\sqrt{2}) \text{ (Rossby)} \end{cases} \end{aligned} \quad (1.19)$$

where  $\omega_1$  is the frequency of eastward IG wave and  $\omega_2$  is that of mixed Rossby-gravity wave.

### (iii) $n = -1$

We consider solution which is not included in Eq. (1.10). Notice that Eq. (1.10) was obtained by reducing the original simultaneous Eq. (1.5) to the equation for  $v$  only. There can exist a solution which has no meridional velocity. Putting  $v = 0$  in Eq. (1.5) yields

$$\begin{aligned} i\omega u + ik\phi &= 0 \\ yu + \frac{d\phi}{dy} &= 0 \\ i\omega\phi + iku &= 0 \end{aligned} \quad (1.20)$$

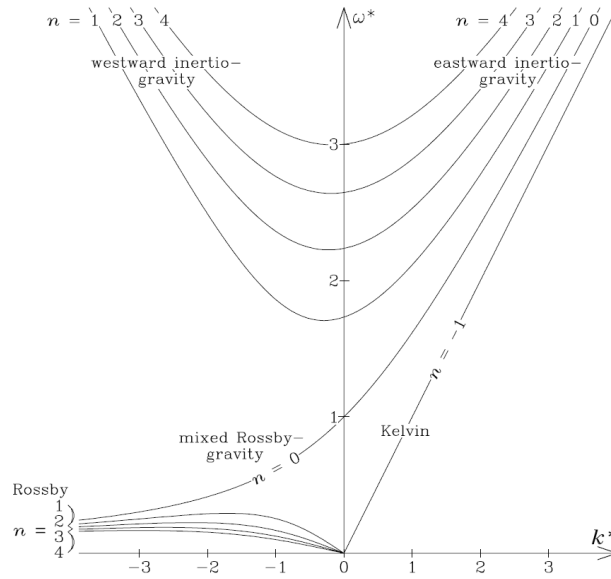


**Fig. 1.16:** Dispersion curves for equatorial waves derived in Matsuno (1966). From Kiladis et al. (2009).

By using the first and the third equations in Eqs. (1.20), the solutions only exist when

$$(\omega - k)(\omega + k) = 0 \quad (1.21)$$

Then the solutions are obtains are as follows;

$$\begin{aligned} \phi = u = Ce^{-y^2/2} \quad \text{for } \omega = -k \\ \phi = -u = Ce^{y^2/2} \quad \text{for } \omega = k \end{aligned} \quad (1.22)$$

Since the lower one dose not satisfy the boundary condition Eq. (1.9), it is rejected. The upper solution  $\omega = -k$  is obtained if we put  $n = -1$  in Eq. (1.10), which is identified as the frequency of Kelvin wave.

The dispersion curves for equatorial waves are shown in Fig. 1.16. The wave number ( $k^* = k(\sqrt{(gH)/\beta})^{1/2}$ ) and frequency ( $\omega^* = \omega/(\beta\sqrt{(gH)})^{1/2}$ ) are non-dimensional values (see Eq. (1.4)). Westward (eastward) propagating waves are in the region of negative (positive) wave number. The Kelvin wave is labeled as  $n = -1$  as described above.

### 1.3.3 Horizontal structure of equatorial waves

In section 1.3.2, eigenvalue ( $\omega_{nl}$ ) of Eq. (1.8) is obtained. In this section, the eigenfunctions are derived as shown below. From Eq. (1.7),  $u$  and  $\phi$  are expressed as follows:

$$\begin{aligned} u &= \frac{1}{i(\omega^2 - k^2)} \left( \omega y v + k \frac{dv}{dy} \right) \\ \phi &= \frac{1}{-i(\omega^2 - k^2)} \left( k y v + \omega \frac{dv}{dy} \right) \end{aligned} \quad (1.23)$$

Using Eq. (1.11) and the recurrence formulas for Hermite's polynomials

$$\begin{aligned}\frac{dH_n(\xi)}{d\xi} &= 2nH_{n-1}(\xi) \\ H_{n+1}(\xi) &= 2\xi H_n(\xi) - 2nH_{n-1}(\xi)\end{aligned}\quad (1.24)$$

eigenfunctions of  $u$  and  $\phi$  are written as follows:

$$\begin{aligned}u &= A \frac{e^{-y^2/2}}{i(\omega^2 - k^2)} \left( \frac{1}{2}(\omega - k)H_{n+1} + n(\omega + k)H_{n-1} \right) \\ v &= A \frac{e^{-y^2/2}}{i(\omega^2 - k^2)} \left( \frac{1}{2}(\omega - k)H_{n+1} - n(\omega + k)H_{n-1} \right)\end{aligned}\quad (1.25)$$

Hence eigenfunctions for eigenvalue  $\omega_{nl}$  are written as:

$$\begin{pmatrix} u \\ v \\ \phi \end{pmatrix}_{nl} = \begin{pmatrix} i(\omega_{nl}^2 - k^2)\psi_n \\ n(\omega_{nl} - k)\psi_{n-1} + \frac{1}{2}(\omega_{nl} - k)\psi_{n+1} \\ -n(\omega_{nl} - k)\psi_{n-1} + \frac{1}{2}(\omega_{nl} - k)\psi_{n+1} \end{pmatrix}\quad (1.26)$$

where

$$\psi_n = e^{-\frac{1}{2}y^2} H_n(y)\quad (1.27)$$

and subscripts  $n$  and  $l$  denote meridional mode number and the three roots of Eq. (1.15), respectively. If  $n$  is an odd (even) number,  $v$  is an odd (even) function and  $u$  and  $\phi$  are even (odd) functions with respect to  $y$ . The eigenfunctions of equatorial waves are summarized as follows:

(i)  $n \geq 1$

$$\begin{pmatrix} u \\ v \\ \phi \end{pmatrix}_{nl} = \begin{pmatrix} i(\omega_{nl}^2 - k^2)\psi_n \\ n(\omega_{nl} - k)\psi_{n-1} + \frac{1}{2}(\omega_{nl} - k)\psi_{n+1} \\ -n(\omega_{nl} - k)\psi_{n-1} + \frac{1}{2}(\omega_{nl} - k)\psi_{n+1} \end{pmatrix}\quad (1.28)$$

(ii)  $n = 0$

$$\begin{pmatrix} u \\ v \\ \phi \end{pmatrix}_{0l} = \begin{pmatrix} 2i(\omega_{0l} + k)\psi_0 \\ \psi_1 \\ \psi_1 \end{pmatrix}\quad (1.29)$$

(iii)  $n = -1$

$$\begin{pmatrix} u \\ v \\ \phi \end{pmatrix}_{-1} = \begin{pmatrix} 0 \\ \psi_0 \\ \psi_0 \end{pmatrix}\quad (1.30)$$

Figure 1.17 shows horizontal structure of  $n = 1$  WIG wave. Since  $n$  is an odd number,  $v$  is an odd function and  $u$  and  $\phi$  are even functions with respect to  $y$ , that is, the dynamical field is symmetric to the equator.

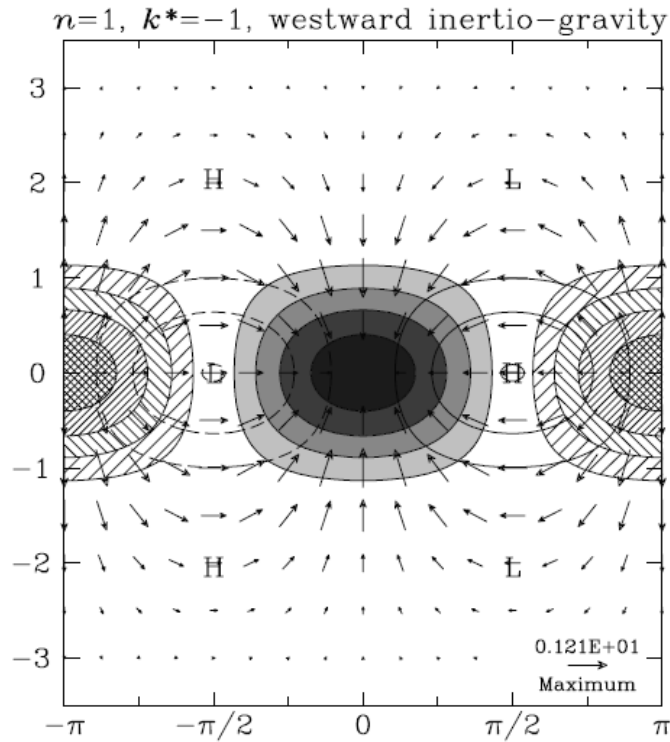


**Fig. 1.17:** Horizontal structure of  $n = 1$  WIG wave derived in Matsuno (1966). Vector represents horizontal wind  $(u, v)$ . Shading (hatching) represents convergence (divergence). Contours are geopotential  $\phi$ . From Kiladis et al. (2009).

## 1.4 Theoretical background: vertical mode transform

SW theory (see section 1.3) describes the zonal propagation of equatorial waves, where the depth of the stable layer of fluid ( $H$ ) determines the phase speed and the spatial scale of equatorial waves. Here, primitive equations linearized about a basic state of rest are considered to describe the motion of the three dimensional atmosphere (Fulton and Schubert 1985). By separating the variables, the primitive equations are divided into the equations of horizontal structure and the equation of vertical structure (eigenvalue equation). Since the horizontal structure equations are identical to the SW equations, the mean depth of the former is called equivalent depth. The vertical structure functions (vertical modes) and the equivalent depth of the waves are calculated by solving the eigenvalue equation (section 1.4.1-1.4.3). The differential method solving the eigenvalue equation is also summarized in sections 2.2.6, 6.3, and 6.5.

### 1.4.1 Governing equations

The primitive equations are used to describe the motion of atmospheric disturbance. First, the primitive equations on a  $\beta$ -plane are linearized about a basic state of rest. Second, the boundary conditions are determined to solve the equations.

### Linearization of the primitive equations

Consider the motions of a compressible atmosphere in hydrostatic balance (primitive equations system). The primitive equations on a  $\beta$ -plane are written as;

$$\frac{\partial u}{\partial t} - \beta y v + \frac{\partial \phi}{\partial x} = 0 \quad (1.31)$$

$$\frac{\partial v}{\partial t} - \beta y u + \frac{\partial \phi}{\partial y} = 0 \quad (1.32)$$

$$\frac{\partial \phi}{\partial p} + \frac{RT}{p} = 0 \quad (1.33)$$

$$c_p \frac{\partial T}{\partial t} - c_p S \omega = Q \quad (1.34)$$

$$\frac{\partial u}{\partial x} + \frac{\partial v}{\partial y} + \frac{\partial \omega}{\partial p} = 0 \quad (1.35)$$

where  $T$  is temperature,  $R$  is gas constant of dry air,  $c_p$  is specific heat at constant pressure, and  $Q$  is heating roughly equal to the apparent heat source in Yanai et al. (1973).  $S$  is the static stability parameter for the isobaric system

$$S = \frac{RT}{c_p P} - \frac{\partial T}{\partial p} = -\frac{T}{\theta} \frac{\partial \theta}{\partial p} \quad (1.36)$$

where  $\theta$  is potential temperature  $\theta = T(p_0/p)^{R/c_p}$ . Eqs. (1.31) and (1.32) are the momentum equations, Eq. (1.33) is hydrostatic equation, Eq. (1.34) is thermodynamic equation, and Eq. (1.35) is continuity equation.

The primitive equations are linearized about the motionless hydrostatic basic state ( $\bar{T}$  and  $\bar{\phi}$ ). The variables are separated into a basic state of rest ( $\bar{\cdot}$ ), where  $\bar{u} = \bar{v} = \bar{\omega} = 0$ , and perturbation from the basic state ( $\prime$ ).

$$\begin{aligned} u &= u' \\ v &= v' \\ \omega &= \omega' \\ \phi &= \bar{\phi} + \phi' \\ T &= \bar{T} + T' \\ Q &= Q' \end{aligned} \quad (1.37)$$

Substituting Eqs. (1.37) into (1.31)-(1.35) yields the primitive equations on a  $\beta$ -plane linearized about a basic state of rest:

$$\frac{\partial u'}{\partial t} - \beta y v' + \frac{\partial \phi'}{\partial x} = 0 \quad (1.38)$$

$$\frac{\partial v'}{\partial t} - \beta y u' + \frac{\partial \phi'}{\partial y} = 0 \quad (1.39)$$

$$\frac{\partial \phi'}{\partial p} + \frac{RT'}{p} = 0 \quad (1.40)$$

$$c_p \frac{\partial T'}{\partial t} - c_p \bar{S} \omega' = Q' \quad (1.41)$$

$$\frac{\partial u'}{\partial x} + \frac{\partial v'}{\partial y} + \frac{\partial \omega'}{\partial p} = 0 \quad (1.42)$$

where  $\bar{S} = R\bar{T}/c_p P - \partial\bar{T}/\partial p$  is static stability of a basic state.

### Boundary conditions

To obtain discrete modes, the atmosphere is taken to be vertically bounded at the top boundary ( $p_t$ ) and the bottom boundary ( $p_b$ ). We use the upper rigid-lid boundary condition, where the vertical p-velocity  $\omega$  is required to vanish at the top boundary and the actual vertical velocity  $w$  is required to vanish at the bottom boundary.

$$\omega = 0 \quad \text{at } p = p_t \quad (1.43)$$

$$w = 0 \quad \text{at } p = p_b \quad (1.44)$$

Using the hydrostatic equation  $\partial z/\partial p = -1/(\rho g)$ , where  $\rho$  is the density of the gas, Eq. (1.44) is rewritten as

$$w = \frac{\partial z}{\partial t} + \mathbf{V} \cdot \nabla z - \omega \frac{1}{\rho g} = 0 \quad (1.45)$$

Multiplying the both side of Eq. (1.45) by  $g$  and replacing  $gz$  for  $\phi$  yield

$$\frac{\partial \phi}{\partial t} + \mathbf{V} \cdot \nabla \phi - \omega \frac{RT}{p} = 0 \quad (1.46)$$

Substituting Eqs. (1.37) into (1.43) and (1.46), we obtain the boundary conditions linearized about the basic state of rest:

$$\omega' = 0 \quad \text{at } p = p_t \quad (1.47)$$

$$\frac{\partial \phi'}{\partial t} - \omega' \frac{R\bar{T}}{p} = 0 \quad \text{at } p = p_b \quad (1.48)$$

### 1.4.2 Simplified governing equations and the vertical differential operator

In this section, the vertical differential operator is introduced to simplify the governing equations. Now, we rewrite  $u' \rightarrow u, v' \rightarrow v, \omega' \rightarrow \omega, \phi' \rightarrow \phi, T' \rightarrow T, Q' \rightarrow Q$ , and  $\bar{S} \rightarrow S$  in Eqs. (1.38)-(1.42) and (1.47)-(1.48). Eliminating  $T$  and  $\omega$  between (1.40)-(1.42) yields

$$\hat{L} \left\{ \frac{\partial \phi}{\partial t} \right\} + \frac{\partial u}{\partial x} + \frac{\partial v}{\partial y} = \frac{\partial}{\partial p} \left( \frac{Q}{S c_p} \right) \quad (1.49)$$

where  $\hat{L}$  is the vertical differential operator and operates to the function  $f(p)$  as follows:

$$\hat{L} \{ f(p) \} = - \frac{\partial}{\partial p} \frac{p}{SR} \frac{\partial}{\partial p} f(p) \quad (1.50)$$

Let us denote the rhs of Eq. (1.49) as ‘‘forced divergence’’  $D$ .

$$\begin{aligned} D &= \frac{\partial}{\partial p} \frac{1}{SR} \frac{R}{c_p} Q \\ &= - \frac{\partial}{\partial p} \frac{p}{SR} \frac{\partial}{\partial p} \left( \frac{\partial \Phi}{\partial t} \right) \\ &= \hat{L} \left\{ \frac{\partial \Phi}{\partial t} \right\} \end{aligned} \quad (1.51)$$

where we define the “forced geopotential”  $\Phi$  as

$$\frac{R}{c_p}Q = -p \frac{\partial}{\partial p} \left( \frac{\partial \Phi}{\partial t} \right) \quad (1.52)$$

Eq. (1.49) is rewritten by using Eq. (1.51) as

$$\hat{L} \left\{ \frac{\partial \phi}{\partial t} - \frac{\partial \Phi}{\partial t} \right\} = - \left( \frac{\partial u}{\partial x} + \frac{\partial v}{\partial y} \right) \quad (1.53)$$

The only vertical derivatives in the governing equations, Eqs. (1.38), (1.39), and (1.53), appear in the term  $\hat{L} \{ \partial \phi / \partial t - \partial \Phi / \partial t \}$ .

Eliminating  $T$  between Eqs. (1.40) and (1.41) yields

$$\omega = \frac{1}{RS} p \frac{\partial}{\partial p} \left( \frac{\partial \Phi}{\partial t} - \frac{\partial \phi}{\partial t} \right) \quad (1.54)$$

Substituting Eqs. (1.54) into (1.47) and (1.48), we obtain the boundary conditions:

$$p \frac{\partial}{\partial p} \left( \frac{\partial \Phi}{\partial t} - \frac{\partial \phi}{\partial t} \right) = 0 \quad \text{at } p = p_t \quad (1.55)$$

$$p \frac{\partial}{\partial p} \left( \frac{\partial \Phi}{\partial t} - \frac{\partial \phi}{\partial t} \right) + \frac{p^2 \sigma}{RT} \left( \frac{\partial \Phi}{\partial t} - \frac{\partial \phi}{\partial t} \right) = 0 \quad \text{at } p = p_b \quad (1.56)$$

where  $\sigma = SR/p$ . Assuming  $\partial \Phi / \partial t = 0$  at  $p = p_b$ , we obtain Eq. (1.56).

### 1.4.3 The vertical mode transform

First, we define vertical inner product and vertical mode transform. Second, we derive the vertical mode in the governing equations, which is the eigenfunction of the vertical differential operator  $\hat{L}$ .

#### Vertical inner product

We define the vertical inner product  $\langle A|B \rangle$  for any functions  $A$  and  $B$  of pressure  $p$ :

$$\langle A|B \rangle = \frac{1}{p_b - p_t} \int_{p_t}^{p_b} AB dp \quad (1.57)$$

Consider an integral transform of the form

$$\hat{A}_n = \langle A|h_n \rangle = \frac{1}{p_b - p_t} \int_{p_t}^{p_b} A h_n dp \quad (1.58)$$

where the kernel  $h_n(p)$  of the transform is the vertical structure function of a vertical mode and  $\hat{A}_n$  is the mode transform coefficient. Here,  $h_n(p)$  consists of a normalized orthogonal system:

$$\langle h_m|h_n \rangle = \frac{1}{p_B - p_T} \int_{p_T}^{p_B} h_m h_n dp = \delta_{mn} \quad (1.59)$$

where  $\delta_{mn}$  is Kronecher delta.

Variable  $A$  is expressed as a superposition of the vertical modes.

$$A = \sum_{n=0}^{\infty} A_n = \sum_{n=0}^{\infty} \hat{A}_n h_n \quad (1.60)$$

where  $A_n = \hat{A}_n h_n$  is the mode transform component and  $\hat{A}_n$  is the mode transform coefficient. A contribution ratio of the n-th mode ( $P_n$ ) is defined as

$$P_n = \frac{\langle A_n^2 \rangle}{\langle A^2 \rangle} = \frac{\hat{A}_n^2}{\sum_{n=0}^{\infty} \hat{A}_n^2}. \quad (1.61)$$

### Eigenvalue equation

Derive the vertical modes  $h_n$  in the governing equations. By using  $h_n$ , the mode transform components of  $u$ ,  $v$ ,  $\phi$ , and  $D$  are expressed as follows;

$$\begin{pmatrix} u_n(x, y, p, t) \\ v_n(x, y, p, t) \\ \phi_n(x, y, p, t) \\ D_n(x, y, p, t) \end{pmatrix} = \begin{pmatrix} \hat{u}_n(x, y, t) \\ \hat{v}_n(x, y, t) \\ \hat{\phi}_n(x, y, t) \\ \hat{D}_n(x, y, t) \end{pmatrix} h_n(p) \quad (1.62)$$

The vertical mode is derived from Eq. (1.53) since the vertical derivatives in the governing equations only appear in the lhs of Eq. (1.53). Letting  $F = (\partial\phi/\partial t - \partial\Phi/\partial t)$ , we rewrite Eq. (1.53) as

$$\hat{L}F = -\left(\frac{\partial u}{\partial x} + \frac{\partial v}{\partial y}\right) \quad (1.63)$$

Multiplying both side of Eq. (1.63) by  $h_n$  from the right and calculating the vertical inner product becomes

$$\langle \hat{L}F | h_n \rangle = -\left(\frac{\partial \hat{u}_n}{\partial x} + \frac{\partial \hat{v}_n}{\partial y}\right) \quad (1.64)$$

The kernel  $h_n$  of the transform is to be chosen so that

$$\langle \hat{L}F | h_n \rangle = \lambda_n \langle F | h_n \rangle \quad (1.65)$$

with  $\lambda_n$  a constant. The lhs of Eq. (1.65) is calculated as

$$\begin{aligned} \langle \hat{L}F | h_n \rangle &= \frac{1}{p_b - p_t} \int_{p_t}^{p_b} (\hat{L}F) h_n dp \\ &= \frac{1}{p_b - p_t} \int_{p_t}^{p_b} \left( -\frac{\partial}{\partial p} \frac{1}{\sigma} \frac{\partial F}{\partial p} \right) h_n dp \\ &= \frac{-1}{p_b - p_t} \left[ \frac{1}{\sigma} \frac{\partial F}{\partial p} h_n \right]_{p_t}^{p_b} + \frac{1}{p_b - p_t} \int_{p_t}^{p_b} \frac{1}{\sigma} \frac{\partial F}{\partial p} \frac{\partial h_n}{\partial p} dp \\ &= \frac{-1}{p_b - p_t} \left[ \frac{1}{\sigma} \frac{\partial F}{\partial p} h_n \right]_{p_t}^{p_b} + \frac{1}{p_b - p_t} \left[ \frac{1}{\sigma} F \frac{\partial h_n}{\partial p} \right]_{p_t}^{p_b} - \frac{1}{p_b - p_t} \int_{p_t}^{p_b} F \frac{\partial}{\partial p} \frac{1}{\sigma} \frac{\partial h_n}{\partial p} dp \\ &= \frac{1}{p_b - p_t} \left[ \frac{1}{\sigma} F \frac{\partial h_n}{\partial p} - \frac{1}{\sigma} \frac{\partial F}{\partial p} h_n \right]_{p_t}^{p_b} + \langle F | \hat{L}h_n \rangle \end{aligned} \quad (1.66)$$

Eq. (1.66) is equal to the rhs of Eq. (1.65), if we suppose the followings;

$$\hat{L}h_n = \lambda_n h_n \quad (1.67)$$

$$\left[ \frac{1}{\sigma} F \frac{\partial h_n}{\partial p} - \frac{1}{\sigma} \frac{\partial F}{\partial p} h_n \right]_{p_t}^{p_b} = 0 \quad (1.68)$$

Eq. (1.67) is the eigenvalue equation and  $h_n$  and  $\lambda_n$  denotes the eigenfunction and eigenvalue, respectively. Notice that  $\lambda_n = 1/c_n^2$  ( $c_n$  : phase speed). Substituting Eqs. (1.67) into (1.66), we obtain  $\langle \hat{L}F|h_n \rangle = \langle F|\hat{L}^\dagger h_n \rangle = \langle F|\hat{L}h_n \rangle$ , which indicates that  $\hat{L}$  is a Hermitian operator ( $\hat{L}^\dagger = \hat{L}$ ).

Substituting Eqs. (1.55)-(1.56) into (1.68), we obtain the boundary conditions for  $h_n$ :

$$\left( P \frac{\partial h_n}{\partial p} \right)_{p_b} + \left( \frac{p^2 \sigma}{RT} h_n \right)_{p_b} = 0 \quad \text{at } p = p_b \quad (1.69)$$

$$\left( P \frac{\partial h_n}{\partial p} \right)_{p_t} = 0 \quad \text{at } p = p_t \quad (1.70)$$

Applying the vertical transform to the governing equations Eqs. (1.38)-(1.39) and (1.53) results in

$$\frac{\partial \hat{u}_n}{\partial t} - \beta y \hat{v}_n + \frac{\partial \hat{\phi}_n}{\partial x} = 0 \quad (1.71)$$

$$\frac{\partial \hat{v}_n}{\partial t} - \beta y \hat{u}_n + \frac{\partial \hat{\phi}_n}{\partial y} = 0 \quad (1.72)$$

$$\left( \frac{\partial \hat{\phi}_n}{\partial t} - \hat{D}_n \right) = -\frac{1}{\lambda_n} \left( \frac{\partial \hat{u}_n}{\partial x} + \frac{\partial \hat{v}_n}{\partial y} \right) \quad (1.73)$$

where  $\hat{D}_n = \partial \hat{\Phi}_n / \partial t$ .

### Vertical mode transform components of the other variables

The mode transform components of  $u$ ,  $v$ ,  $\phi$ , and  $D$  are expressed as in Eq. (1.62). That of  $T$ ,  $\omega$ , and  $Q$  are also written by using the vertical mode  $h_n$  (see section 6.2 for more detail).

$$T_n = -\frac{1}{R} \hat{\phi}_n \frac{\partial h_n}{\partial \ln p} \quad (1.74)$$

$$\omega_n = -\left( \frac{\partial \hat{u}_n}{\partial x} + \frac{\partial \hat{v}_n}{\partial y} \right) \int_{p_t}^p h_n dp \quad (1.75)$$

$$Q_n = -S c_p \hat{D}_n \int_{p_t}^p h_n dp \quad (1.76)$$

## 1.5 Outline of the thesis

This study focuses on quasi-2-day waves which are the most fundamental element of the hierarchy of CCEWs. Our ultimate goal is proposing a comprehensive frame work to understand the wave-convection coupling mechanism of various CCEWs. In the present study, the coupling mechanism of quasi-2-day waves is examined by utilizing satellite and reanalysis data. The first and second parts of this study are summarized in chapter 3 and chapter 4, respectively.

In chapter 2, data and methodology used in the following analysis (chapter 3 and chapter 4) are summarized. The 2-day waves are detected by WIG filtering of brightness temperature data since they are nearly identical to convectively coupled WIG waves.

In chapter 3, the interaction between convection and the wave dynamics is examined in the thermodynamic context. Following recent investigations, moist static energy (MSE) which is nearly conserved in moist adiabatic process is used to examine the thermodynamic process during the active phase of the 2-day waves. Budget equation of vertically integrated MSE tell us about MSE recharge-discharge process associated with the wave dynamics. Further, the normalized gross moist stability (NGMS) is adopted to discuss the relationship between the large-scale circulation and convective intensity.

In chapter 4, the interaction between convection and the wave dynamics is examined in the vertical mode perspective. The large-scale fields of the 2-day waves are decomposed by a few vertical modes calculated from a mean temperature profile of reanalysis data. Phase speed of vertical modes is evaluated using the mode transform coefficients. The mechanism of slowdown of the vertical modes is examined in terms of effective static stability which is reduced by the latent heating of convective systems. Using a simple diagnostic equation, the relationship between the effective static stability and the slow phase speed is investigated for each vertical mode.

In chapter 5, a summary of the above analyses is presented.

# Chapter 2

## Data and Methodology

### 2.1 Data description

This study analysis 10-yrs (2000-2009) of satellite and reanalysis data as shown below. The analysis area is the whole tropical region between 10°N and 10°S over oceans. All satellite data are projected onto a 0.25° grid.

#### 2.1.1 Satellite data

##### IR data

IR brightness temperature (TBB) data is used to identify convective peaks of quasi-2-day waves (see sec. 2b). TBB data is obtained from Global-merged IR Brightness Temperature Data (mergedIR) Ver. 6 by [Janowiak et al. \(2001\)](#). The mergedIR is a high-resolution gridded global data in which Geostationary Operational Environmental Satellite (GOES)-8/10, Meteorological Satellite (METEOSAT)-7/5 and Geostationary Meteorological Satellite (GMS) are combined. The spatial coverage is between 60°N and 60°S. The horizontal resolution is about 0.0364° and temporal resolution is 30 min. Owing to the high temporal resolution of mergedIR, we could construct a composite time series with a time increment of 30 min (see section [2.2.4](#) for more detail).

##### TRMM PR2A25 data

The precipitation data in tropical ocean area is obtained from Tropical Rainfall Measuring Mission (TRMM) data product. TRMM satellite is launched in November 1997 and ended in April 2015. It is a sun-asynchronous satellite orbiting with an inclination angle of about 35° and carrying the Precipitation Rader (PR) which estimates vertical profile of precipitation. The horizontal and vertical resolutions of PR are about 4 km and 250 m, respectively. The near surface precipitation data in PR2A25 Level 2 Ver. 6 ([Iguchi et al. 2000](#)) is used to analyze variance in precipitation of 2-day waves.

## 2.1.2 Reanalysis data

### ERA-Interim

To analyze the environmental fields accompanied with 2-day waves, we use ERA-Interim data which is one of European Center for Medium-Range Weather Forecasts (ECMWF)'s reanalysis data (Simmons et al. 2007). The horizontal resolution is  $1.5^\circ$  and the total number of pressure levels is 38 with non-uniform pressure interval. The temporal resolution is 6 and 12 hours for three and two dimensional data, respectively. ERA-Interim variables utilized in this work are summarized as follows. 1) the 3D variables; geopotential height  $\phi$ , temperature  $T$ , specific humidity  $q$ , horizontal wind velocity  $\mathbf{V} = (u, v)$ , and pressure velocity  $\omega$ . 2) the 2D variables; surface sensible heat flux  $SH$ , surface latent heat flux  $LH$ , surface short wave flux  $SW_s$ , short wave flux at the top of the atmosphere (TOA)  $SW_t$ , surface long wave flux  $LW_s$ , and long wave flux at TOA  $LW_t$ . The analysis area is the whole tropical region between  $10^\circ\text{N}$  and  $10^\circ\text{S}$  over oceans as selected with the ERAI sea-land flag.

## 2.2 Methodology

### 2.2.1 Spectral analysis

Space-time power spectrum of the high-resolution TBB data (mergedIR) is computed in a similar manner to that used by previous studies (e.g., Wheeler and Kiladis 1999). The procedure is briefly summarized here. First, raw TBB data are averaged over the meridional band between  $10^\circ\text{N}$  and  $10^\circ\text{S}$ . Then, a longitude-time cross section of the area averaged TBB is constructed for every 2 yr between 2000 and 2009. Missing data are filled in by linear interpolation over time. Second, the mean and the linear components at each longitude are removed to obtain anomalous TBB. Third, the longitude-time cross section of the anomaly is divided into 80-day segments that consecutively overlap each other by 40 days. Therefore, a frequency resolution  $f$  is 0.0125 (1/80) cycle per day (cpd). Finally, fast Fourier transform (FFT) is performed to compute the power spectrum of anomalous TBB for each segment. Here, a split cosine bell tapering function is applied to each segment to avoid spectral leakage. The power spectrum are averaged over 10 yr between 2000 and 2009.

Figure 2.1 shows the power spectrum normalized by the background spectrum in wavenumber-frequency domain. The background spectrum is computed by smoothing many times the raw spectrum with a 1-2-1 filter in frequency only. The degree of freedom (DOF) is estimated about 91 ( $\sim 2 \times 365 \times 10/80$ ). Shading begins at a value of 1.3, which is significant at the 95 % level with 91 DOF in a chi-squared test. The spectral signals of TBB in Fig. 2.1 are consistent with those of OLR, precipitation, and precipitable water in previous studies (e.g., Takayabu 1994a; Wheeler and Kiladis 1999; Wheeler et al. 2000; Roundy and Frank 2004; Masunaga et al. 2006; Kiladis et al. 2009; Yasunaga and Mapes 2012, and many others).

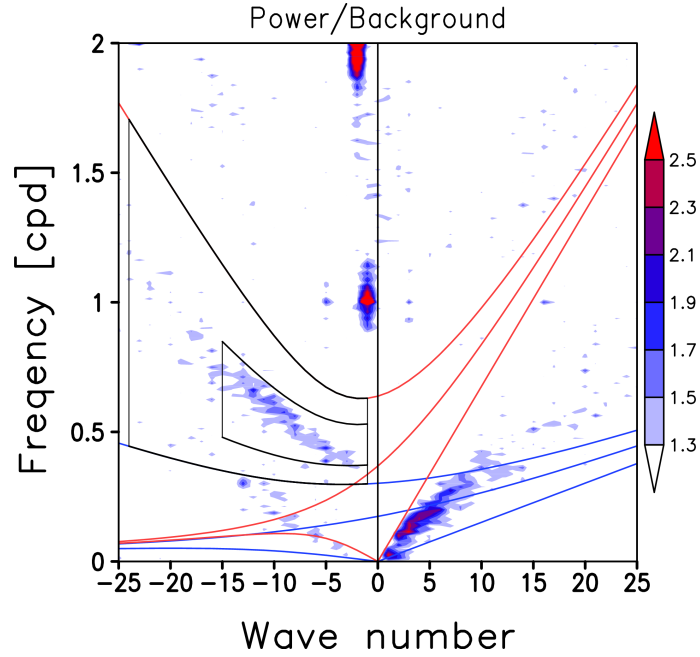


**Fig. 2.1:** The raw power spectrum normalized by the background spectrum (shade) in wave number-frequency (cycle per day; cpd) domain. A negative (positive) wave number means westward (eastward) mode. Shading begins at a value of 1.3, which is significant at the 95 % level with 91 degrees of freedom (DOF). The colored lines represent the dispersion relationships of various equatorial waves for different equivalent depth of 5 m (blue) and 100 m (red); inertia gravity wave ( $n = 1$ ), Rossby wave ( $n = 1$ ), mixed Rossby wave ( $n = 0$ ), and Kelvin wave ( $n = -1$ ). The large black frame represents the WIG filter used in this study, including  $k=1-24$  and  $h_e = 5-100$  m.

### 2.2.2 Filtering analysis

Filtering analysis is performed to isolate individual CCEWs (e.g., [Wheeler and Kiladis 1999](#)), where the filtering boxes are defined in the wavenumber-frequency domain based on the dispersion curves of dry equatorial waves derived by [Matsuno \(1966\)](#). This approach is applied to the present study with some minor modifications as described below.

In the present study, convective peak of a quasi-2-day wave is identified by filtering TBB. It is assumed that convectively coupled WIG wave is a practical indicator of 2-day wave. First, a longitude-time cross section of TBB averaged over meridional band ( $10^\circ\text{N}-10^\circ\text{S}$ ) is constructed for every 2 years between 2000 and 2009. Missing data are filled in by linear interpolation over time, and then the mean and the linear components at each longitude are removed. Second, we apply fast Fourier transform to the time series of anomalous TBB by utilizing a split cosine bell tapering function to avoid spectral leakage. Third, WIG filter (the filter design is described below) is applied to a wavenumber-frequency domain to isolate individual WIG wave. Finally, the filtered TBB is transformed back to the longitude-time domain.

WIG filter is often defined as a wavenumber-frequency domain bounded by two dispersion curves of WIG wave, including  $k = 1 - 14$  and  $h_e = 12 - 50$  m (e.g., [Wheeler](#)

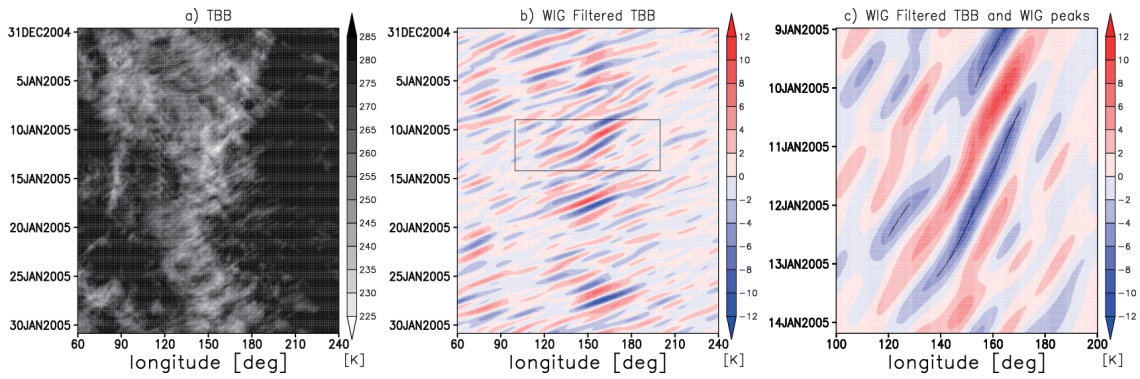


**Fig. 2.2:** A longitude-time cross section of (a) raw TBB, (b) WIG filtered TBB, and (c) WIG filtered TBB and WIG peaks (black dot). In (c), the area surrounded by a black box in (b) is displayed in large size. The longitudinal band is between  $60^{\circ}\text{E}$  and  $120^{\circ}\text{W}$ . The time period is between 2004/12/31 and 2005/1/31.

and Kiladis 1999). In the present study, WIG filter used in chapter 3 is defined as a somewhat broader region including  $k = 1 - 24$  and  $h_e = 5 - 100$  m (black box in Fig. 2.1). It is confirmed that the filter includes the prominent WIG signals ( $k \sim 1 - 15$  and  $f \sim 0.4 - 0.8$ ) in Fig. 2.1. Some recent studies have reported that the spectral signal of WIG waves extends over a wider region in the higher frequencies and wave numbers (Tulich and Kiladis 2012; Kikuchi 2014). Based on TRMM 3B42 precipitation product, Tulich and Kiladis (2012) shows that the significant signal of westward disturbances is seen up to zonal wavelength of about 500 km and period of about 8 h, corresponding to the meso-alpha scale. Such a small and fast disturbances are excluded in this study to avoid their contamination to the WIG filtering. The TD signals (e.g., Kiladis et al. 2006) may appear below the lower boundary of the WIG filter near  $f = 0.2 - 0.4$ . However, TD-type disturbances are unlikely to have significant influence on this analysis. Finally, the same filter defined in Wheeler and Kiladis (1999) is tested to verify the justification for the filter in this study. The following results are insensitive to the difference in the filter design (not shown here).

Figure 2.2 is the longitude-time cross section during the period between December 2004 and January 2005 for an example to show how the filtering works. Unfiltered TBB (Fig. 2.2a) shows that a synoptic-scale envelope of active convection is prominent between the Indian Ocean (IO) and western Pacific Ocean (WP), while 2-day disturbances are only barely discernible. Westward propagating 2-day waves are clearly captured in the WIG filtered TBB (Fig. 2.2b), particularly striking in the western Pacific between  $140^{\circ}\text{E}$  and  $180^{\circ}$ .

In chapter 4, we further define five sub-filters with different equivalent depth in order to isolate the waves moving at different phase speed (Fig. 2.3). The sub-filters are denoted by h5/15, h15/25, h25/35, h35/45, and h45/55 in the order of increasing equivalent depths. For the filter h5/15, the upper and bottom boundaries are set at  $h_e = 5$  m and  $h_e = 15$  m, respectively. A range of wave number  $k = 1 - 14$  is common among the sub-filters. Yasunaga and Mapes (2014) separates the faster and slower components of CCEW by using two filtering box with different equivalent depth, where region including  $h_e = 20 -$

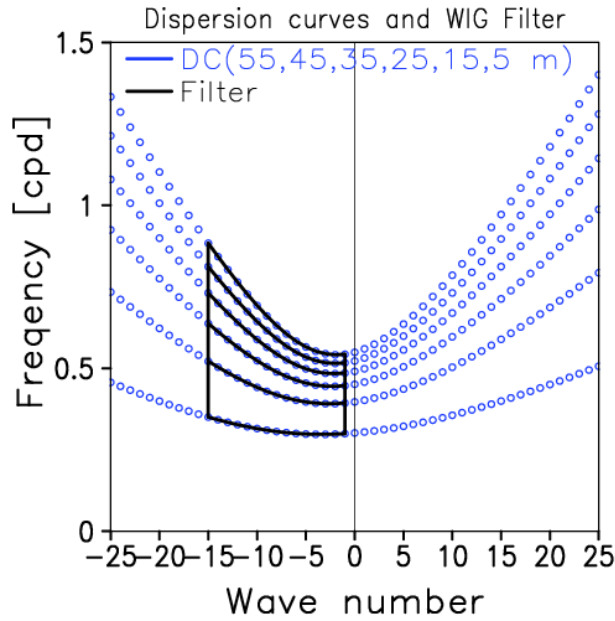


**Fig. 2.3:** Five sub-filters with different equivalent depth which are used in chapter 4. See more description in section 2.2.2.

25 m is excluded to reduce the cross contamination from other components. As the five filters defined above are adjacent each other, any contamination could be occurred. It is noted, however, that WIG waves with different phase speed are isolated well as shown in section 4.2.

### 2.2.3 Definition of the peak of WIG wave

A convective peak of WIG waves (hereafter WIG peak) is detected by using a longitude-time cross section of filtered TBB. First, the standard deviation(SD) of filtered TBB is computed from the longitude-time cross section with the sample number of about 50457600 ( $\sim 2 \times 365 \times 48 \times 360^\circ / 0.25^\circ$ ) for each 2 yr. Second, zonal local minima of filtered TBB are searched at each time by moving a searching box, with a zonal length of  $20^\circ$ , in zonal zonal direction. Only a minimum locating at the center of the searching box is picked up to ignore noisy fluctuations. Third, the local minima colder than  $-2$  SD are defined as the longitudinal location of convective peaks of WIG waves (WIG peak). This threshold is used to prevent the composite wave structures from being contaminated by irrelevant background convective signals. Finally, the longitude of the convective peak is defined as a meridional local minimum of raw TBB between  $10^\circ\text{N}$  and  $10^\circ\text{S}$ .

The total number of WIG peaks is 355491 in 10 yr between 2000 and 2009. Figure 2.2c shows that the peaks (black dot) distribute along the WIG ridges where the zonal minimum of filtered TBB are colder than  $-2$  SD. Robust wave signals with active convection are likely to be captured, while relatively weak and noisy signals are excluded. Figure 2.4 shows the geographic distribution of WIG peaks. The waves are most frequently observed in the Indo-Pacific Ocean region and Africa, as shown in the previous

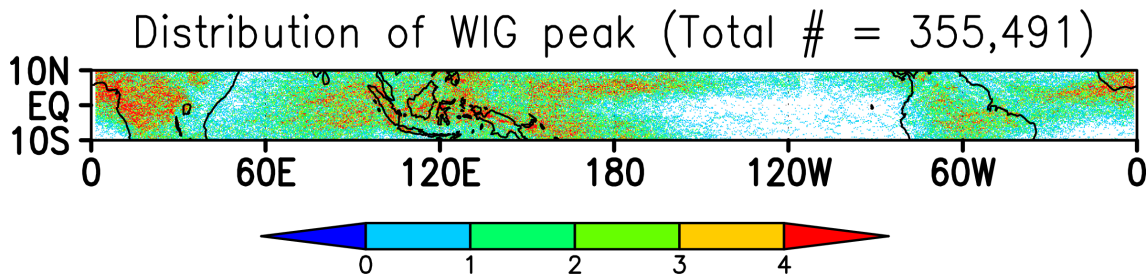


**Fig. 2.4:** Geographic distribution of WIG peaks detected by the method in section 2.2.3. The total peak number is 355,491.

works. It is noted that only peaks in the ocean are used in the composite analysis.

### 2.2.4 Composite analysis

The composite analysis is performed to investigate observational features of WIG waves. It should be noted that there exists a technical problem as described below. The WIG wave accompanies with an individual convective event with a period from a few hours to one day. Such a fast evolution process is unable to be tracked continuously by orbiting satellite and reanalysis data due to their coarse temporal sampling. For example, daily observational frequencies are four times (6 hourly) and less than two times in reanalysis data and low-Earth-orbiting(LEO) satellite data, respectively. To avoid this technical problem, [Masunaga \(2012a\)](#) proposed a new composite technique to statistically construct fast temporal variations in the atmosphere. In his technique, two LEO satellite datasets with different observational time are combined, where the time axis is defined as their observational time difference: the composite base points are detected by using TRMM data and the other LEO data are composited around them (see Fig. 2 in [Masunaga 2012a](#)). A huge number of the base points are needed to construct a statistically continuous time series because individual base points only provide discrete snapshots due to a coarse time resolution of the composited data.

A similar technique is applied to the present study. First, the peak of WIG wave, identified from filtering TBB data (mergedIR), is defined as a base point of composite. Second, a long time period of satellite and reanalysis data are composited around the base point to obtain the statistical continuous time series. The composite time is the observational time difference between mergedIR and the composited data, which is sorted by 0.5-hourly bins. This high temporal resolution of the composite filed is achieved because the base points are identified by 0.5-hourly merged IR data. As definition, the composite time 0 h corresponds to the timing when the WIG wave has the minimal TBB.

### 2.2.5 Radon transform

Phase speed of CCEW is often calculated as a regression coefficient of the peaks of anomalies in a longitude-time domain (e.g., [Wheeler et al. 2000](#)). Radon transform (RT) method has been sometimes used to evaluate propagation speeds of CCEWs and organized cloud systems ([Yang et al. 2007b](#); [Dias and Pauluis 2011](#); [Dias et al. 2012](#)).

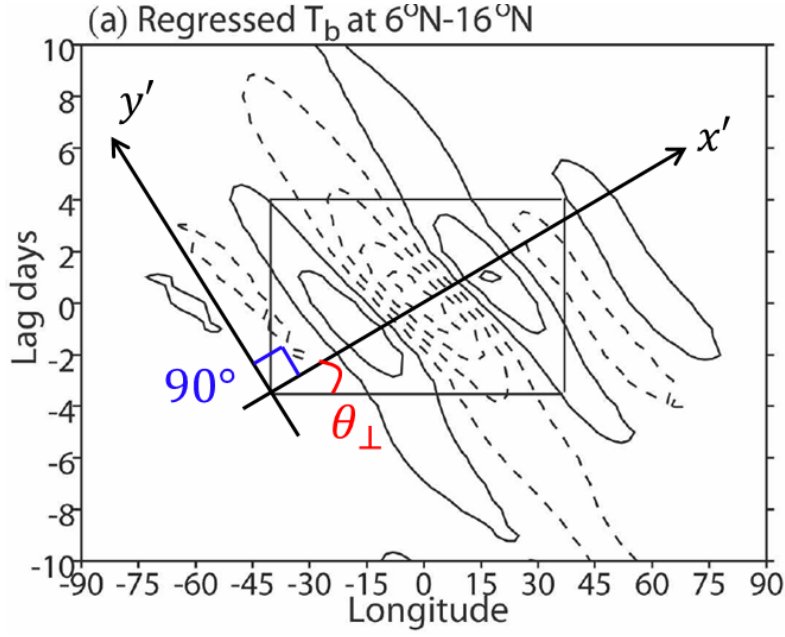


**Fig. 2.5:** A longitude-time cross section of anomalous brightness temperature. Solid (dashed) lines denote positive (negative) anomalies. The energy of the projected data has a maximum amplitude at angle  $\theta_{\perp}$  perpendicular to the ridges and troughs. The wave propagates at the direction of angle  $\theta_{\perp} + 90^{\circ}$ . From Yang et al. (2007b).

The RT, a method described as “a more objective way to obtain phase speed” by Yang et al. (2007b), is adopted in the present study to estimate propagation speeds of the WIG waves and the moist vertical modes. It should be noted that the obtained speed is not so sensitive to differences in the evaluation methods (not shown here).

We briefly summarize the procedure here (see appendix in Yang et al. (2007b) for more details). The anomalous field of longitude-time domain  $(x, t)$  is projected along a line at angle  $\theta$  with respect to the  $x$  axis (Fig. 2.5). Equation of RT is written as follows:

$$P(x', \theta) = \int_{y'} f(x, y) dy' \quad (2.1)$$

where

$$\begin{pmatrix} x' \\ y' \end{pmatrix} = \begin{pmatrix} \cos\theta & \sin\theta \\ -\sin\theta & \cos\theta \end{pmatrix} \begin{pmatrix} x \\ y \end{pmatrix} \quad (2.2)$$

When the line at angle  $\theta$  is perpendicular to the ridges and troughs of the wave in the course of varying  $\theta$  from  $0^{\circ}$  to  $180^{\circ}$ , the energy of the projected data would have a maximum amplitude;  $P(x', \theta)$  has a maximum variance ( $\sum_{x'} P^2(x', \theta)$  is maximized at  $\theta_{\perp}$ ). With this angle denoted by  $\theta_{\perp}$ , the angle perpendicular to the projection angle ( $\theta_{\perp} + 90^{\circ}$ ) gives the wave propagation direction in the longitude-time domain. The phase speed is calculated as the slope of the propagation direction;

$$c \sim \frac{\Delta x \times 100 \times 1000}{\Delta y \times 3600} \frac{1}{\tan(\theta_{\perp} + 90^{\circ})} \quad (2.3)$$

where  $c$  is phase speed [ $\text{m s}^{-1}$ ],  $\Delta x$  and  $\Delta y$  are resolution of space and time, respectively. As will be shown in chapter 4,  $\Delta x = 0.25^\circ$  and  $\Delta y = 0.5 \text{ h}$  in Fig. 4.1a.

## 2.2.6 Vertical mode

Numerical methods to calculate normal modes in the atmosphere have been proposed in different ways (Kasahara and Puri 1981; Dias et al. 1983; Fulton and Schubert 1985). This study adopts the method proposed in Fulton and Schubert (1985) where the vertical modes are derived from primitive equation system in pressure coordinate (see section 1.4 for more detail). This method has been widely used in observational and theoretical investigations of CCEWs and meso-scale convective systems (Mapes and Houze Jr 1995; Mapes 1998; Haertel and Johnson 1998; Haertel and Kiladis 2004; Khouider and Majda 2006b; Tulich et al. 2007; Tulich and Mapes 2008; Haertel et al. 2008; Kuang 2008a; Tulich and Mapes 2010; Tulich and Kiladis 2012).

The vertical mode is obtained by solving a discrete eigenvalue equation (Eq. (1.67));

$$-\frac{\partial}{\partial p} \frac{p}{\bar{S}R} \frac{\partial}{\partial p} h_n(p) = c_n^2 h_n(p) \quad (2.4)$$

where  $\bar{S} = R\bar{T}/pc_p - \partial\bar{T}/\partial p$  is static stability of basic state (over bar denotes temporal and area average),  $h_n(p)$  is a normalized structure function of the  $n$ -th dry vertical mode, and  $c_n$  is the phase speed. Note that  $h_n(p)$  consists of a normalized orthogonal system. Eq. (2.4) is solved by applying rigid upper boundary condition. To compute numerical solutions of the vertical modes, we rewrite the eigenvalue equation, the boundary condition, and the normalized condition in a finite difference form. First, pressure coordinate is represented in a discrete form. Second, the eigenvalue equation and the boundary condition are represented in a finite difference form, where the eigenfunction is written in a matrix form. Third, the normalized condition in a difference form is described.

### Pressure coordinate in a discrete form

Figure 2.6 shows a pressure coordinate with  $(M + 1)$  layers in a discrete form. Each of the layers has a uniform thickness of  $\Delta p$  and is labeled by an integer index  $k$  ( $k = 0, \dots, M$ ). The  $k$ -th layer is placed between two pressure levels  $p = p_{k-1/2}$  and  $p = p_{k+1/2}$ , and is centered at  $p = p_k$ . The index of the upper and bottom boundaries are  $k = -1/2$  and  $k = M + 1/2$ , respectively. In this analysis,  $p_t = 100 \text{ hPa}$ ,  $p_b = 1000 \text{ hPa}$ ,  $\Delta p = 25 \text{ hPa}$ , and  $M = 35$ .

### Eigenvalue equation, boundary condition, and normalized condition

The eigenvalue equation and boundary conditions are summarized as follows;

$$\begin{aligned} -\frac{\partial}{\partial p} \mu \frac{\partial}{\partial p} h_n &= \lambda_n h_n \\ \left( \frac{\partial h_n}{\partial p} \right)_{p_t} &= 0 \\ \left( \frac{\partial h_n}{\partial p} \right)_{p_b} + \left( \frac{S h_n}{\bar{T}} \right)_{p_b} &= 0 \end{aligned} \quad (2.5)$$

where  $\mu = p/SR$ . Let us denote  $h_n(p_k)$  and  $\mu_n(p_{k+1/2})$  as  $h_{n,k}$  and  $\mu_{n,k+1/2}$ , respectively (Fig. 2.7). The latter is the mean values of  $\mu$  between pressure levels  $k$  and  $k + 1$ . The discrete form of Eqs. (2.5) is given as follows (see section 6.3 and 6.5):

$$-\frac{\mu_{k-1/2}h_{n,k-1} - (\mu_{k-1/2} + \mu_{k+1/2})h_{n,k} + \mu_{k+1/2}h_{n,k+1}}{\Delta p^2} = \lambda_n h_{n,k} \quad (2.6)$$

$$h_{n,-1} = h_{n,0} \quad (2.7)$$

$$h_{n,M+1} = bh_{n,M} \quad (2.8)$$

where  $b = (1 - a)/(1 + a)$  and  $a = \Delta p(S/\bar{T})_{M+1/2}$ .

Substituting Eqs. (2.7) into (2.6) for  $k = 0$  eliminates  $h_{n,-1}$  from (2.6). Substituting Eqs. (2.8) into (2.6) for  $k = M$  eliminates  $h_{n,M+1}$  from (2.6). Simplifying Eq. (2.6) for  $k = 0, \dots, M$ , we obtain the eigenvalue equation in a matrix form:

$$\hat{\mathbf{L}}\mathbf{h}_n = \lambda_n \mathbf{h}_n \quad (2.9)$$

where  $\hat{\mathbf{L}}$  is a difference operator matrix:

$$\hat{\mathbf{L}} = \begin{pmatrix} \frac{\mu_{1/2}}{\Delta p^2} & -\frac{\mu_{1/2}}{\Delta p^2} & 0 & 0 & \dots & 0 \\ -\frac{\mu_{1/2}}{\Delta p^2} & \frac{\mu_{1/2} + \mu_{3/2}}{\Delta p^2} & -\frac{\mu_{3/2}}{\Delta p^2} & 0 & \dots & 0 \\ \vdots & -\frac{\mu_{k-1/2}}{\Delta p^2} & \frac{\mu_{k-1/2} + \mu_{k+1/2}}{\Delta p^2} & -\frac{\mu_{k+1/2}}{\Delta p^2} & & \vdots \\ 0 & \dots & 0 & -\frac{\mu_{M-3/2}}{\Delta p^2} & \frac{\mu_{M-3/2} + \mu_{M-1/2}}{\Delta p^2} & -\frac{\mu_{M-1/2}}{\Delta p^2} \\ 0 & \dots & 0 & 0 & -\frac{\mu_{M-1/2}}{\Delta p^2} & \frac{\mu_{M-1/2} + \mu_{M+1/2}(1-b)}{\Delta p^2} \end{pmatrix}$$

and the eigenfunction  $\mathbf{h}_n$  is written as

$$\mathbf{h}_n = (h_{n,0}, h_{n,1}, \dots, h_{n,k}, \dots, h_{n,M-1}, h_{n,M})^t$$

$\hat{\mathbf{L}}$  is a tridiagonal matrix and also identifies with a Hermitian matrix as described in sec. 1.4.3. Solving Eq. (2.9), we obtain  $(M + 1)$  eigenfunctions  $\mathbf{h}_n$  and  $(M + 1)$  eigenvalues  $\lambda_n$ . The normalized condition in the difference form is given by

$$\frac{1}{(M + 1)\Delta p} \sum_{k=0}^M h_{n,k}^2 \Delta p = 1 \quad (2.10)$$

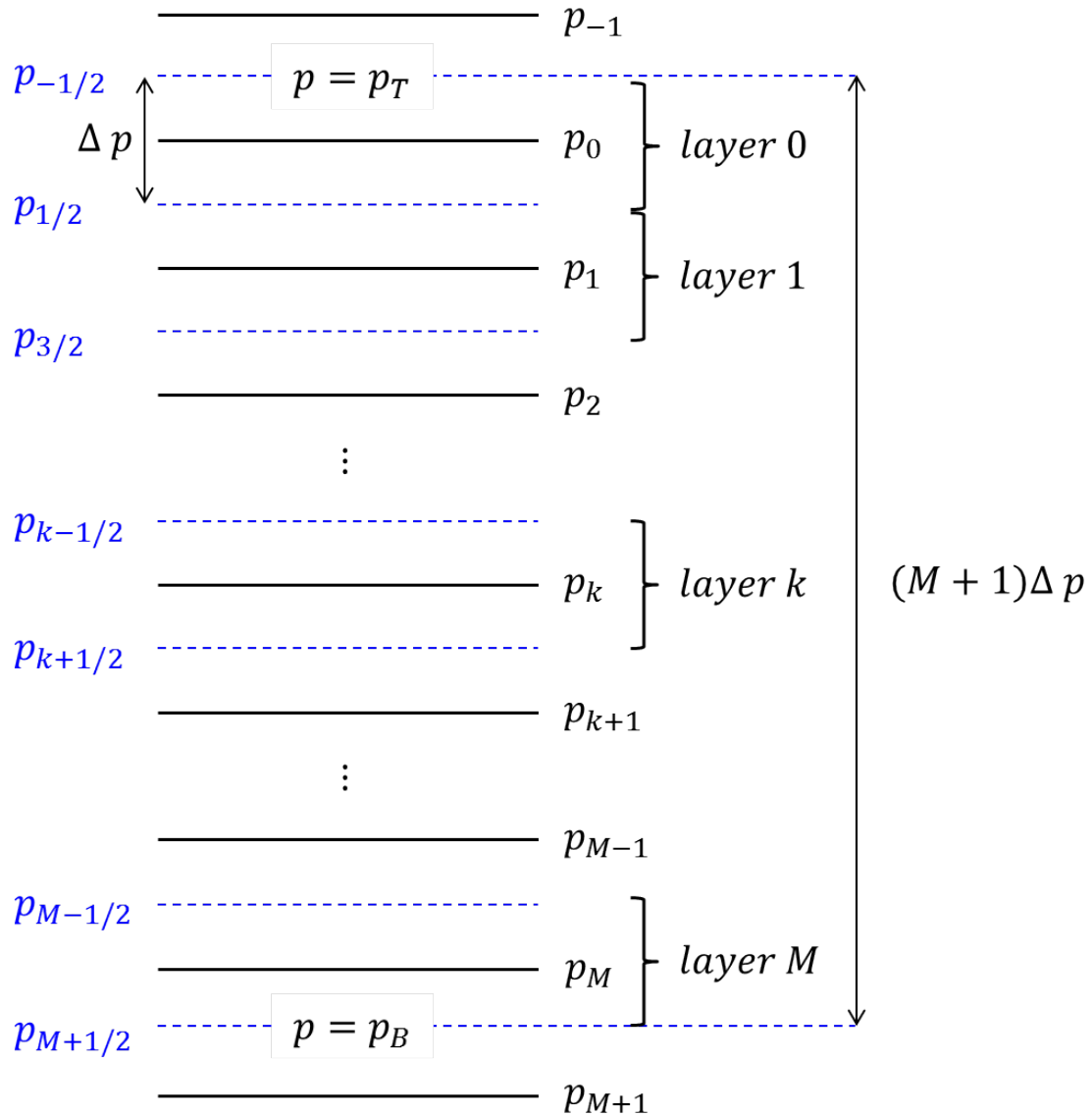


**Fig. 2.6:** Pressure coordinate with  $(M + 1)$  layers between  $p_T$  and  $p_B$ . The layers are uniformly separated with a thickness of  $\Delta p$ . The center of  $k$ -th layer is at level  $p = p_k$  and is labeled by integer index  $k$  (black solid lines:  $k = 0, \dots, M$ ). The  $k$ -th layer is placed between two pressure levels,  $p = p_{k-1/2}$  and  $p = p_{k+1/2}$ , labeled by semi-integer index (blue dashed lines). The index of the upper and bottom boundaries are  $k = -1/2$  and  $k = M + 1/2$ , respectively.

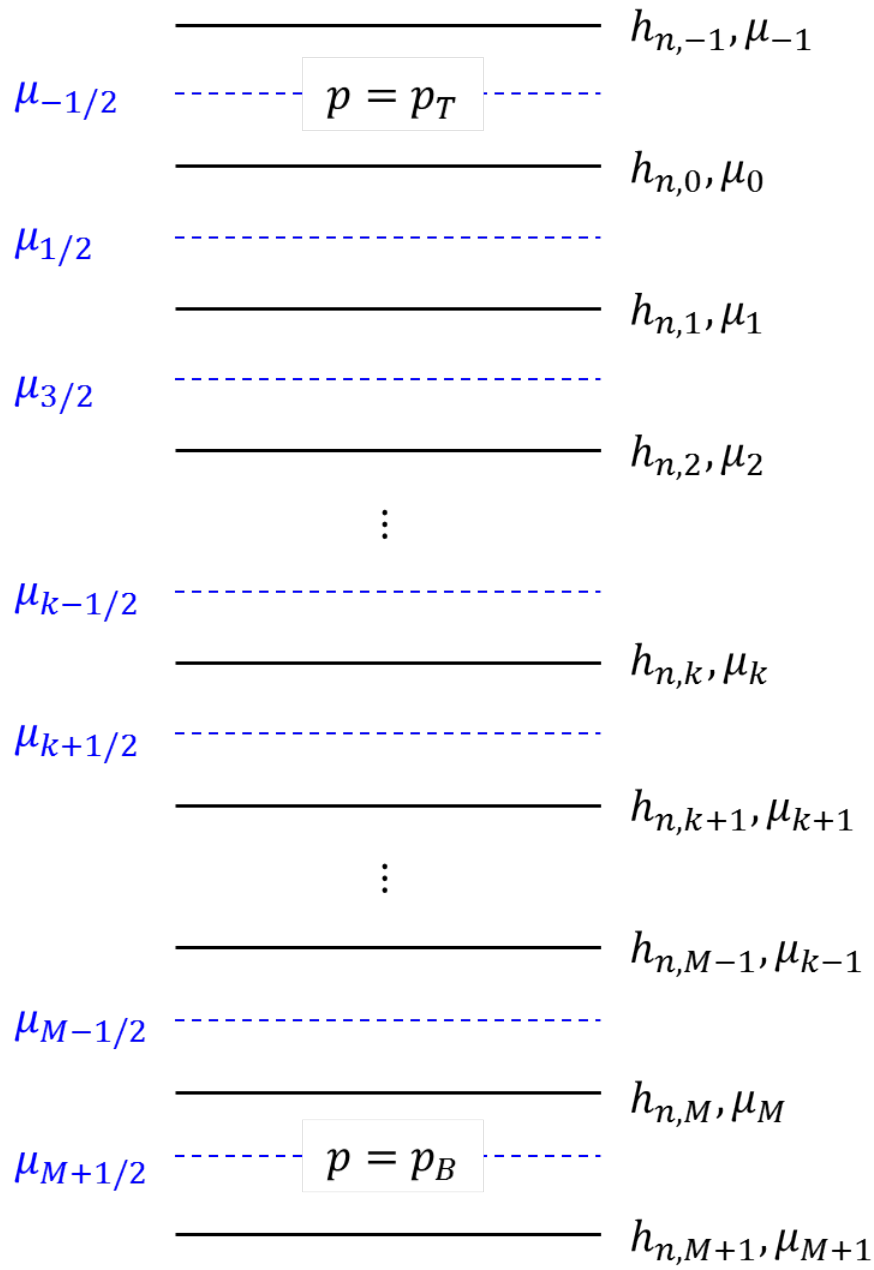


**Fig. 2.7:** Same as Fig. 2.6, but for discrete representation of  $h_n$  and  $\mu$ .  $\mu_{k+1/2}$  denotes the mean value of  $\mu$  between the levels  $k$  and  $k + 1$ .  $u, v, \phi, \omega, T, Q$

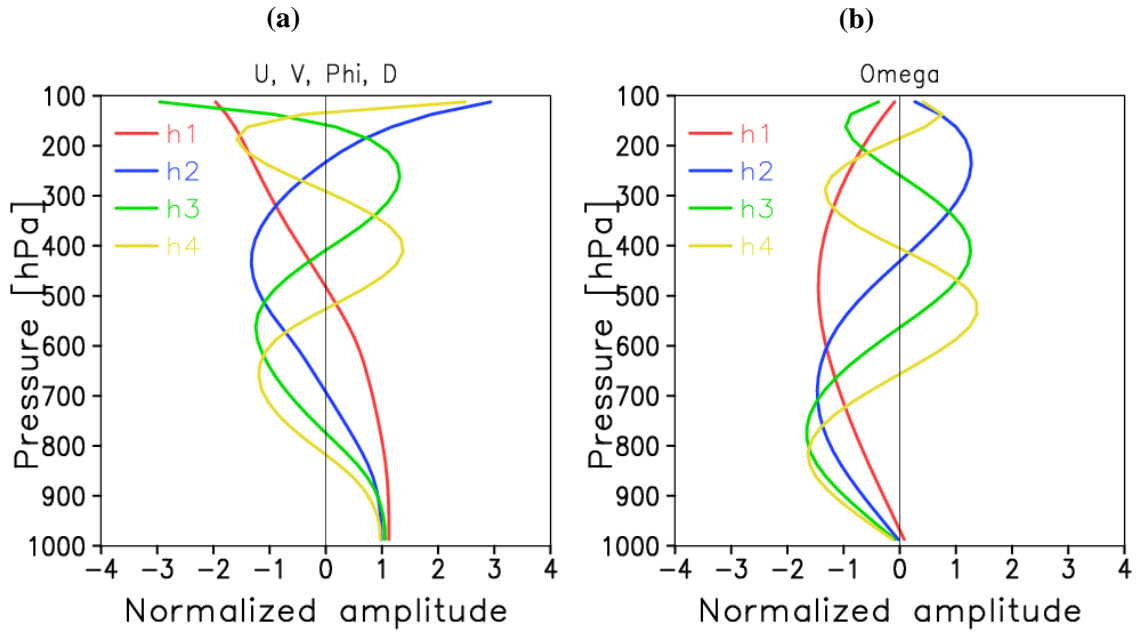


**Fig. 2.8:** Structure functions of the first four baroclinic modes for (a)  $h_n$  and (b) omega. Different color denote different modes.

### Vertical modes calculated from ERAI data

In this study, we select  $p_t = 100$  hPa and  $p_b = 1000$  hPa following previous studies (e.g., [Haertel et al. 2008](#); [Tulich and Kiladis 2012](#)). The pressure coordinate between  $p_t$  and  $p_b$  is divided into 36 layers with a uniform thickness of 25 hPa. Therefore, total number of vertical modes is 36 ( $n = 0 \sim 35$ ). ERAI variables in pressure coordinate (between  $p_t$  and  $p_b$ ) are also vertically interpolated with uniformly spacing (25 hPa) by cubic spline interpolation.  $\bar{T}$  is calculated as a temporal-domain averaged temperature of ERAI data between  $10^\circ\text{N}$  and  $10^\circ\text{S}$  in 10 yrs (2000-2009). The profile is insensitive to regional and temporal differences (not shown here).

Figure 2.8a shows the structure function of the first four baroclinic modes calculated in this study. The  $n$ -th mode has the  $n$  nodes. Figure 2.8b shows the structure function of  $\omega$  calculated from Eq. (6.30). The lower mode has faster phase speed (deeper equivalent depth). For the first four modes, the phase speeds are 52, 27, 20, and 15  $\text{m s}^{-1}$ . The equivalent depth ( $H_n = c_n^2/g$ ) are 274, 75, 39, and 23 m. The phase speed and equivalent depth are almost consistent with that calculated with the same boundary condition in previous studies. For example, [Tulich and Kiladis \(2012\)](#) using ERA-Interim data showed that phase speeds of the first four modes are 51, 22, 18, and 14  $\text{m s}^{-1}$ . [Haertel et al. \(2008\)](#) using TOGA-COARE data shows that phase speeds of the first tree modes are 52, 26, and 19  $\text{m s}^{-1}$ . It is also confirmed that pressure levels of the peaks and nodes of each vertical mode are roughly consistent with that in the previous studies.

# Chapter 3

## Thermodynamic process of quasi-2-day wave

### 3.1 Goal of this chapter

In this chapter, the relationship between convection and 2-day wave dynamics is examined. Following recent investigations (see section 1.2.2), budget equation of column MSE is applied to the composite WIG waves, where the budget terms are calculated from ERAI data. MSE recharge-discharge process is discussed comparing with that in multi-mode model. The goal of this chapter is to reveal a role of tropospheric moisture in the coupling mechanism.

### 3.2 Gross features of composite WIG waves

In this section, the horizontal structure and propagation character of the composite WIG waves are described. Figure 3.1 shows the horizontal structure of anomalous TBB, precipitation, geopotential height, and horizontal wind during a sequence of WIG phases. Anomalies represent the deviation from the temporal mean over  $\pm 48$  hour in the composite time series, which are computed by subtracting the mean from the value at each grid point in Fig. 3.1. The computing method of anomaly is similar to that used in the previous studies (Takayabu et al. 1996; Benedict and Randall 2007). Shade and arrows in Fig. 3.1 are plotted only where statistically significant at the 95% level as tested by the Student's t-test.

The area with a negative TBB anomaly (convective active area) has a zonal scale of about 1000 km (Fig. 3.1a). Therefore, the zonal wavelength of the composite WIG wave is estimated about 2000 km, corresponding to that of COARE 2-day wave (Takayabu 1994b; Takayabu et al. 1996; Haertel and Johnson 1998; Haertel and Kiladis 2004). The convective envelope moves westward with a period of about 2 days and has a minimum TBB around 0 hour by definition. The propagation speed of the composite WIG waves is estimated to be about  $17 \text{ m s}^{-1}$  given that the convective active area moves over about  $30^\circ$  in 48 hours, which is nearly consistent with that of COARE-2-day waves ( $10\text{-}30 \text{ m s}^{-1}$ ) as mentioned in section 3.4.3. The TBB minimum lags the precipitation maximum by a few hours, which is consistent with the previous studies (Takayabu et al. 1996; Haertel

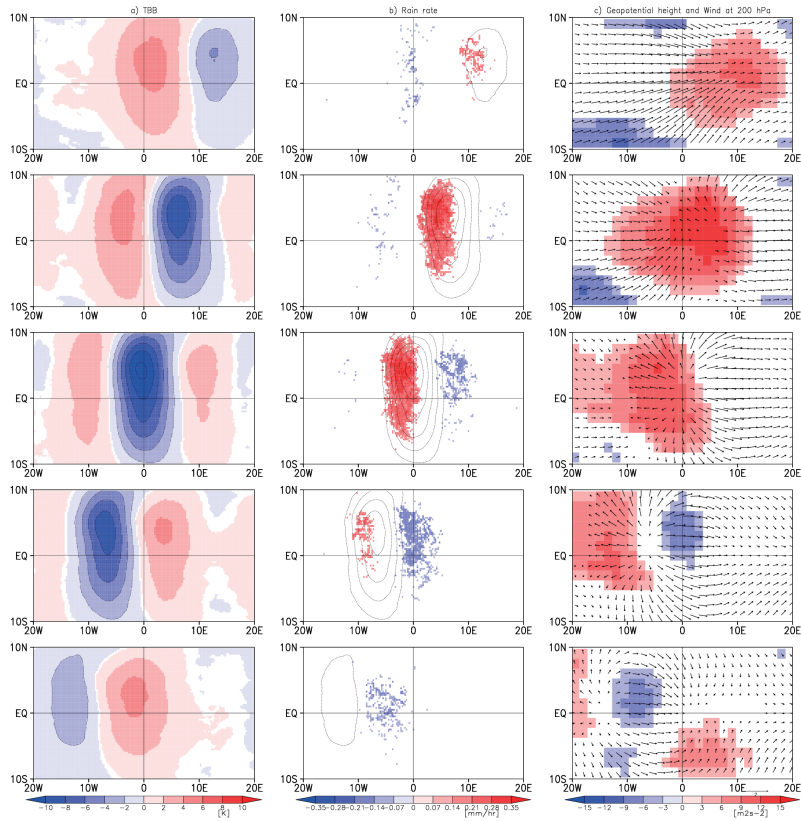


**Fig. 3.1:** 12-hourly snapshots of the horizontal structure of the composite WIG waves; (a) anomalous TBB, (b) anomalous precipitation, (c) anomalous geopotential height (shade) and horizontal wind (vector) at 200 hPa. Negative anomaly of TBB is represented by contour in (a) and (b). Anomalies are computed by subtracting time mean value during  $\pm 48$  hour in the composite time series from the values at each grid point. Shades and arrows indicate significant regions at the 95 % level. The horizontal axis is a relative longitude between  $-20^\circ$  and  $+20^\circ$ . The vertical axis is latitude between  $10^\circ\text{N}$  and  $10^\circ\text{S}$ . Time increase downward from  $-24$  hr to  $+24$  hr with a time increment of 12 hour.

and Johnson 1998; Haertel and Kiladis 2004). The somewhat noisy distribution of precipitation anomaly (Fig. 3.1b) is likely to result from the small sample size of PR2A25 data, because TRMM satellite has less than twice daily observations at the same location. The synoptic-scale structure of geopotential height and wind at 200 hPa is roughly identical to that of the theoretical  $n = 1$  WIG waves derived by Matsuno (1966) in that divergence and convergence are on the left and right, respectively, of the low pressure field (Fig. 1.17). The negative TBB anomaly is almost in quadrature with the geopotential height and is in phase with the wind divergence field.

The convective center of the composite WIG waves is shifted away from the equator to around  $5^\circ\text{N}$  (Fig. 3.1a). This could result from the effect of ITCZ, which is located near the equator (Indian Ocean; IO) and off the equator around  $7^\circ\text{N}$  (Pacific Ocean). In fact, the WIG convective center appears around  $7^\circ\text{N}$  in WP and around  $0^\circ$  in IO (not shown). The horizontal structure of geopotential height and wind is offset to the north of the equator (Fig. 3.1c), while that of theoretical  $n = 1$  WIG is equatorial symmetric,

probably due to the same reason as mentioned above.

The horizontal and vertical structures are nearly identical between the Indian and Pacific Oceans (not shown here). A secondary difference is that a maximum height of convection is lower in the east Pacific than in the indo-west Pacific, which could be explained by the regional difference of the tropical large-scale circulation (e.g., [Back and Bretherton \(2006\)](#)).

### 3.3 MSE budget analysis

#### 3.3.1 Budget analysis

In this section, thermodynamic process of 2-day waves is examined by using moist static energy (MSE) which is nearly conserved in moist adiabatic processes (see section [1.2.2](#)). MSE is defined as

$$m = s + Lq \quad (3.1)$$

where  $m$  is MSE,  $s = \phi + c_p T$  is dry static energy (DSE),  $L$  is the latent heat of condensation ( $2.5 \times 10^6$  J/kg), and  $c_p$  is dry air heat capacity at constant pressure (1004 J/K/kg). The budget of MSE is expressed as (see more description in section [6.6](#))

$$\partial_t m = -\mathbf{V} \cdot \nabla m - \omega \partial_p m + Q_R + \partial_p(s'\omega') + \partial_p(Lq'\omega') \quad (3.2)$$

where MSE eddy term is sum of radiative heating  $Q_R$  and eddy transports of latent heat flux  $\partial_p(q'\omega')$  and sensible heat flux  $\partial_p(s'\omega')$ . The budget of column-integrated MSE is expressed as

$$\langle \partial_t m \rangle = -\langle \mathbf{V} \cdot \nabla m \rangle - \langle \omega \partial_p m \rangle + \langle Q_R \rangle + SH + LH \quad (3.3)$$

Here, angle brackets denotes mass-weighted vertical integration from the top of the atmosphere ( $p_t$ ) to the surface pressure ( $p_s$ ):

$$\langle A \rangle = \frac{1}{g} \int_{p_t}^{p_s} A dp \quad (3.4)$$

where  $p_s = 1000$  hPa and  $p_t = 100$  hPa. The lhs of Eq. (3.3) is the MSE tendency term. The first and second terms on the rhs of Eq. (3.3) represent horizontal MSE advection (HADV) and vertical MSE advection (VADV), respectively. The other terms are the MSE source terms.  $\langle Q_R \rangle$  is column integrated radiative heating and calculated as the difference in net radiative flux between the surface and top of the atmosphere:

$$\langle Q_R \rangle = SW_t \downarrow - SW_t \uparrow - SW_s \downarrow + SW_s \uparrow - LW_t \uparrow - LW_s \downarrow + LW_s \uparrow \quad (3.5)$$

where the variables are defined in section [2.1.2](#) and upward (downward) arrow represent upward (downward) flux. LH and SH represent latent and sensible heat flux at surface pressure, respectively. These fluxes at TOA are 0, where  $\omega$  is assumed to be vanished. The budget equation of column MSE tells us the MSE recharge-discharge process associated with the large-scale circulation.

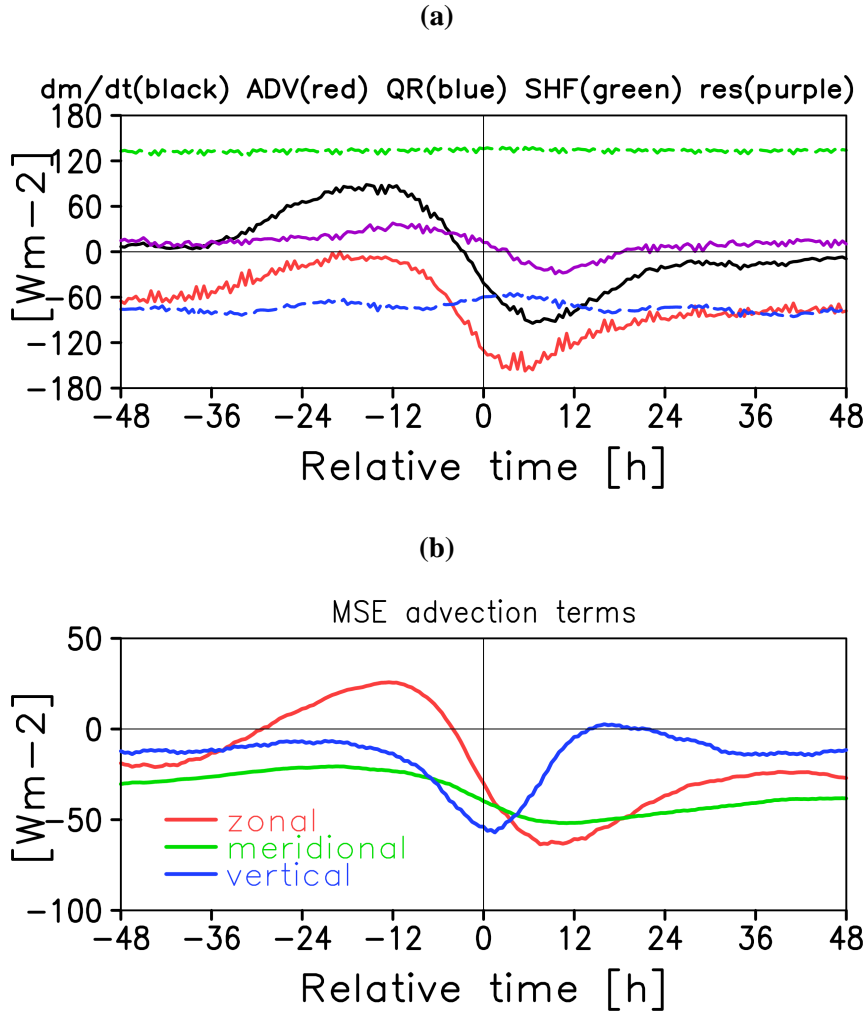


**Fig. 3.2:** (a) Composite time series of integrated MSE budget terms. The MSE tendency (black), total MSE advection (red), surface flux (green), radiative heating (blue), and the budget residual (purple). The residual is computed by subtracting the right hand side from the left hand side of the budget equation. (b) Same as in Fig. 3.2a, but for zonal (red), meridional (green), and vertical (blue) MSE advection.

Figure 3.2a shows the composite time series of the integrated MSE budget terms. The tendency term has a maximum of  $100 \text{ W m}^{-2}$  before the WIG peak ( $\sim -15 \text{ hr}$ ) and a minimum of  $-100 \text{ W m}^{-2}$  after the peak ( $\sim +5 \text{ hr}$ ). This suggests that MSE increase (recharge process) and MSE decrease (discharge process) occur before and after deep convection, respectively. Variation in the total MSE advection term (HADV+VADV) is responsible for that in the tendency term. The advection increases MSE import in the column before deep convection and approaches its maximum of 0 around  $-15 \text{ hr}$ . It increases MSE export as convection develops and reaches its minimum after the WIG peak. On the other hand, MSE source terms are almost unchanged during the active convection: Radiative and surface fluxes stay nearly constant at  $-60 \text{ W m}^{-2}$  ( $LW=-180 \text{ W m}^{-2}$  and  $SW=120 \text{ W m}^{-2}$ ) and  $+130 \text{ W m}^{-2}$  ( $SH=20 \text{ W m}^{-2}$  and  $LH=110 \text{ W m}^{-2}$ ), respectively. The budget residual is calculated by subtracting the rhs from the lhs in Eq. (3.3). It is roughly in phase with the tendency term and the amplitude is smaller, which may be attributed

to uncertainties of reanalysis data, including 1) the convection and cloud parameterizations used in the data assimilation and 2) the coarse spatiotemporal resolution. Although the budget analysis using ERA-Interim data is not closed, the MSE recharge-discharge process of WIG wave is mainly regulated by the MSE advection.

Total advection is separated into the horizontal and vertical components (Fig. 3.2b). A striking increase in negative VADV occurs around WIG peak within  $\pm 12$  hr. This may correspond to an increase in MSE export due to the strong ascent with deep convection (the first baroclinic mode). HADV is further separated into the zonal and meridional components ( $-\mathbf{V} \cdot \nabla m = -u\partial_x m - v\partial_y m$ ). Zonal advection shows a striking variability and is nearly in phase with the tendency term. It increases MSE import before deep convection and MSE export as convection develops. On the other hand, meridional advection has a small amplitude.

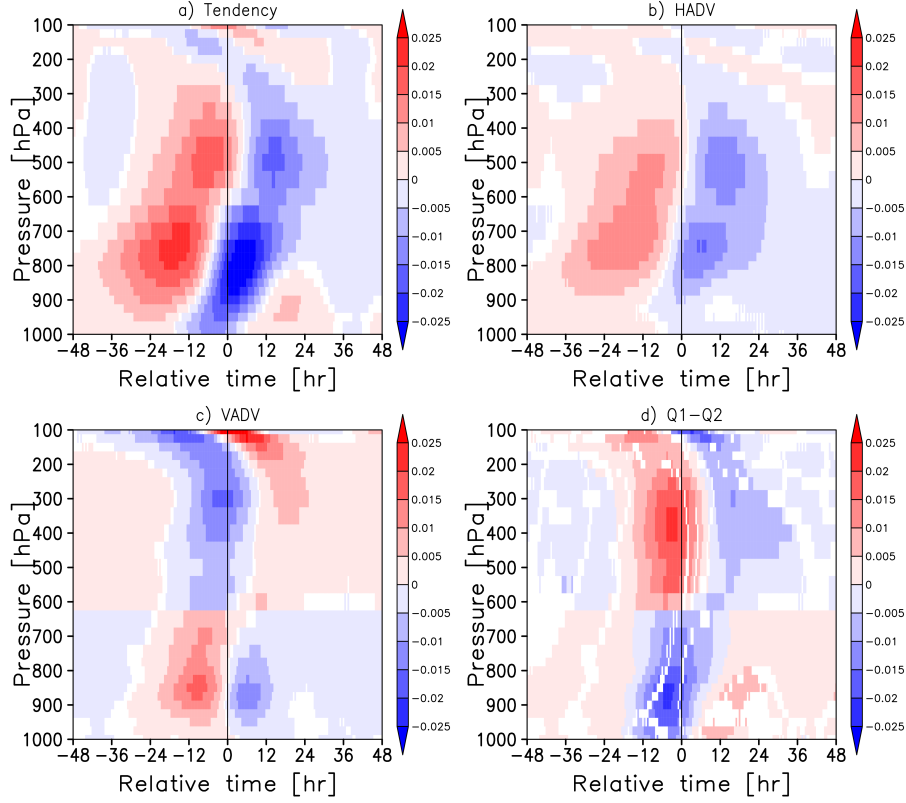
### 3.3.2 Vertical structure of the budget terms

Figure 3.3 shows the time-pressure cross section of the budget terms in Eq. (3.2), where positive and negative anomalies correspond to MSE import and export, respectively. The tendency term has a vertically tilted structure with a maximum amplitude around 750 hPa before deep convection, which is consistent with a large variation in MSE in the lower troposphere (not shown here). HADV is nearly in phase with the tendency term at each pressure level and mainly explained by zonal component. Meridional component is negligibly small as expected from Fig. 3.2b (not shown here). The amplitude of VADV is large during the evolution of intense convection ( $\pm 12$  hr), which is nearly comparable to that of HADV. Before WIG peak, a positive anomaly emerges in the lower troposphere under a negative anomaly from the middle to upper troposphere. This means that MSE increase (decrease) due to a strong ascent occurs in the lower (upper) half of the troposphere. After WIG peak, updraft is decreased in the upper troposphere and downdraft is strengthened in the lower troposphere due to an enhancement of anvil cloud. Therefore, a decrease of ascent in the upper troposphere weakens the negative VADV (positive anomaly) and an increase of descent in the lower troposphere enhances the negative VADV (negative anomaly). See section 6.7 for the relationship between a large-scale vertical motion and signs of VADV.

MSE eddy term in Eq. (3.2) is rewritten as follows:

$$Q_1 - Q_2 = Q_R + \partial_p(s'\omega') + \partial_p(Lq'\omega') \quad (3.6)$$

where  $Q_1$  is the apparent heating source and  $Q_2$  is moisture sink. MSE eddy transport  $-\partial_p(s'\omega') - \partial_p(Lq'\omega')$  is unresolved in a spatial resolution of reanalysis data. The vertical profile of  $Q_R$  is not provided in ERA-interim data. Hence, MSE eddy term ( $Q_1 - Q_2$ ) is calculated by subtracting the total advection term from the tendency term (Yanai et al. 1973). In Fig. 3.3, the eddy term is out of phase with VADV and shows a prominent contribution to the budget, which is absent by definition in the column integrated terms. The large amplitude may be attributed to the MSE eddy transport term rather than the radiative heating term since the former usually exceeds the latter in the region where deep vertical motion exists (Yanai et al. 1973). In fact, Masunaga and L'Ecuyer (2014) estimated the MSE eddy transport and radiative heating from satellite data, showing that the former is much larger than the latter during tropical convection with the time scale of about 1~2 days.



**Fig. 3.3:** Longitude-pressure cross sections of anomalies of the MSE budget terms ( $\text{m}^2 \text{s}^{-3}$ ). (a) MSE tendency, (b) horizontal MSE advection, (c) vertical MSE advection, and (d)  $Q1 - Q2$ . Anomalies are computed by subtracting the time mean value during  $\pm 48$  hour in the composite time series from the values at each pressure level. Shades represent significant regions at the 95 % level.

### 3.3.3 Decomposition of advection terms

The advection terms are further separated by decomposing variables into a time mean and perturbation from the mean. The background is defined as the 10-yr-averaged 6-hourly climatology of ERA-Interim data, a 365-day long time series of global maps. The zonal advection is separated into the four components:

$$-u\partial_x m = -u'\partial_x \bar{m} - u'\partial_x m' - \bar{u}\partial_x m' - \bar{u}\partial_x \bar{m} \quad (3.7)$$

where the variable  $A$  is expressed as  $A = \bar{A} + A'$ , and the overbar and the prime denote the background and perturbation, respectively. The meridional and vertical advection terms are decomposed in the same way. Following results are insensitive to the different definition of the background.

Figure 3.4 shows the composite time series of the decomposed advection terms. The background components ( $-\bar{u}\partial_x \bar{m}$ ,  $-\bar{v}\partial_y \bar{m}$ , and  $-\bar{\omega}\partial_p \bar{m}$ ) contribute to a small and steady MSE export. Advection by the mean wind across the perturbation MSE gradient  $-\bar{u}\partial_x m'$  gives a large contribution to the zonal advection, while  $-\bar{v}\partial_y m'$  and  $-\bar{\omega}\partial_p m'$  are nearly 0. The leading term of the meridional advection is  $-v'\partial_y m'$ . The contributions from  $-u'\partial_x m'$  and  $-\omega'\partial_x m'$  are non-negligible but small, indicating that the perturbation winds weakly act against  $m'$ . Vertical advection is mainly dominated by the advection by  $\omega'$

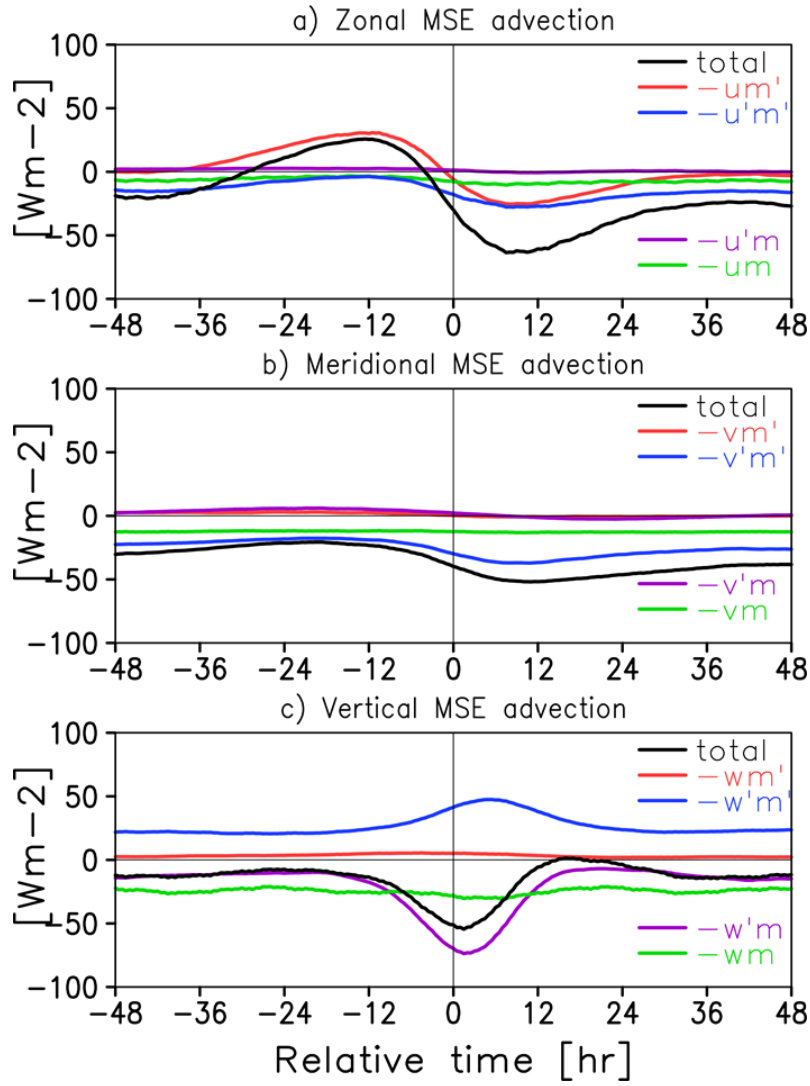


**Fig. 3.4:** Same as Fig. 3.2a, but for the MSE advection separated by the background and perturbation fields. (top) zonal, (middle) meridional, and (bottom) vertical MSE advection. The colored lines correspond to the labeled components in the figure.

across the mean MSE gradient  $-\omega' \partial_p \bar{m}$ . This is consistent with the previous studies suggesting that the large-scale vertical motion associated with the wave dynamics is responsible for the variability in the vertical advection.

Figure 3.5 shows snapshots of the longitude-time cross section of zonal wind and MSE zonal gradient which are decomposed into the mean and perturbation components. Each snapshot represents individual developing stages in WIG waves: an early stage of convection (-24 h), maximum of the MSE tendency (-15 h), near-precipitation maximum (-5 h), minimum of the MSE tendency (+5 h), and a decaying stage of convection (+10 h). The term  $\partial_x \bar{m}$  is positive (negative) to the west (east) of the composite center. This may result from a fact that a convective peak of WIG wave is most frequently observed in the pacific warm pool region where the mean MSE has a maximum in zonal direction. Amplitude of  $\partial_x m'$  is larger than that of  $\partial_x \bar{m}$ . The  $\bar{u}$  is easterly everywhere from the surface to the tropopause and slower than the propagation speed of WIG wave ( $\sim 17$  m/s). Amplitude of  $u'$  is large near the tropopause, which is a well-known feature of

WIG waves. Figure 3.6 shows the longitude-pressure cross sections of decomposed zonal advection components. As expected from Fig. 3.5, the contribution from  $-\bar{u}\partial_x m'$  is more prominent than the other components. A dipole-like structure of  $-\bar{u}\partial_x m'$  with positive and negative anomalies is explained by a superposition of  $\partial_x m'$  and  $\bar{u}$  shown in Fig. 3.5.

The positive advection due to  $-\bar{u}\partial_x m'$  leads to MSE increase (recharge) to the west of the region with a positive MSE anomaly ( $m'$ ). The MSE recharge to the west of convection might be important to determine the propagating direction of 2-day waves. It has been known that most of the observed 2-day waves prefer to propagate westward rather than eastward. It is also shown that spectral signal of convectively coupled eastward inertia gravity waves is less prominent than the WIG waves. However, it is unreliable that the term  $-\bar{u}\partial_x m'$  is responsible for the propagation of WIG waves. We discuss the role of the zonal advection more carefully in the next section.

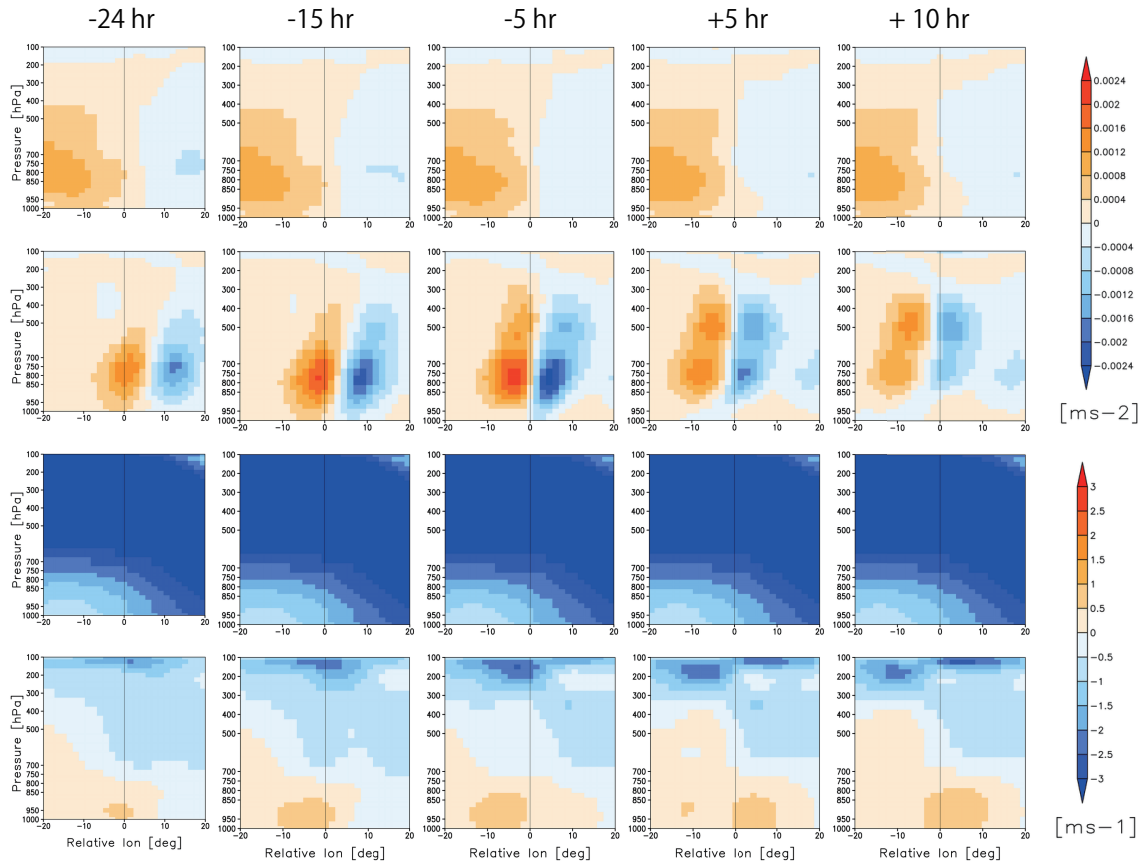


**Fig. 3.5:** Snapshots of the longitude-pressure cross section of MSE zonal gradient ( $\text{m s}^{-2}$ ) and zonal wind ( $\text{m s}^{-1}$ ). From the above line,  $\partial_x \bar{m}$ ,  $\partial_x m'$ ,  $\bar{u}$ , and  $u'$ . The horizontal and vertical axis represent relative longitude and pressure, respectively. Time increase to the right ( $-24, -15, -5, +5, +10$  hr).

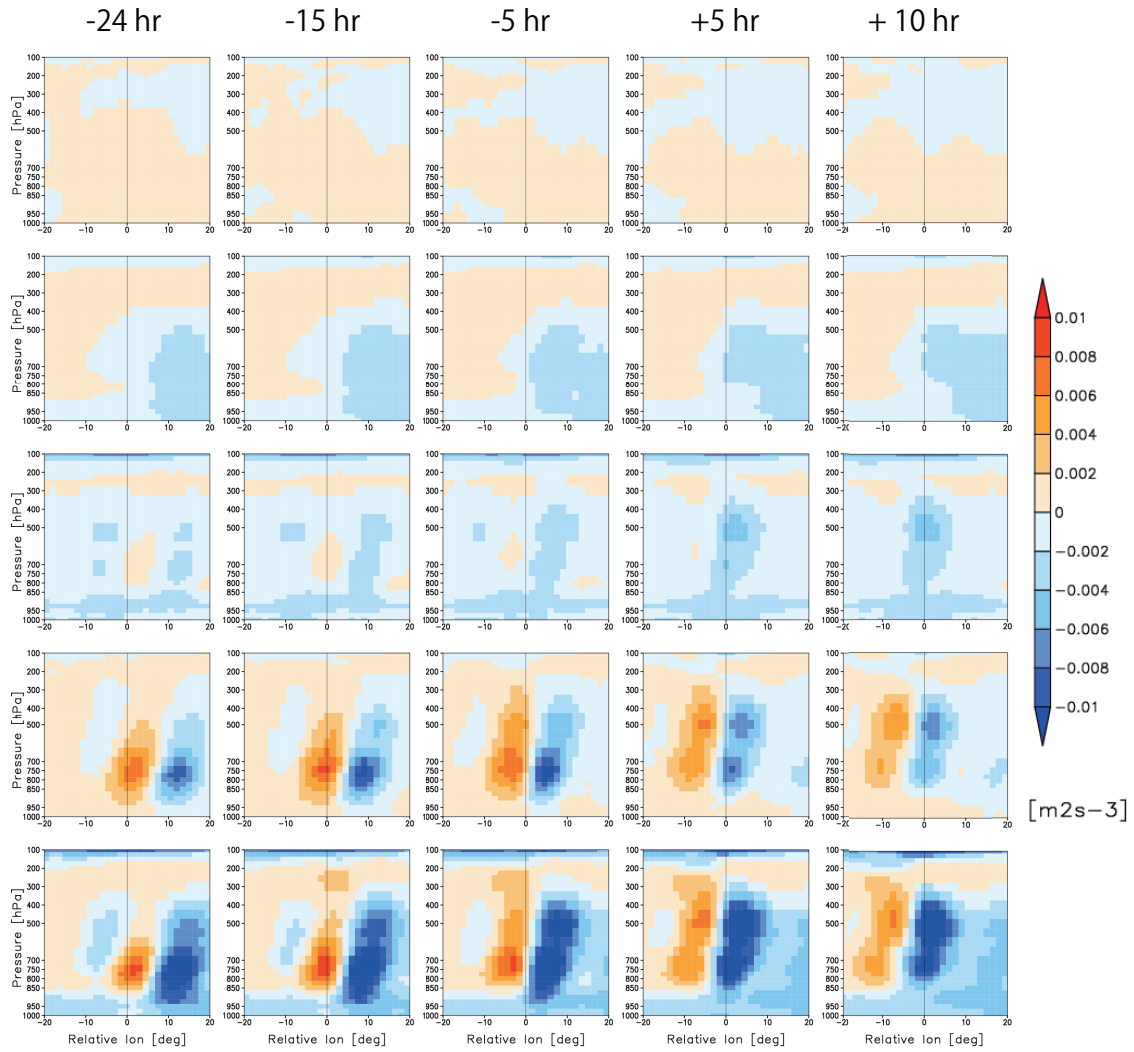


**Fig. 3.6:** Same as Fig. 3.5, but for the four components of zonal MSE advection decomposed by the background and perturbation fields. From above,  $-u'\partial_x \bar{m}$ ,  $-\bar{u}\partial_x \bar{m}$ ,  $-u'\partial_x m'$ ,  $-\bar{u}\partial_x m'$ , and  $-u\partial_x m$  ( $\text{m}^2 \text{s}^{-3}$ ).

### 3.3.4 Zonal wind effect

To examine the possible roles of the background zonal wind on the MSE budget, a barotropic flow  $\bar{u}_b$  is defined as a pressure averaged  $\bar{u}$  in the lower troposphere, where the tendency and advection terms show striking variabilities (Fig. 3.3).  $\bar{u}_b$  is expressed as

$$\bar{u}_b = \frac{1}{\Delta p} \int_{p_A}^{p_B} \bar{u} dp \quad (3.8)$$

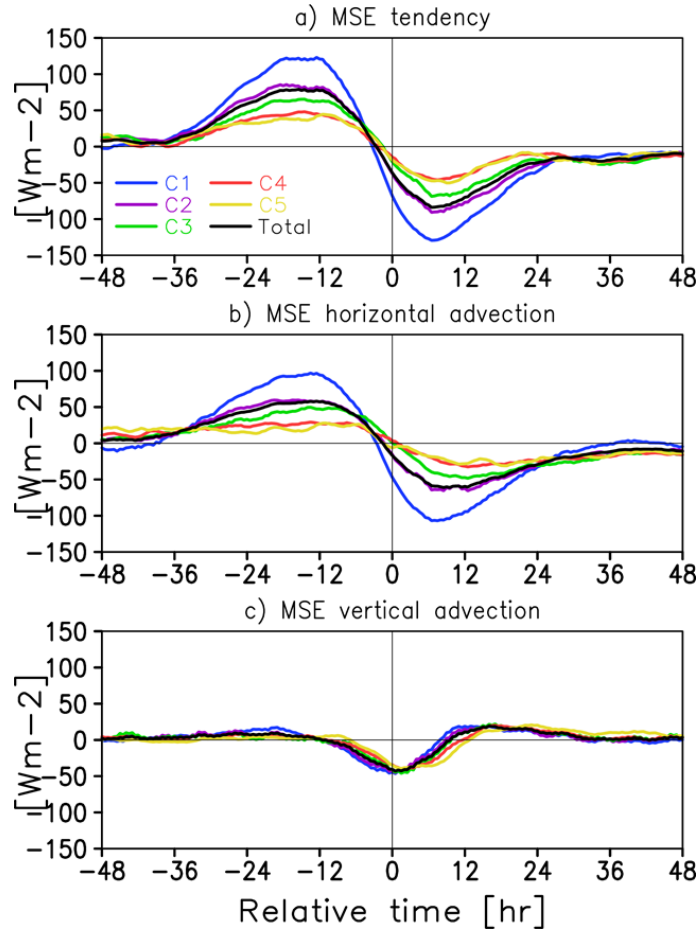
where  $p_A = 800$  hPa,  $p_B = 700$  hPa, and  $\Delta p = p_A - p_B$ . Then, the base points of composite (WIG peaks) are sorted into five categories by the barotropic flow at the points as summarized in Table 3.1. The base point in the category with the lower (higher) number corresponds to the stronger easterly (westerly) flow. Each of C1-C4 includes about 20 %-25 % and C5 includes about 8 %.

Figure 3.7 shows the composite time series of the anomalous tendency and advection terms for the different barotropic flow. The anomaly is the deviation from the temporal mean over  $\pm 48$  hr during the composite time series. Whenever the background barotropic flow is easterly (C1-C3) or westerly (C4-C5), the tendency and HADV are in phase with each other. As the barotropic easterly flow becomes stronger, their amplitudes become larger due to  $-\bar{u}\partial_x m'$ . In the easterly flow,  $-\bar{u}\partial_x m'$  and  $-u'\partial_x m'$  are in phase with each other (see Fig. 3.4), leading to a large amplitude of HADV (e.g, C1 in Fig. 3.7). Although  $-u'\partial_x m'$  is identical to that in the easterly flow, it is out of phase with  $-\bar{u}\partial_x m'$  in the westerly flow (not shown), canceling each other out in HADV (e.g, C5 in Fig. 3.7). On the other hand, VADV is insensitive to the direction and magnitude of the background wind speed. This implies that MSE recharge-discharge process of the wave dynamics is mainly dominated by the vertical advection due to the large-scale vertical motion.

The coherence of  $-\bar{u}\partial_x m'$  with the MSE tendency implies that this term is largely left unconsumed during a passage of the WIG wave and thus is not critical of two-day wave dynamics. As  $\bar{u}$  is slower than the wave propagation speed of about  $17 \text{ m s}^{-1}$ , the term  $-\bar{u}\partial_x m'$  brings an MSE anomaly from the near-side of the WIG peak itself. Under the easterly background, this results in a positive MSE advection because the near-side lies ahead of the convective peak where the lower troposphere is moist. When the background is westerly, in contrast, the horizontal MSE advection feels a dry anomaly behind the wave peak and counteracts the moistening due to the wave itself, which is primarily regulated by the vertical advection.

**Table 3.1:** Category of barotropic flow between 700 and 800 hPa.

<i>category</i>	$\bar{u}_b$ [m/s]	<i>percentile</i>
C1	$\sim -5.7$	$\sim 26$
C2	$-5.4 \sim -3.0$	$26 \sim 52$
C3	$-2.7 \sim 0.0$	$52 \sim 72$
C4	$0.3 \sim 3.9$	$72 \sim 92$
C5	$4.2 \sim$	$92 \sim 100$



**Fig. 3.7:** Same as Fig. 3.5, but for (a) the tendency, (b) horizontal MSE advection, and (c) vertical MSE advection. The WIG peaks are categorized by the background barotropic flow between 700 and 800 hPa (see Table. 1). C1 (blue), C2 (purple), and C3 (green) represent easterly, and C4 (red) and C5 (yellow) represent westerly.

### 3.3.5 Gross moist stability

As described above, it is shown that MSE recharge-discharge process in WIG waves is dominated by the vertical advection associated with the large-scale circulation. Here, Gross Moist Stability (GMS) is adopted to investigate the relationship between moist convection and the large-scale wave dynamics. Neelin and Held (1987) first introduced GMS as a tool to simplify the relationship between moist convection and large atmospheric circulations. In their two dimensional model, GMS was a time invariant parameter and was meaningful only when GMS is positive because otherwise the system would be unstable and time dependent.

Recently, GMS has been tested in much broader contexts including the so-called normalized GMS (NGMS) (Raymond and Fuchs 2007; Raymond et al. 2009; Sessions et al. 2010; Kuang 2011; Hannah and Maloney 2011; Andersen and Kuang 2012; Benedict et al. 2014; Sobel et al. 2014). For example, Raymond et al. (2009) defined NGMS as “the ratio of net lateral outflow of MSE from an atmospheric column to some measure of

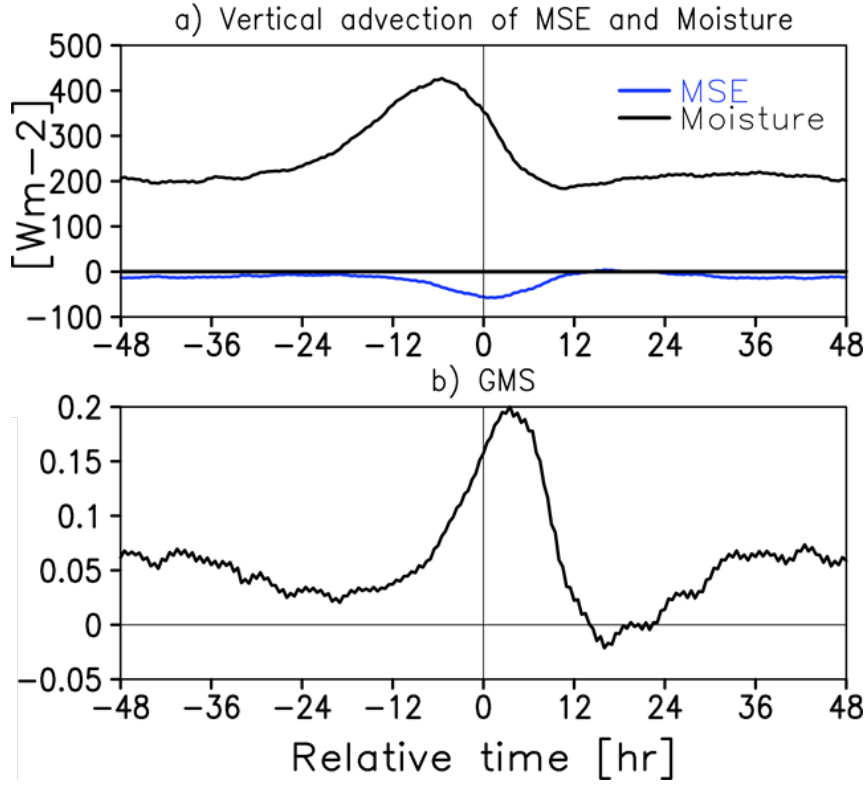


**Fig. 3.8:** Same as in Fig. 3.2a, but for (a) vertical MSE advection (blue) and vertical moisture advection (black), (b) normalized GMS.

convective intensity within the column”. The sign and magnitude of NGMS are a measure to characterize how convective heating and large-scale dynamics work together. Utilizing the definition of NGMS in Raymond et al. (2009), we examine the roles of convection in the large-scale dynamics associated with WIG waves. NGMS is defined as

$$NGMS = -\frac{\left\langle \omega \frac{\partial m}{\partial p} \right\rangle}{\left\langle \omega \frac{\partial Lq}{\partial p} \right\rangle} \quad (3.9)$$

where the denominator and numerator are the column integrated vertical advection of moisture and MSE, respectively. The numerator, unlike Raymond et al. (2009), only includes VADV, since a large amplitude of HADV due to the advection  $\langle -\bar{u} \partial m' / \partial x \rangle$  is not responsible for the recharge-discharge process.

Figure 3.8a shows the composite time series of the denominator and numerator in Eq. (3.9). Since the numerator sometimes approaches the noise level close to zero, the noise is smoothed out by applying a  $\pm 6$ h moving average. The following result is insensitive to the smoothing. The moisture import due to the vertical advection increases before deep convection and peaks around precipitation maximum of WIG wave. The recharge of MSE (decrease in VDAV) occurs during and after the deep convection.

NGMS in Fig. 3.8b is estimated from the advection terms in Fig. 3.8a. It decreases gradually before deep convection and approaches 0 around -20 h when VADV is nearly 0.

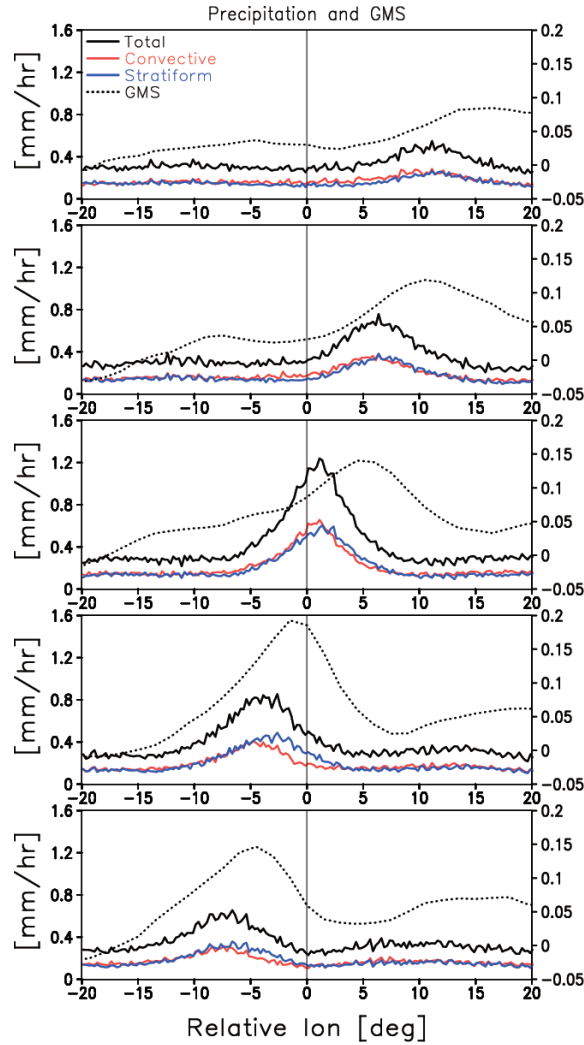


**Fig. 3.9:** The snapshots of zonal distribution of precipitation and GMS. Solid lines represent total (black), convective (red), and stratiform (blue) rainfall rate. Dotted line represents normalized GMS. The horizontal axis is the relative longitude between  $-20^\circ$  and  $+20^\circ$ . The time increases from top to bottom ( $-24$ ,  $-15$ ,  $-5$ ,  $+5$ ,  $+10$  hr).

Then, it increases during and after the deep convection, and arrives its maximum 0.2 after the WIG peak around +6 h. The time evolution of NGMS during active phase of WIG wave is nearly consistent with that of meso-scale tropical convections with a time scale of about 1-2 days (see Fig. 3 in Masunaga and L'Ecuyer 2014). Masunaga and L'Ecuyer (2014) calculated the similar composite time series of NGMS from satellite observations of tropical convection, varying with time on an hourly to daily time scale for the horizontal scale of about 100 km. Although their analysis was not targeted on any particular wave mode, NGMS decreases toward 0 before deep convection and increases following convection development, closely resembling Fig. 3.8b. Moisture and MSE convergence are largely controlled by vertical advection in Masunaga and L'Ecuyer (2014). The large contribution of VADV might be because the horizontal scale of the convection in their analysis is much smaller than that in the composite WIG waves (Fig. 3.1). Also, it is

possible that the contribution of the second baroclinic mode is underestimated in ERAI data. In section 3.4, we will discuss again why the contribution of the second mode is smaller in this study than in previous studies (Haertel et al. 2008; Inoue and Back 2015a).

Figure 3.9 shows the zonal distribution of precipitation and NGMS. The area of active precipitation with the zonal scale of about 1000 km moves westwards as expected from Fig. 3.1. Convective rainfall peaks a few hours earlier than stratiform rainfall in  $\pm 5$  hours, which is a well-known property of tropospheric mesoscale convective systems (e.g., Houze 2004). NGMS has a significantly high value to the east of the precipitation peak. NGMS has a lower value to the west of the peak, in which VADV closes to 0. This might suggest that an area favorable (unfavorable) for the development of convection emerges to the west (east) of the convective envelope.

## 3.4 Discussion

### 3.4.1 Comparison with the other CCEWs and MJO

In convectively coupled gravity waves, HADV is known to be less important than VADV to controlling a MSE recharge-discharge process. Peters and Bretherton (2006), based on Cloud Resolving Model, showed that VADV is dominant over HADV in the Kelvin wave. Haertel et al. (2008) and Inoue and Back (2015a) showed that a column MSE is mainly controlled by VADV in COARE 2-day waves (WIG waves). The results in this chapter also supports the previous studies, indicating that VADV plays a primary role in maintaining the thermodynamic process. However, HADV in Fig. 3.2b is larger than that in COARE 2-day wave (Inoue and Back 2015a). This discrepancy could be explained by the difference of the background zonal wind. In the present study,  $-\bar{u}\partial_x m'$  and  $-u'\partial_x m'$  are in phase due to background easterly wind (see Fig. 3.4), leading to an emphasize of HADV. Meanwhile, the background zonal wind is strong westerly in the lower troposphere during TOGA COARE IOP (e.g., Chen et al. 1996; Ciesielski et al. 1997). HADV in COARE 2-day wave could be weakened because  $-\bar{u}\partial_x m'$  and  $-u'\partial_x m'$  are in opposite phase under the background westerly.

In MJO, both VADV and HADV are responsible for the MSE recharge-discharge process. HADV could play an important role in the eastward propagation mechanism of the MJO (Maloney 2009; Maloney et al. 2010; Kiranmayi and Maloney 2011; Benedict et al. 2014; Kim et al. 2014; Sobel et al. 2014). As noted in the previous paragraph, an importance of HADV is small in the WIG wave and Kelvin wave. This corresponds to the result in Inoue and Back (2015a) showing that a relative contribution of HADV increases as the time scale of the disturbance grows to intraseasonal scales. There are some differences in the thermodynamic process of the MJO compared to the WIG wave. First, MSE source terms have the same amplitude as the MSE advection and play an important role in regulating a column MSE. Also, radiative and surface fluxes fluctuate larger as the time scale of the disturbance get longer (e.g., Inoue and Back 2015a). Second, the meridional advection has a striking variability during the MJO propagation. Third, the perturbation wind ( $u'$  and  $v'$ ), associated with the wave kinetics, causes equal or larger MSE advection than the background wind ( $\bar{u}$  and  $\bar{v}$ ). Meanwhile, eddy MSE advection ( $-u'\partial_x m'$  and  $-v'\partial_y m'$ ) stay small in WIG waves. This difference may be because the variation of environmental fields change with the spatio-temporal scale of CCEWs (Kiladis et al. 2009).

For example, the amplitude of  $u'$  in WIG is about ten percent of that in MJO (Benedict and Randall 2007; Haertel et al. 2008; Kiladis et al. 2009).

### 3.4.2 Comparison with 2 mode model

Previous studies suggest that MSE recharge-discharge processes in CCEWs are well captured by the multi-mode model (e.g., Peters and Bretherton 2006; Haertel et al. 2008). The shallow vertical motion with the second baroclinic mode causes a positive VADV preceding deep convection (MSE recharge process). The strong vertical motion associated with the first baroclinic mode causes a negative VADV (MSE discharge process). After the convective peak, the descending motion in the lower troposphere and the ascending motion in the upper troposphere with the second mode cause a negative VADV (MSE discharge process).

In this study, a negative VADV around a WIG peak might be explained by the first mode (Fig. 3.2b). A positive VADV with the second mode is not visually evident, although a slight vertical tilt provides a hint of the second mode (Fig. 3.3). It is implied that the framework of multi-mode model could be applied to the composite WIG waves. This is qualitatively consistent with the previous studies which emphasized the multi-mode structure in the 2-day wave dynamics (Haertel and Kiladis 2004; Haertel et al. 2008; Kuang 2008b; Tulich and Kiladis 2012; Yasunaga and Mapes 2012; Yasunaga and Mapes 2014) (see section 3.4.3).

The lack of a clear signature of shallow moistening by the congestus mode might be a unique feature of WIG waves, or possibly due to the technical limitation in reproducing shallow updraft in reanalysis data. It could be difficult for reanalysis data to resolve a rapid variation associated with shallow circulation due to the coarse resolution. Despite of an obscure contribution of the second mode, this study hardly deny a primary importance of the second baroclinic mode in the wave dynamics. It would be beneficial elsewhere to test carefully to what extent a pre-moistening of the second mode is important in the WIG wave dynamics in comparison with the vertical mode decomposition technique used in recent investigations (Handlos and Back 2014; Masunaga and L'Ecuyer 2014).

### 3.4.3 Propagation characteristics of 2-day waves

Previous studies based on ground and satellite measurements showed that most of the convective systems accompanied with 2-day waves move westward (Takayabu 1994b; Takayabu et al. 1996; Chen and Houze 1997; Haertel and Johnson 1998; Haertel and Kiladis 2004). It is outside the scope of this study to explore the origins of westward propagation because the 2-day wave is currently extracted by a WIG filter and by design moves westward. Nevertheless, a brief discussion on the selection of propagation direction in the general context might be beneficial.

Here, the propagation dynamics is examined in terms of thermodynamic process. As the low (high) NGMS area exists to the west (east) of pre-existing convection, new convection prefers to arise to the west of the pre-existing convection. Hence, a synoptic-scale convective system accompanied with the WIG wave could move westward. This dynamics mainly depend on the generic properties of inertio-gravity waves, and the same dynamics with opposite signs would presumably help convection move eastward when

coupled with the eastward inertia gravity (EIG) waves.

As shown in section 3.3.4, the present analysis presents no clear evidence that the background state plays roles in breaking the east-west symmetry in the propagation direction and phase speed of 2-day waves. Meanwhile, a further analysis is needed to discuss the relationship between the wave propagation dynamics and the background wind (Stechmann and Majda 2009; Tulich and Kiladis 2012). For example, Tulich and Kiladis (2012) based on Weather Research and Forecast (WRF) model indicated that the zonal wind shear in the lower troposphere is important to westward propagation of 2-day wave. Key parameters responsible for the propagation characteristics of 2-day waves will be addressed to more depth in future.

It is expected that phase speed of CCEWs is affected by the moist process and various aspects in the tropical atmosphere (see section 1.2.3 and ). Previous studies have discussed in various aspect about the WIG phase speed which is slower than the theoretically expected one. In the vertical mode perspective, Haertel and Kiladis (2004) showed that the shallow equivalent depth could result from a superposition of the first and second baroclinic modes. Based on a cross spectral analysis, Yasunaga and Mapes (2012) and Yasunaga and Mapes (2014) showed that the fast and slow WIG waves have different moist process. Takayabu (1994b) reported Doppler shifting by the background zonal wind in WIG waves and showed that the equivalent depth is 20 m. Furthermore, Dias and Kiladis (2014) showed that the equivalent depth of CCEWs is uniform ( $\sim 25$  m) between the different climatological regions if the Doppler shifting is considered. It is still unclear, however, how the phase speed of the WIG wave is modified by the background zonal wind and the moist process. To approach the above problem, in chapter 4, we will calculate the baroclinic mode by using ERAI data and examine their modifications to the phase speed.

### 3.5 Summary

Following recent investigations indicating a prominent role of moistening in the troposphere on the coupling mechanism, the present study examines the thermodynamic process of quasi 2-day waves by using moist static energy. The budget equation of column MSE tells us MSE recharge-discharge process associated with the wave dynamics. The 2-day waves are detected by WIG filtering of brightness temperature (mergedIR). The budget terms calculated from the reanalysis data (ERA-Interim) are composited around the WIG peaks to create statistically continuous time series. The horizontal dynamic structure of composite WIG waves is confirmed to be overall as expected from previous studies.

MSE variability during active phase of WIG waves is mainly dominated by MSE advection term. Meanwhile, surface fluxes and radiative heating bring about nearly constant MSE import and export, respectively, and hardly contribute the MSE variability throughout the evolution. An enhancement of negative vertical advection decreases column MSE around WIG peak, plausibly resulting from deep convection (or the first baroclinic mode). Zonal MSE advection causes a significant MSE increase and a decrease before and after deep convection, respectively, overwhelming vertical advection in magnitude. The zonal advection is mainly dominated by  $-\bar{u}\partial_x m'$ , while the term should be considered separately to the MSE recharge-discharge process. It is implied that vertical advection rather than horizontal advection modulates the thermodynamic process in the WIG waves. This

result is qualitatively consistent with the previous studies suggesting that the recharge-discharge process in convectively coupled gravity waves (e.g., WIG waves and Kelvin waves) is regulated by a large-scale vertical circulation (Peters and Bretherton 2006; Haertel et al. 2008; Inoue and Back 2015a). A slight contribution of the second baroclinic mode in this study might result from the technical limitation in reproducing shallow updraft in reanalysis data.

NGMS is used to examine the relationship between the large-scale circulation of the waves and convective intensity. Before deep convection, NGMS gradually decreases from a positive value to a significant small positive value near 0. According to the development of deep convection, NGMS increases and reaches its maximum after the WIG peak. It is suggested that the low (high) NGMS leads to (lags) deep convection. In the convective envelope associated with WIG waves, new convection is allowed to develop to the west of the pre-existing convection where NGMS decreases toward zero. These results are nearly consistent with previous studies showing that the temporal variability of NGMS is prominent for the disturbances with a time scale of about 2-days (Masunaga and L'Ecuyer 2014; Inoue and Back 2015a).

The results obtained in this chapter are nearly consistent with the previous investigations based on multi-mode theory, although the second baroclinic mode is invisible in this analysis. Ongoing work is testing carefully to what extent a pre-moistening of the second mode works in the WIG wave dynamics. In the next chapter, the coupling mechanism of 2-day waves is examined in the light of vertical modes.

# Chapter 4

## Vertical mode and effective stability of quasi-2-day wave

### 4.1 Goal of this chapter

As shown in chapter 3, a large-scale vertical motion plays an important role in modulating the thermodynamic properties of the composite WIG waves. It is known that the large-scale dynamical fields of the wave are separated into a few vertical modes with different vertical wave length. The vertically tilted and top-heavy structure is explained by a superposition of a few vertical modes, which is qualitatively consistent with the wave dynamics produced by multi-mode models.

Vertical modes associated with the wave dynamics would be slowed down when coupled with convection. In the multi-mode models, the phase speed of different vertical modes is not likely to significantly disagree among them since otherwise the wave would necessarily be heavily dispersive and would not propagate over a long distance. However, it remains unclear as to how different vertical modes can have a common phase speed constituting a coherent wave packet without being immediately dispersed out. It is not obvious whether the dispersiveness of the wave is small, because propagation dynamics of CCEWs (e.g., phase speed and propagating direction) would be modulated by various factors in the tropical atmosphere. Previous studies have suggested that the wave propagation would be affected by environmental fields (e.g., mean wind) as well as moist convective processes (Wheeler et al. 2000; Straub and Kiladis 2002; Yang et al. 2003 2007a; Roundy 2008; Dias and Pauluis 2009; Kiladis et al. 2009; Stechmann and Majda 2009; Dias and Pauluis 2011; Dias and Kiladis 2014; Yasunaga and Mapes 2014). Although the dispersiveness of the waves has yet to be discussed deeply in the above studies, it may be also related to the propagation dynamics of the waves. To better understand this relationship, we need to examine what determines a degree of slowdown of the vertical modes. Majda and Shefter (2001) showed using two mode model that the relative contribution of the second mode to the first mode is larger in the slower wave, implying that the second mode is important to regulate the slowdown of the modes as predicted by stratiform instability mechanism. Yasunaga and Mapes (2014) also indicates that the ratio of stratiform precipitation to convective precipitation is large in the slower wave. More observational evidence is required to examine the mechanism of slowdown of vertical modes.

In this chapter, the slowdown mechanism of 2-day waves is explored by using vertical

mode decomposition technique. The ultimate goal is to provide a theoretical framework to explain the slowness of CCEWs in light of both the effective stability and multiple vertical modes.

## 4.2 Phase speed of composite WIG wave

In chapter 4, WIG waves with different phase speed are detected from five sub-filters with different equivalent depth (see section 2.2.2 for filter definition). The phase speed of composite WIG waves is calculated by the radon transform of anomalous TBB (see section 2.2.5 for details). Figure 4.1a shows the longitude-time diagram of anomalous TBB composited around the WIG peaks identified by the h25/15 filter. A convectively active area with a negative anomaly is shown to propagate westward over a period of about 2 days. By using the RT method, the anomalies are projected onto a line at angle  $\theta$  from  $0^\circ$  to  $180^\circ$ . Figure 4.1b shows that variance of the transformed TBB is normalized by its maximum value at  $\theta = 59^\circ$ , indicating that the wave propagate at a direction of  $\theta + 90^\circ = 149^\circ$ . The slope of the black line in Fig. 4.1a is estimated to be the phase speed of  $21 \text{ m s}^{-1}$ .

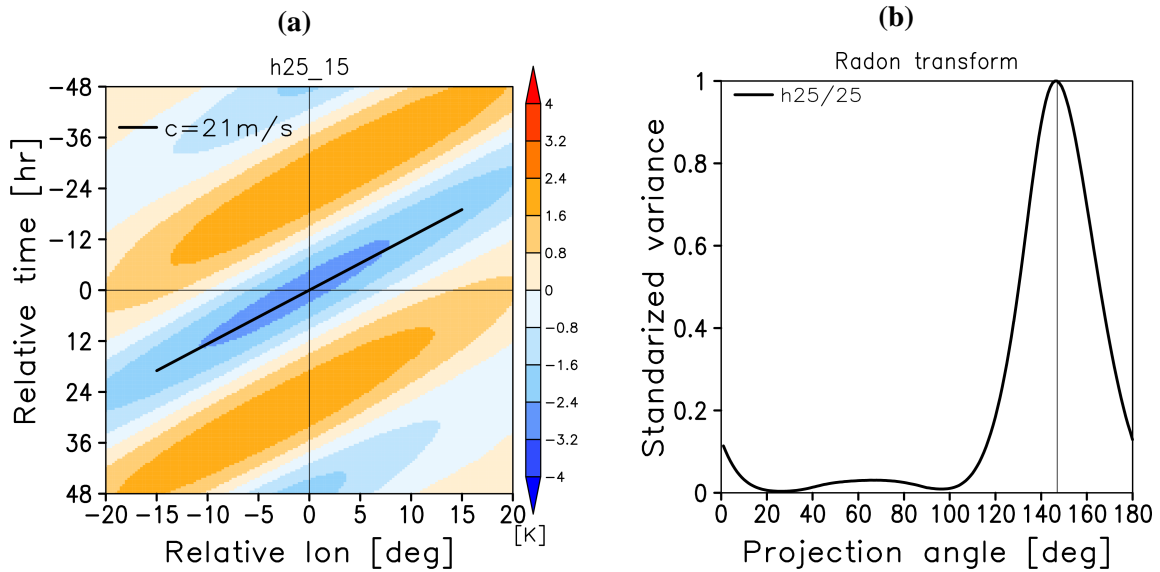


**Fig. 4.1:** (a) A longitude-time diagram of anomalous TBB [k] for WIG wave identified with filter h25/15. A slope of black line represents the phase speed of about 21 m/s. (b) Standardize variance of transformed TBB in Fig. 4.1a with respect to the projection angle  $\theta + 90^\circ$ . The curve is maximized at  $149^\circ$  (black thin line).

For the waves identified using different WIG filters, the phase speeds are calculated by applying the RT method to both the anomalous TBB and precipitation (Fig. 4.2). The phase speed of TBB (black circle) agrees well with that of precipitation (blue circle).

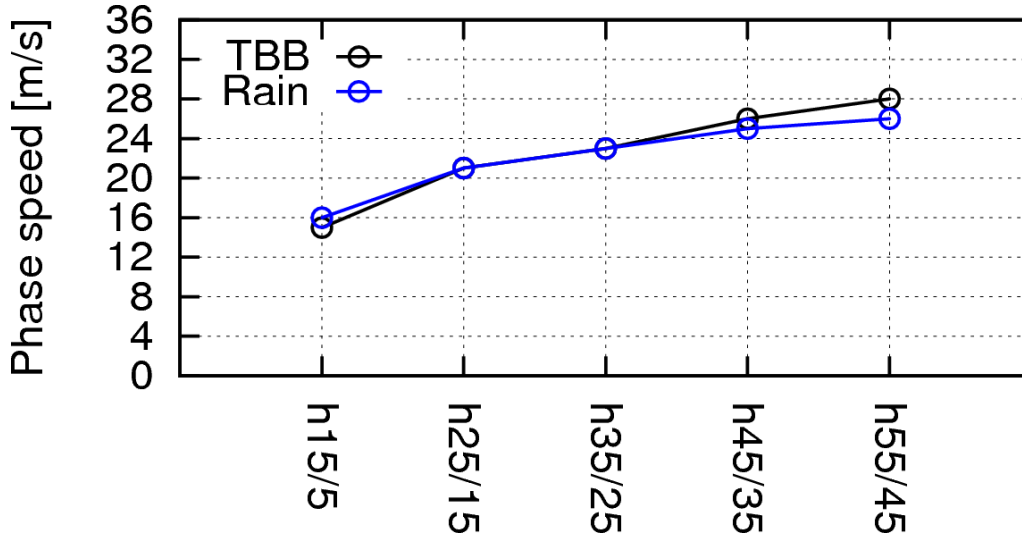


**Fig. 4.2:** Phase speed of composite WIG wave. Black and blue circle represents the phase speed estimated by RT of anomalous TBB and anomalous precipitation, respectively.

Therefore, it is suggested that the estimated phase speeds are insensitive to the difference in physical parameters (cloud or precipitation) or in observational sampling approaches (mergedIR or TRMM PR). The range of phase speeds ( $15\text{--}28\text{ m s}^{-1}$ ) is consistent with that found in previous studies ( $10\text{--}30\text{ m s}^{-1}$ ). A WIG filter with a deeper (shallower) equivalent depth results in a faster (slower) wave as expected, supporting the robustness of the RT method for use in the present application.

## 4.3 Vertical mode transform

### 4.3.1 Vertical mode transform

In this section, we analyze the vertical modes associated with the composite WIG wave. Figure 4.3 shows a time-pressure cross section of the mode transform component  $\omega_n$  for the first four baroclinic modes, where  $\omega_n$  is calculated by substituting  $h_n$  in the continuity equation (see Fig. 2.8b). A strong updraft, with a single-sign structure due to the first mode, develops around 0 h and reaches a maximum of around 500 hPa in the middle troposphere at  $-3$  h (Fig. 4.3a). The amplitude of the first mode is the largest among the first four modes. Although the higher modes have smaller amplitudes, their contribution to the wave dynamics is not negligible. The second and third modes are almost in phase with each other and exhibit a dipole-like structure with opposite signs in the lower and upper half of the troposphere (Fig. 4.3b,c). The second and third modes, with a peak around  $\sim +6$  h, is roughly quadrature with the first mode. The time lag between the modes is estimated to be about 10 h. The negative peak of the third mode in the lower troposphere represents a shallow updraft preceding deep convection. Such dipole-like structures lagging or preceding the first mode are consistent with the stratiform mode or the congestus mode, respectively. The fourth mode (Fig. 4.3d) is almost in phase with the first mode, which might provide a modest modulation to the first mode.

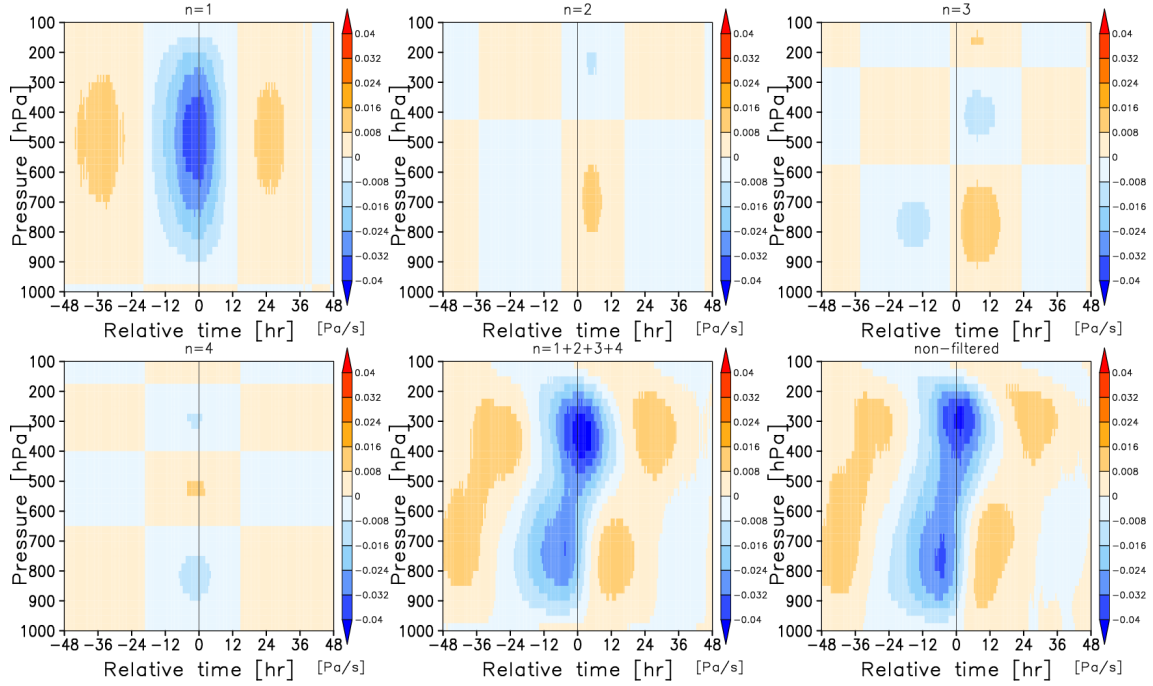


**Fig. 4.3:** A time-pressure cross section of pressure velocity [Pa/s] of composite WIG wave identified with filter h25/15: (a)  $\omega_1$ , (b)  $\omega_2$ , (c)  $\omega_3$ , (d)  $\omega_4$ , (e) a superposition of  $\omega_n$  from  $n = 1$  to  $n = 4$ , and (f) composite  $\omega$ . A negative and positive value denotes upward and downward motion, respectively.

The superposition of the first four vertical modes reproduces a vertically tilted and top-heavy structure (Fig. 4.3e), which is qualitatively consistent with the observed one (Fig. 4.3f). Although not shown here, it is confirmed that the first four modes are sufficient to capture the various dynamical fields ( $u$ ,  $v$ ,  $D$ ,  $\phi$ , and  $Q$ ). Additional higher modes are needed to reproduce a boomerang-like structure in the temperature field as reported in previous studies (Haertel and Kiladis 2004; Haertel et al. 2008; Kuang 2008a; Tulich and Kiladis 2012), which is outside the scope of the present work. It is also confirmed that the above results are true for both the slower and the faster waves (not shown here).

### 4.3.2 Phase speed of the vertical mode

Phase speeds of moist vertical modes are examined below. The mode transform component  $A_n$  is written as  $A_n = \hat{A}_n \Omega_n$ , where the mode transform coefficient  $\hat{A}_n(x, y, t)$  depends on both the horizontal location and time, and the structure function  $\Omega_n(p)$  depends only on pressure. Because the horizontal propagation of the moist mode is characterized by  $\hat{A}_n$ , the phase speed is calculated by RT of  $\hat{A}_n$ . Figure 4.4 shows that the  $\hat{u}_n = \langle u | h_n \rangle$  anomaly moves westward over a period of about 2 days in a longitude-time domain. Shades of red and blue represents westerly and easterly zonal wind anomaly at surface, respectively. The surface wind converges (diverges) for the first and fourth modes (the second and third modes) around WIG peak, which corresponds to the upward (downward) motion shown in Fig. 4.3.

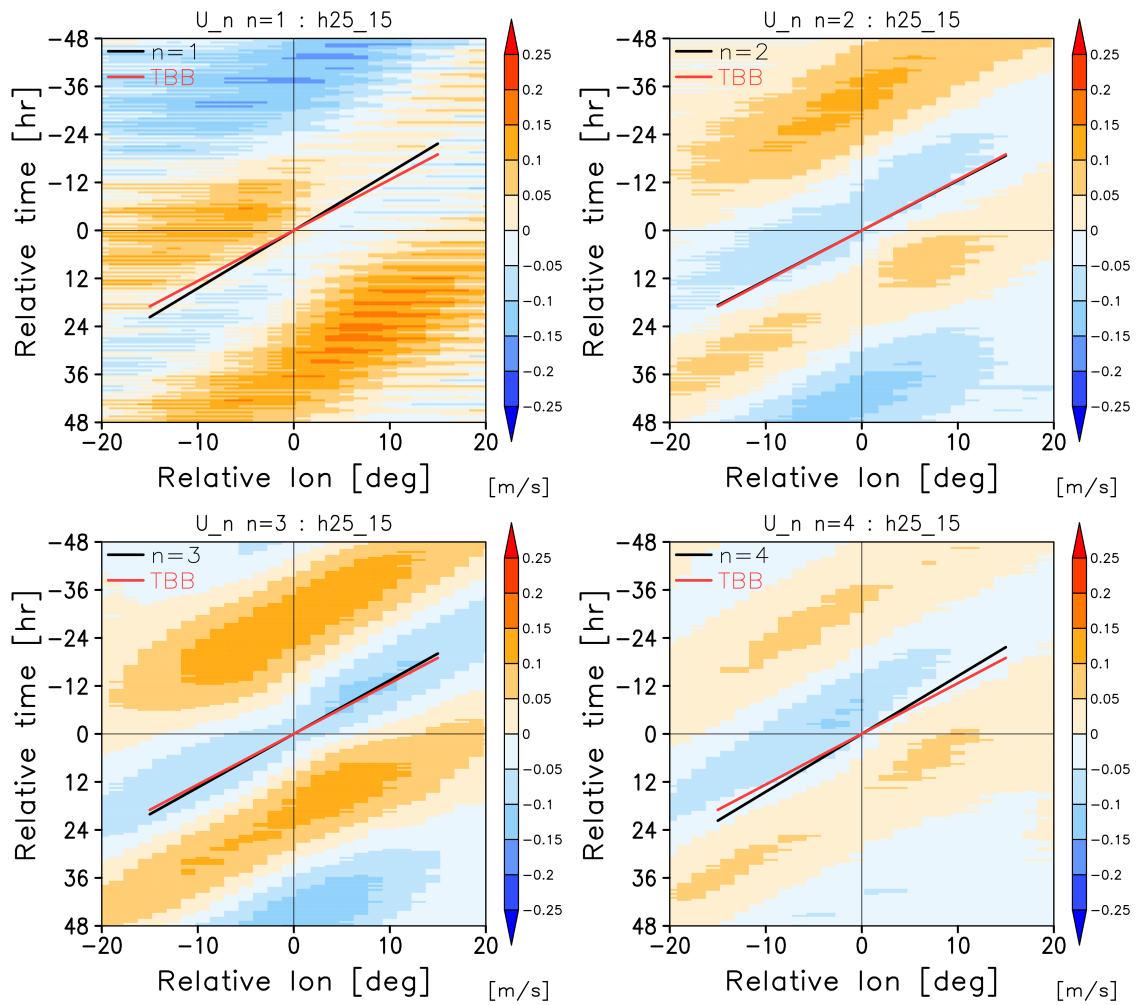


**Fig. 4.4:** A longitude-time diagram of mode transform coefficient of zonal wind  $\hat{u}_n$  for the first four vertical modes. A slope of black line corresponds to phase speed of vertical mode, which is estimated by RT of  $\hat{u}_n$ . Red line is the same as black line in Fig. 4.1a.

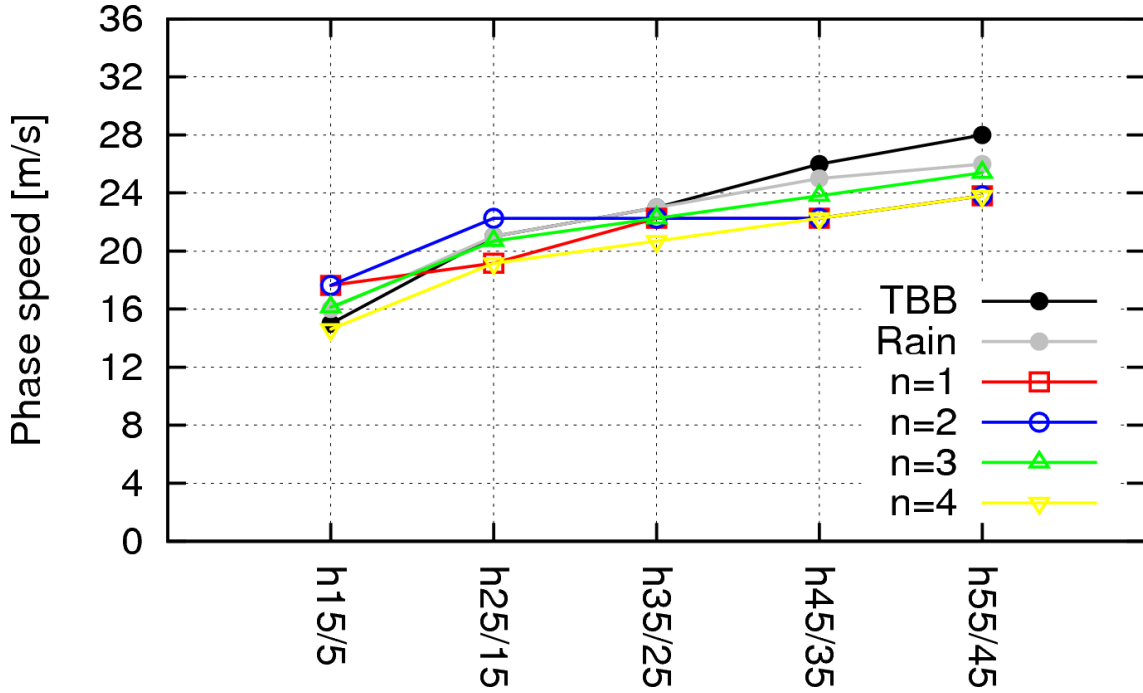


**Fig. 4.5:** Phase speed of moist vertical mode estimated by using  $\hat{u}_n$  in Fig. 4.4 for  $n = 1$  (red),  $n = 2$  (blue),  $n = 3$  (green), and  $n = 4$  (yellow). Phase speed estimated from TBB (Black) and precipitation (gray) are the same as that in Fig. 4.2.

Phase speed of the moist mode, calculated by RT of  $\hat{u}_n$ , corresponds to the slope of the black line in Fig. 4.4. The phase speed of  $\hat{u}_n$  is roughly equal to the phase speed of the wave (TBB and precipitation) and is faster for larger equivalent depths (Fig. 4.5). It is noted that  $u_n$  itself is not filtered but is simply composited against the filtered TBB peaks, so the agreement in the phase speed is not by design. The phase speed of the dry first mode is, in theory, a few times faster than that of the higher modes, whereas different moist modes have a similar phase speed among themselves. Such a non-dispersive nature of moist vertical modes holds for both the slower and faster waves. It is also emphasized that the above results are verified for other parameters, including geopotential, horizontal wind divergence, and heating rate (not shown here).

## 4.4 Effective static stability

### 4.4.1 Definition of $\alpha_n$

In section 4.3.2, it was shown that different moist vertical modes propagate at a similar phase speed, more slowly than the dry counterparts. To reveal the slowdown mechanism of each mode, we investigate the relationship between a reduced equivalent depth and a reduced static stability that the mode feels.

First, we consider the relationship between static stability ( $S$ ) and effective static sta-

bility ( $S_e$ ). For a fixed vertical mode, the thermodynamic equation is written as follows:

$$\partial_t T_n = S\omega_n + Q_n \quad (4.1)$$

Here  $S\omega_n$  represents adiabatic heating (cooling) due to ascent (descent), and  $Q_n$  represents the diabatic source, including latent and radiative heating terms. Assume that  $Q_n$  is expressed as

$$Q_n \sim -\alpha_n S\omega_n \quad (4.2)$$

where  $\alpha_n$  is a positive constant representing the degree of cancellation between adiabatic heating (cooling) and diabatic cooling (heating) (e.g., [Kiladis et al. 2009](#)). Substituting Eq. (4.2) in (4.1) yields:

$$\partial_t T_n \sim S_e \omega_n \quad (4.3)$$

where  $S_e$  is defined as

$$S_e = (1 - \alpha_n)S. \quad (4.4)$$

It is suggested that  $0 < \alpha_n < 1$  since  $S_e$  is considered to be positive.

Second, we consider the relationship between static stability and equivalent depth of the vertical mode. Here, the equivalent depths of the dry vertical mode and that of the moist vertical mode are denoted by  $H_n$  and  $H_e$ , respectively. In shallow water system with a constant Brant vaisalla frequency ( $N$ ),  $H_n$  is written as

$$H_n = \frac{N^2}{g \left( m_{z,n}^2 + \frac{1}{4h^2} \right)} \quad (4.5)$$

where  $g$  is the gravitational acceleration,  $h$  is the scale height, and  $m_{z,n}$  is the vertical wave number (e.g., [Wheeler et al. 2000](#)).  $H_n$  is a function of  $m_{z,n}$  and  $S$  ( $\propto N^2$ ). For a fixed vertical mode (constant  $m_{z,n}$ ),  $H_n$  is proportional to  $S$ . Assuming that shallow  $H_e$  of the moist mode is also proportional to reduced static stability ( $S_e$ ), we obtain

$$\frac{H_e}{H_n} \sim \frac{S_e}{S}. \quad (4.6)$$

From Eq. (4.6), it is indicated that the degree of reduction of equivalent depth is connected to that of static stability. It should be noted that  $H_n$  and  $H_e$  can not be exactly expressed in a simple form as shown in Eq. (4.5) since static stability depends on the height in the real atmosphere. This effect, however, is neglected here since the vertical variability in the stability stays small except near the surface and tropopause.

Combining Eqs. (4.6) and (4.4), the theoretical expectation of  $\alpha_n$  is derived as

$$\alpha_n \sim \tilde{\alpha}_n = 1 - \frac{H_e}{H_n} \quad (4.7)$$

where  $\tilde{\alpha}_n$  is a monotonical decrease function of  $H_e$  with an increment of  $-1/H_n$ . Eq. (4.7) is a useful tool to investigate the relationship between the shallow equivalent depth

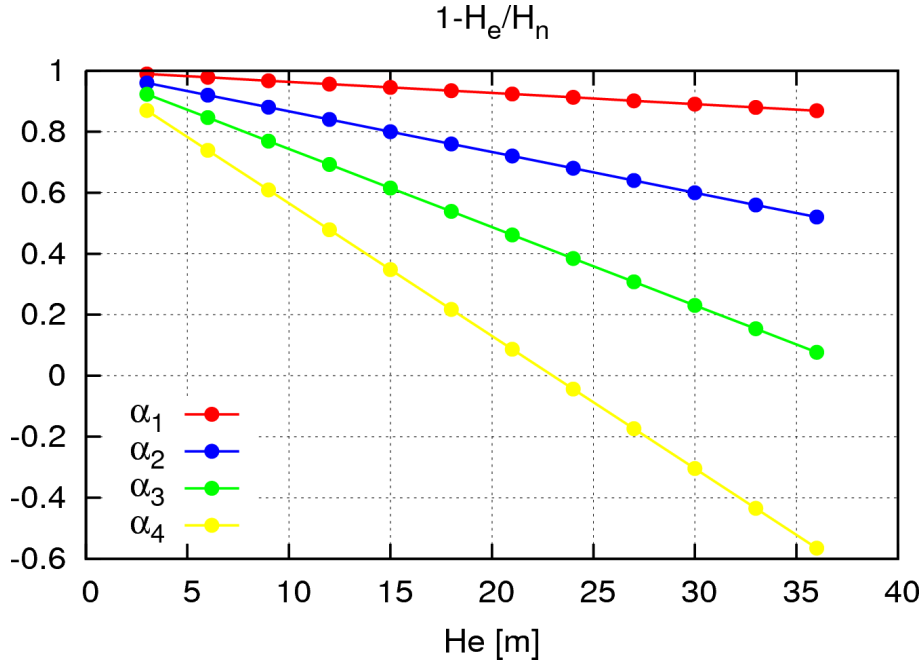


**Fig. 4.6:**  $\tilde{\alpha}_n$  vs  $H_e$  for the first four modes.  $H_e$  is changed from 3 to 36 m with an interval of 3 m.

and reduced static stability. Figure 4.6 shows  $\tilde{\alpha}_n$  within a range of  $H_e$  between 3 and 36 m. The value of  $\tilde{\alpha}_n$  decreases more steeply in the higher mode owing to the shallower  $H_n$ . Eq. (4.7) confirms that, for a given  $n$ ,  $\alpha_n$  approaches unity, i.e., the effective static stability decreases with  $H_e$  and hence with the phase speed as argued in the literature. Another implication of Eq. (4.7) is that the higher mode has a smaller  $\alpha_n$  when different moist modes have a common  $H_e$ . It follows that adiabatic heating cancels diabatic cooling more weakly in a higher mode for non-dispersive waves (e.g., Eq. (4.2)). In fact, Fig. 4.5 suggests that different moist modes have a common phase speed (or equivalent depth).

However, it is not obvious if Eq. (4.7) holds for each vertical mode. Haertel and Kiladis (2004) suggested, for the first and second modes in 2-day waves produced by a linear primitive equation model, that a degree of reduction of the equivalent depth depends on that of static stability. Haertel et al. (2008) also showed that  $\alpha_1$  is larger than  $\alpha_2$  and  $\alpha_3$  in COARE-2-day waves, which is roughly consistent with Haertel and Kiladis (2004). More observational evidence is needed to verify Eq. (4.7). Therefore, we estimate  $\alpha_n$  in section 4.4.2 and discuss the validity of Eq. (4.7) in section 4.5.

#### 4.4.2 Estimating of $\alpha_n$

Now  $\alpha_n$  is calculated according to Eq. (4.2). The mode transform components  $\omega_n$  and  $Q_n$  are written as (see Eqs. (1.76) and (1.76))

$$\omega_n = -\nabla \cdot \hat{V}_n \int_{p_t}^p h_n dp \quad (4.8)$$

$$Q_n = \hat{D}_n S \int_{p_t}^p h_n dp \quad (4.9)$$

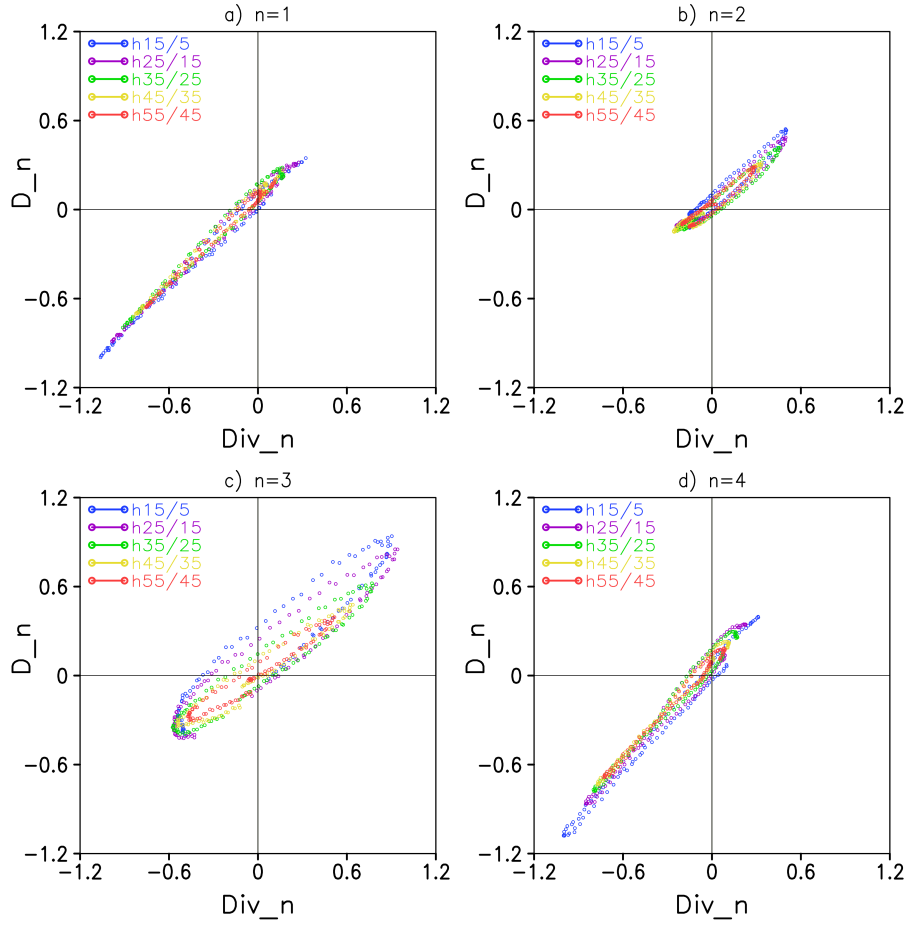


**Fig. 4.7:** A scatter plot of  $\nabla \cdot \hat{V}_n$  and  $\hat{D}_n$  between  $\pm 24$  hr. for the first four modes. Different colors represent different phase speed.

where  $\nabla \cdot \hat{V}_n$  and  $\hat{D}_n$  are the mode transform coefficients of horizontal wind divergence  $\nabla \cdot V_n$  and forced divergence  $D$ , respectively. In this study,  $Q$  is calculated as the apparent heat source (Yanai et al. 1973). Substituting Eqs. (4.8) and (4.9) in (4.2) gives

$$\begin{aligned} \alpha_n &= -\frac{Q_n}{S\omega_n} \\ &= \frac{\hat{D}_n}{\nabla \cdot \hat{V}_n} \end{aligned} \quad (4.10)$$

It is implied from Eq. (4.10) that  $\alpha_n$  may be evaluated from the nominator and dominator of the rhs. Figure 4.7 is the scatterplot of  $\nabla \cdot \hat{V}_n$  vs  $\hat{D}_n$  for the slower and faster waves. These two quantities are distributed tightly around a linear line in the first and fourth modes (Fig. 4.7a,d). Meanwhile, they are more scattered for the second and third modes (Fig. 4.7b,c). In the present study,  $\alpha_n$  is calculated as the least square coefficient between  $\hat{D}_n$  and  $\nabla \cdot \hat{V}_n$ . Figure 4.8 shows  $\alpha_n$  for the first four modes. The values of the estimated  $\alpha_n$  is positive and smaller than 1 as expected, except in the fourth mode (Fig. 4.8). In the slowest wave, with a phase speed of  $15 \text{ m s}^{-1}$  (the h15/5 filter),  $\alpha_1 = 0.96$ ,  $\alpha_2 = 0.85$ ,

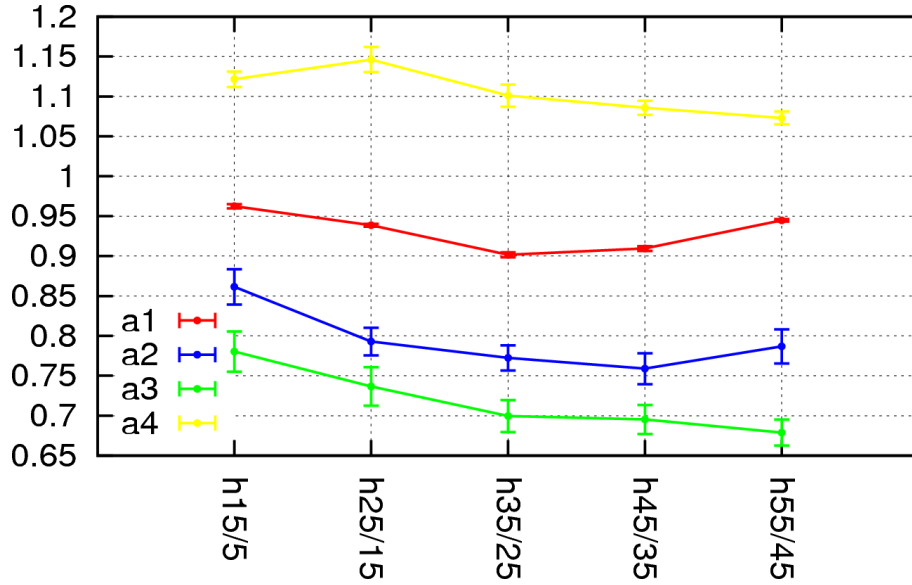


**Fig. 4.8:**  $\alpha_n$  calculated as a least square coefficient between  $\nabla \cdot \hat{V}_n$  and  $\hat{D}_n$  in Fig. 4.7. Different color denotes different mode.

and  $\alpha_3 = 0.75$ . This is roughly consistent with [Haertel and Kiladis \(2004\)](#) who shows that  $\alpha_1 = 0.95$  and  $\alpha_2 = 0.75$  in 2-day waves with a phase speed of  $16 \text{ m s}^{-1}$ . In [Haertel and Kiladis \(2004\)](#),  $\alpha_n$  is estimated as a ratio between  $Q_n$  and  $S\omega_n$  at a pressure of the maximum variances. It is noted that the value of  $\alpha_n$  is not so sensitive to the method of estimation (not shown here). If  $\alpha_n$  is larger than 1,  $S_e$  or  $H_e$  may have a negative value. Because of this apparent error in the estimate of  $\alpha_n$ , the fourth mode is excluded in the following discussion by using Eq. (4.7).

Figure 4.8 illustrates how  $\alpha_n$  differs among different equivalent depths. First,  $\alpha_n$  is smaller in the higher mode ( $\alpha_1 > \alpha_2 > \alpha_3$ ), implying that different moist modes have a common  $H_e$  or phase speed (Fig. 4.5). Second, the slower wave has a larger  $\alpha_n$ . These results could suggest that Eq. (4.7) qualitatively holds regardless of the wave speed. It is postulated that  $\alpha_n$  decreases with an equivalent depth at a rate of  $-1/H_n$ . However,  $\alpha_n$  for a given vertical mode appears not to decrease with the equivalent depth as sharply as expected from Eq. (4.7). This issue is investigated further in the next section.

The curve of  $\alpha_n$  is slightly bent in the faster waves. For example,  $\alpha_1$  ( $\alpha_2$ ) increases with an equivalent depth between h35/25 and h55/45 (h45/35 and h55/45). The bend in the curves may have resulted from uncertainties in the estimated  $\alpha_n$ . Both  $\nabla \cdot \hat{V}_n$  and  $\hat{D}_n$  have smaller amplitudes of variability in the faster waves than in the slower waves (Fig. 4.7), indicating that the WIG filter with higher equivalent depth identifies relatively weaker convective peaks of the WIG waves. Therefore, the composite fields may be less robust in the faster waves, leading to the larger uncertainties of the estimated  $\alpha_n$ .

## 4.5 Discussion

### 4.5.1 The Doppler effects

The equivalent depth of CCEWs is modified by the Doppler effect due to the ambient flow (e.g., [Yang et al. 2003](#)). For example, the equivalent depth of the WIG waves, observed during December-February in the southern hemisphere, is estimated to be about 20 m when considering the Doppler effect of the mean westerly flow at 850 hPa ([Takayabu 1994b](#)). Further, the spectral peak of the WIG waves is shown to be weakly affected by the Doppler shifting due to the mean barotropic flow, where the equivalent depth of 25 m is obtained ([Dias and Kiladis 2014](#)).

In the present study, the equivalent depth of the composite WIG waves is estimated by taking into account the Doppler effect due to mean zonal flow into the dispersion curves. The mean zonal wind  $\bar{u}$  is defined as the time mean ( $\pm 48$  h) of composite zonal wind at the composite center. Figure 4.9 shows the vertical profile of  $\bar{u}$  for the slower and faster WIG waves. The mean wind is easterly in the whole troposphere, and the profile is insensitive to the difference in the wave speed, suggesting that 2-day waves are sampled from a relatively uniform background condition regardless of their propagation characteristics.

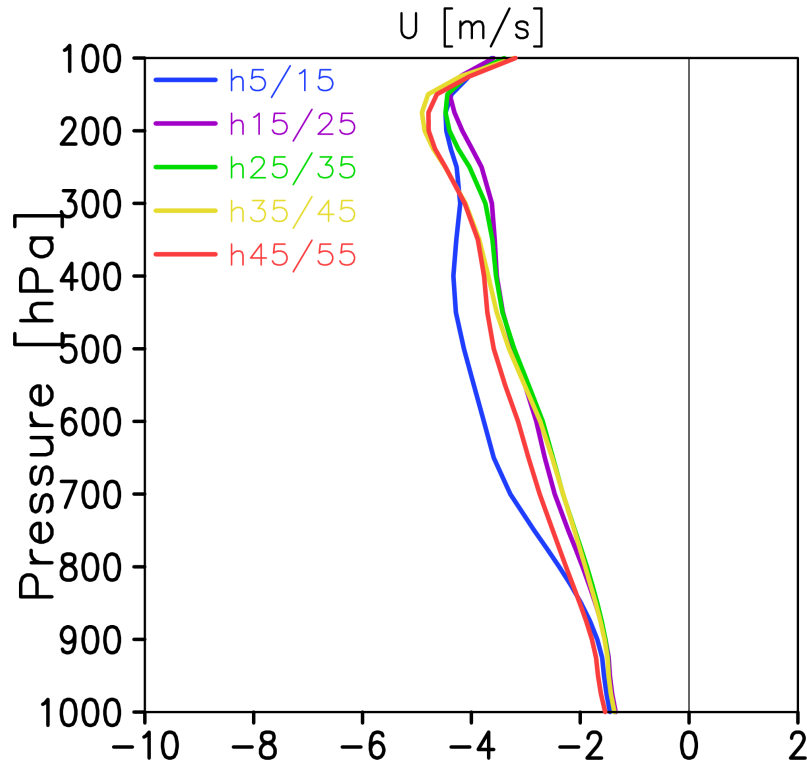


**Fig. 4.9:** Vertical profile of mean zonal wind  $\bar{u}$  [m/s]. The mean zonal wind  $\bar{u}$  is defined as a time mean ( $\pm 48$  hr) of composite zonal wind at a composite center. Different color represents different phase speed of WIG wave.

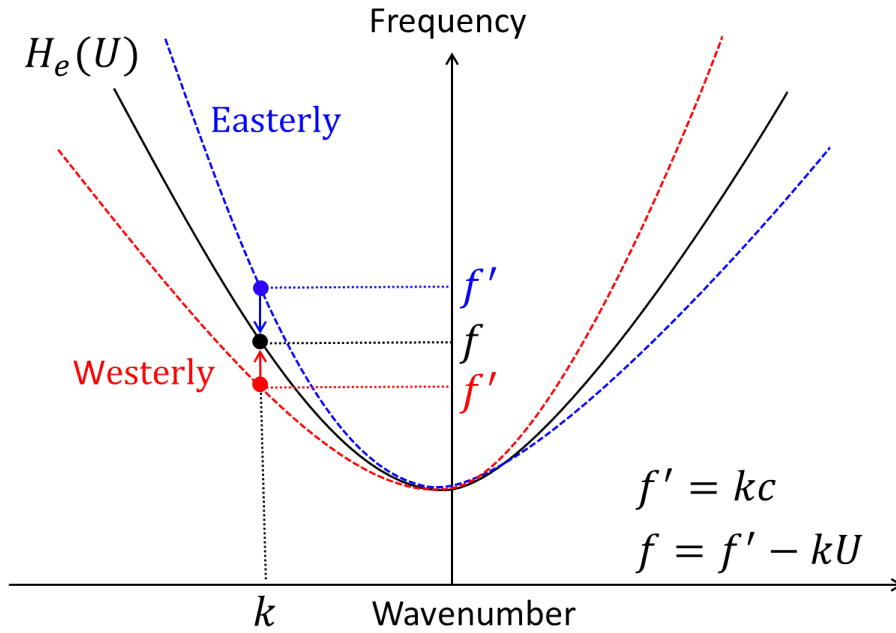


**Fig. 4.10:** A schematic of dispersion curves of WIG wave considering Doppler effect by a mean zonal flow.  $f'$  (dashed curves) and  $f$  (black solid curve) denote frequency excluding and including Doppler effect, respectively. Blue (red) dashed curve represents dispersion curve under mean easterly (westerly) flow.

Figure 4.10 shows how dispersion curve of WIG wave is shifted by considering Doppler effect by mean zonal wind. As the wave number ( $k$ ) is negative in the westward wave, the frequency ( $f$ ) decreases by the easterly flow (e.g.,  $f - k\bar{u}$ ). Hence, the equivalent depth becomes shallower as easterly flow gets stronger. To assess the Doppler shift, we choose three mean zonal flows at different pressure levels:  $\bar{u}$  at 850 hPa ( $U_{850}$ ),  $\bar{u}$  at 200 hPa ( $U_{200}$ ), and the pressure averaged  $\bar{u}$  from 850 to 200 hPa ( $U_{ave}$ ). As seen in Fig. 4.9, the mean zonal flow and the phase speed do not show any significant correlation (Table. 4.1). Therefore, it is suggested that mean zonal flow would have little influence on the wave speed. This result is consistent with Yasunaga and Mapes (2014) and shows that background wind has little effect on the propagation speed of WIG waves.

**Table 4.1:** Phase speed and mean flow for each WIG wave identified with different WIG filter.

<i>filter</i>	$c$ [ $\text{m s}^{-1}$ ]	$U_{850}$ [ $\text{m s}^{-1}$ ]	$U_{ave}$ [ $\text{m s}^{-1}$ ]	$U_{200}$ [ $\text{m s}^{-1}$ ]
h15/5	15	2.0	3.2	4.5
h25/15	21	1.7	2.8	4.2
h35/25	23	1.7	2.6	4.4
h45/35	26	1.7	2.9	4.9
h55/45	28	2.0	3.2	4.8

**Table 4.2:** Zonal wave number  $k$ , frequency  $f$  [cpd], and equivalent depth  $H_e$  [m].

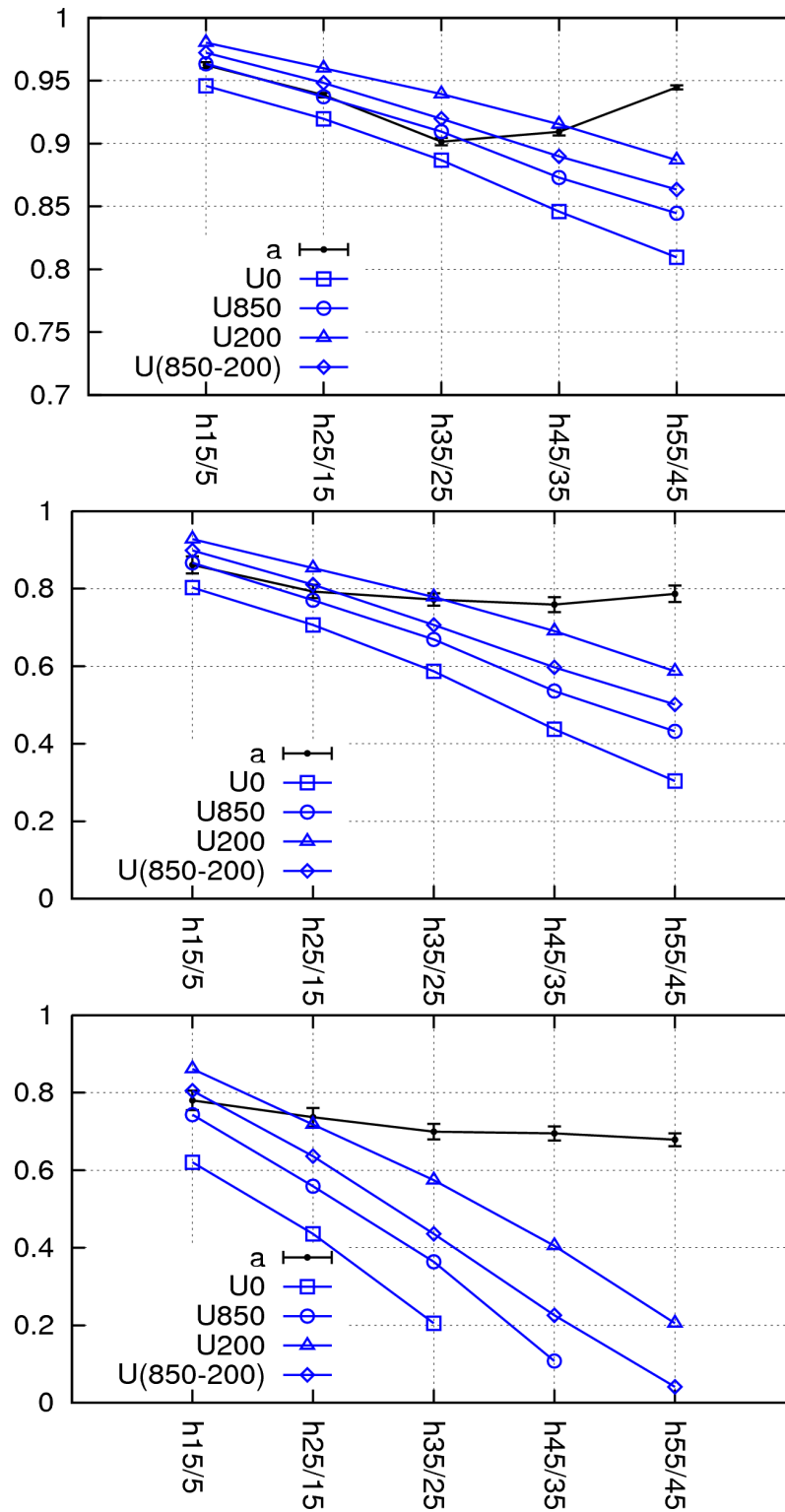
<i>filter</i>	$k$	$f(U_0)$	$f(U_{850})$	$f(U_{ave})$	$f(U_{200})$	$H_e(U_0)$	$H_e(U_{850})$	$H_e(U_{ave})$	$H_e(U_{200})$
h15/5	13.89	0.50	0.43	0.39	0.54	14.8	10.0	7.60	5.40
h25/15	9.92	0.50	0.46	0.43	0.40	22.0	17.2	14.2	11.0
h35/25	10.35	0.57	0.53	0.51	0.46	31.0	24.8	22.0	16.6
h45/35	10.12	0.63	0.59	0.56	0.51	42.2	34.8	30.2	23.2
h55/45	10.20	0.69	0.64	0.61	0.57	52.2	42.6	27.4	31.0

Table 4.2 summarized  $H_e(U)$  estimates by considering the Doppler effect due to the mean flows. Note that  $H_e(U_0)$  denotes  $H_e$  estimated by considering no Doppler effect ( $\bar{u} = 0$ ). The equivalent depth of the composite WIG wave is always shallower than that of the upper boundary of the WIG filter. As expected theoretically, it is implied that  $H_e(U)$  becomes shallower due to the strong easterly flow and that the slower wave has a shallower  $H_e(U)$ .

#### 4.5.2 $\alpha_n$ versus $\tilde{\alpha}_n$

It is suggested from Eq. (4.7) that the reduced equivalent depth of the moist vertical mode can be explained by reduced static stability. To see if Eq. (4.7) holds,  $\alpha_n$  in Fig. 4.8 is compared with  $\tilde{\alpha}_n$ . Here,  $\tilde{\alpha}_n$  is estimated using  $H_e(U)$  in Table 4.2, and it is expressed as  $\tilde{\alpha}_n(U)$ . The relationship between  $\alpha_n$  (black line) and  $\tilde{\alpha}_n(U)$  (blue line) is shown for the first three vertical modes in Fig. 4.11. Blue square, circle, triangle, and diamond marks resemble  $\tilde{\alpha}_n(\bar{u}_0)$ ,  $\tilde{\alpha}_n(\bar{u}_{850})$ ,  $\tilde{\alpha}_n(\bar{u}_{200})$ , and  $\tilde{\alpha}_n(\bar{u}_{ave})$ , respectively.

First,  $\alpha_1$  and  $\tilde{\alpha}_1(U)$  are compared. The value of  $\alpha_1$  is almost identical to that of  $\tilde{\alpha}_1(U_{850})$  in the slower wave (h15/5-h35/25), where  $\alpha_1$  changes with  $H_1$  nearly at the rate of  $\sim -1/H_1$ . Meanwhile,  $\alpha_1$  is no longer consistent with  $\tilde{\alpha}_1(U_{850})$  for larger equivalent depths (h45/35-h55/45). Second,  $\alpha_2$  and  $\tilde{\alpha}_2(U)$  are compared. The value of  $\alpha_2$  is nearly identical to that of  $\tilde{\alpha}_2(\bar{u}_{850})$  in the slower wave (h15/5-h25/15), where a decreasing rate of  $\alpha_2$  is roughly close to that of  $\tilde{\alpha}_2 (= -1/H_2)$ . However,  $\alpha_2$  decreases with increasing  $H_2$  more modestly than  $\tilde{\alpha}_2$  in the wave speed with a range of 21 to 28  $\text{m s}^{-1}$  (h25/15-h55/45). Finally, we compare  $\alpha_3$  and  $\tilde{\alpha}_3(U)$ . It is clearly shown that a decreasing rate of  $\alpha_3$  never agrees with that of  $\tilde{\alpha}_3 (= -1/H_3)$ . The value of  $\alpha_3$  in the slowest wave (h15/5) is roughly equal to that of  $\tilde{\alpha}_3(U_{850})$ . For the second and third vertical modes, Eq. (4.7) hardly explains the actual values of  $\alpha_n$  with the possible exception that Eq. (4.7) could be barely applicable to the slower wave with a range of 15 to 21  $\text{m s}^{-1}$  (h15/5-h25/15). In the next section, we will further discuss the discrepancy between  $\alpha_n$  and  $\tilde{\alpha}_n$ .



**Fig. 4.11:**  $\alpha_n$  (black) vs  $\tilde{\alpha}_n$  (blue) for the first three modes: (top)  $n = 1$ , (middle)  $n = 2$ , and (bottom)  $n = 3$ .

### 4.5.3 The reduced stability mechanism

The mechanism of slowdown of the WIG wave is discussed in terms of both the effective stability mechanism and the vertical mode perspectives (see section 1.2.3). The effective stability mechanism explains the slower phase speed of the first vertical mode by a reduced stability due to the latent heat release (e.g., Emanuel et al. 1994). This is approximately expressed by Eq. (4.7), claiming that reduced equivalent depth is connected with reduced static stability. It is implied from Eq. (4.7) that a higher vertical mode should have a higher effective static stability (a lower  $\alpha_n$ ) so the wave as whole is heavily dispersive.

It is not intuitively obvious how the effective stability mechanism explains the slowdown of the higher modes. To address the question, the relationship between a reduction in equivalent depth and that in static stability is examined in section 4.5.2 by comparing  $\alpha_n$  and  $\tilde{\alpha}_n$ . The main findings are summarized as follows. First,  $\alpha_n$  is roughly identical to  $\tilde{\alpha}_n(U_{850})$  in the slower waves, especially for the first vertical mode. Second, a decreasing rate of  $\alpha_1$  as a function of equivalent depth is quantitatively consistent with that of  $\tilde{\alpha}_1(U_{850})(= -1/H_1)$  in the slower waves. For the second and third modes,  $\alpha_n$  decreases more modestly than  $\tilde{\alpha}_n(U_{850})(= -1/H_n)$ . Therefore, it is confirmed that Eq. (4.7) may hold for the lowest vertical modes but fails to predict  $\alpha_n$  for higher modes. This does not contradict previous studies (Haertel and Kiladis 2004; Haertel et al. 2008).

There are a variety of possible explanations for the discrepancy between  $\alpha_n$  and  $\tilde{\alpha}_n$ . First, the estimation of  $\alpha_n$  has its own uncertainties. As expressed in Eq. (4.10),  $\alpha_n$  is evaluated as the least square coefficient between  $\hat{D}_n$  and  $\nabla \cdot \hat{V}_n$  (Fig. 4.7). While  $\hat{D}_n$  and  $\nabla \cdot \hat{V}_n$  are almost linearly changed with each other for the first mode, the ratio of  $\hat{D}_n$  to  $\nabla \cdot \hat{V}_n$  changes with time for the second and third modes. Therefore, it is considered that the errors in  $\alpha_n$ , estimated as a time-independent parameter, should be larger in the higher modes than in the first mode. The time dependency of  $\alpha_2$  and  $\alpha_3$  should be included to estimate  $\alpha_n$  more adequately. It is, however, beyond the scope of the present study to discuss to what extent such a modification improves the estimation of  $\alpha_n$ . Second,  $\alpha_n$  is, by definition, a vertical uniform parameter, but this property is readily justifiable only for the first mode. In Eq. (4.2),  $\alpha_n$  represents the degree of cancellation between adiabatic heating (cooling) and diabatic cooling (heating) due to ascent (descent). In the literature, the effective stability has been introduced to explain the large-scale motion involving deep convection (the first mode) (e.g., Neelin and Held 1987; Yano and Emanuel 1991; Neelin and Yu 1994; Emanuel et al. 1994), where the atmosphere is assumed to be in a state of precipitation to ignore the descending area with no precipitation (Emanuel et al. 1994). This is because the formulation of the effective stability is further complicated by the inclusion of a descending area. As shown in Fig. 4.3, the vertical profiles of  $\omega_n$  and  $Q_n$  have a multi-pole structure for the second and higher modes, for which it is physically impossible to define vertically uniform  $\alpha_n$ . We estimate the degree of the reduction in static stability ( $S_e/S$ ) by simply assuming a constant  $\alpha_n$  (Eq. (4.2)), where the ascending and descending motions are not treated separately. Such simplicity might have a non-trivial influence on the estimation of  $\alpha_2$  or  $\alpha_3$ .

## 4.6 Summary

In this chapter, the slowdown mechanism of quasi-2-day waves is examined using satellite and reanalysis data. The 2-day waves with different phase speed are identified by WIG filtering of TBB, where the wave speeds are separated by adopting WIG sub-filters with different equivalent depths within a range from 5 to 55 m. ERAI data are composited around the convective peaks of WIG waves to analyze the large-scale fields associated with the waves. The composite fields are further decomposed by the vertical modes calculated with the mean temperature profile (ERAI) in the tropical region between  $10^{\circ}\text{N}$  and  $10^{\circ}\text{S}$ .

It is shown that the large-scale dynamical fields of WIG waves are explained largely by a superposition of the first four baroclinic modes. The resulting vertically tilted, top-heavy structure is consistent with the multi-mode structure, including the deep, congestus, and stratiform modes (e.g., [Mapes 2000](#); [Haertel et al. 2008](#)). The phase speeds of moist vertical modes is estimated by Radon transform of the mode coefficient in the longitude-time domain. The moist vertical modes are slowed down compared to its dry counterpart, while different vertical modes have similar phase speeds, so the wave is only weakly dispersive. The above results are insensitive to the difference in the filter design.

In the effective stability mechanism, the slower phase speed of the first mode is attributed to the reduction of effective stability. It is not obvious, however, if the slowdown of the higher modes is also explained by a similar framework. The effective stability increases with the equivalent depth as expected from the non-dispersive nature, but the rate of increase is not as steep as theoretically predicted. This disagreement is partially reconciled particularly for the lowest modes when the Doppler effect is taken into account, but fails to account for higher modes. The reasons include the limitation in the estimation method and physical robustness of the effective stability for the higher vertical modes. Further investigations of these outstanding issues should be addressed in future studies.

# Chapter 5

## Summary

The present study investigates physical properties of quasi-2-day waves by using satellite and reanalysis data to better understand the interaction between moist convection and a large-scale circulation in the tropical atmosphere.

In chapter 3, thermodynamic properties of 2-day waves are examined using moist static energy (MSE) which is nearly conserved in moist adiabatic process. Vertically integrated MSE budget equation is used for investigating MSE recharge-discharge process of the waves. The budget terms are calculated from reanalysis data and composited around the convective peaks of the waves. Column MSE increases before deep convection (recharge process) and decreases as convection develops (discharge process). Variability of column MSE is mainly dominated by advection term. Meanwhile, surface heat fluxes and radiative heating terms scarcely change with time during wave development, and hardly contribute to the MSE change. A prominent zonal advection by mean zonal wind is found to exist and significantly contributes to horizontal advection, while this term should be considered not to be closely relevant to the wave dynamics. Instead, the recharge-discharge process is mainly regulated by vertical MSE advection. The vertical advection decreases MSE around the convective peak, plausibly resulting from the first baroclinic mode associated with deep convection. An increase of positive vertical advection due to shallow convection has a relatively smaller amplitude than expected from previous studies. The above result, however, is qualitatively consistent with theoretical models explaining the recharge-discharge process by a large-scale vertical circulation. The normalized gross moist stability (NGMS) is used to examine the relationship between large-scale circulation and convective intensity. NGMS decreases to 0 before deep convection. According to the development of deep convection, NGMS increases and reaches its maximum after the convective peak. The lower NGMS seems to be related to amplification of deep convection. This result is consistent with the previous study indicating that temporal variability of NGMS is more prominent for the waves with short time scale such as 2-day waves.

In chapter 4, slow down mechanism of 2-day waves is examined focusing on a slow-down of vertical modes associated with the wave dynamics. It is shown, using a vertical mode transform technique, that the large-scale fields of 2-day waves are explained by a superposition of first four baroclinic modes. The resulting vertically tilted, top-heavy structure is consistent with the multi-mode model, including the deep, congestus, and stratiform modes. The phase speeds of moist vertical modes are slower than their dry

counterparts, while different modes have similar slow phase speed, suggesting that the wave is only weakly dispersive. In the effective stability mechanism, a slowdown of the first mode is explained by a reduction of effective static stability due to the latent heat release. In the present study, the mechanism of slowdown of each vertical modes is investigated from estimating effective static stability individually for each mode. The effective static stability is evaluated by defining the degree of cancellation between diabatic heating and adiabatic cooling. The cancellation is larger (smaller) in the first mode (the higher modes), leading to smaller (larger) effective static stability. This is qualitatively as expected for the weak dispersiveness of the moist vertical modes. The relationship between effective static stability and reduced equivalent depth is examined for each vertical modes. In the first mode, as expected from the theoretical model, the shallow equivalent depth is qualitatively explained by effective static stability. In the higher modes, however, discrepancy from the theoretical prediction becomes large, implying that the effective stability mechanism may be inappropriate to explain the slowdown of the higher modes.

This discrepancy remains even with the Doppler effect considered. The discrepancy may be associated with uncertainties in the estimation of  $\alpha_n$ , where  $\alpha_n$  is assumed to be a time-independent and vertically uniform by design. The above assumptions are valid for the first mode with a single-signed structure as proposed in the reduced stability model. Meanwhile, some modifications would be needed for the higher modes, since their dipole-like structure makes the assumptions more complicated: upward and downward motions occur simultaneously at different height, affecting inhomogeneously the effective static stability. Applying the reduced stability to the higher mode should be dealt with carefully in the future analysis. Finally, it should be noted again that the two theoretical models for the phase speed of CCEWs, the reduced stability model and multi-mode model, are not mutually exclusive to each other. It is possible that the two theories may work together for determining the phase speed, while a further investigation in this direction is beyond the scope of the present study. The physical factors controlling the phase speed will be examined in more depth in the future.

# Chapter 6

## Supplement to theoretical background

### 6.1 Shallow water equations

In this section, we derive the equations of motion and mass continuity in shallow water system (see section 1.3.1). The equation of motion in 3D is written as:

$$\frac{D\mathbf{v}}{Dt} = -\frac{1}{\rho}\nabla p - f\mathbf{k} \times \mathbf{v} - g\mathbf{k} + \mathbf{F} \quad (6.1)$$

where  $t$  is time,  $\mathbf{v} = (u, v, w)$  is the three-dimensional velocity of a parcel of air,  $\rho$  is the density of the air,  $p$  is pressure of the atmosphere,  $f$  is Coriolis parameter,  $g$  is the acceleration of gravity,  $\mathbf{k}$  is unit vector in the  $z$  direction, and  $\mathbf{F}$  is frictional acceleration.  $\nabla = (\partial/\partial x, \partial/\partial y, \partial/\partial z)$  is differential operator. The first and second terms in the rhs in Eq. (6.1) are the pressure gradient force and Coriolis force, respectively. The Coriolis parameter  $f$  is written as:

$$f = 2\Omega \sin\theta \quad (6.2)$$

where  $\Omega$  is the angular speed of the earth's rotation and  $\theta$  is latitude. Taylor expansion of  $f$  around angular  $\theta_0$  is written as

$$f \sim 2\Omega (\sin\theta_0 + \cos\theta_0(\theta - \theta_0) + \dots) \quad (6.3)$$

$$\sim f_0 + \beta y \quad (6.4)$$

where  $f_0 = 2\Omega \sin\theta_0$ ,  $\beta = 2\Omega \cos\theta_0/R$ , and  $R$  is the earth's radius. Note that  $y \sim R(\theta - \theta_0)$ .

We neglect  $\mathbf{F}$ , Eq. (6.1) is written in  $x$ ,  $y$ , and  $z$  components.

$$\frac{\partial u}{\partial t} = -\frac{1}{\rho} \frac{\partial p}{\partial x} + fv \quad (6.5)$$

$$\frac{\partial v}{\partial t} = -\frac{1}{\rho} \frac{\partial p}{\partial y} - fu \quad (6.6)$$

$$\frac{\partial w}{\partial t} = -\frac{1}{\rho} \frac{\partial p}{\partial z} - g \quad (6.7)$$

We assume the hydrostatic balance in the  $z$  direction

$$\frac{\partial \phi}{\partial p} = -\frac{1}{\rho} \quad (6.8)$$

where  $\phi = gz$  is geopotential. The pressure gradient force in the  $x$  and  $y$  direction is rewritten as;<sup>1</sup>

$$-\frac{1}{\rho} \frac{\partial p}{\partial x} = -\frac{\partial \phi}{\partial x} \quad (6.9)$$

$$-\frac{1}{\rho} \frac{\partial p}{\partial y} = -\frac{\partial \phi}{\partial y} \quad (6.10)$$

Substituting Eqs. (6.8)-(6.10) into (6.7), we finally obtain

$$\frac{\partial u}{\partial t} = -\frac{\partial \phi}{\partial x} + fv \quad (6.11)$$

$$\frac{\partial v}{\partial t} = -\frac{\partial \phi}{\partial y} - fu \quad (6.12)$$

$$\frac{\partial \phi}{\partial p} = -\frac{1}{\rho} \quad (6.13)$$

Continuity equation in incompress fluid is expressed as;

$$\frac{\partial u}{\partial x} + \frac{\partial v}{\partial y} + \frac{\partial w}{\partial z} = 0 \quad (6.14)$$

By integrating Eq. (6.14) by  $z$  from 0 to  $z$ , and using  $w(z) = dz/dt$ , we obtain

$$\left( \frac{\partial u}{\partial x} + \frac{\partial v}{\partial y} \right) z + \frac{dz}{dt} = 0 \quad (6.15)$$

Averaging Eqs. (6.13) and (6.15) over the horizontal area, and applying the Reynolds averaging technique, we obtain

$$\frac{\partial u'}{\partial t} = -\frac{\partial \phi'}{\partial x} + fv' \quad (6.16)$$

$$\frac{\partial v'}{\partial t} = -\frac{\partial \phi'}{\partial y} - fu' \quad (6.17)$$

$$\left( \frac{\partial u'}{\partial x} + \frac{\partial v'}{\partial y} \right) \bar{z} + \frac{dz'}{dt} = 0 \quad (6.18)$$

---

<sup>1</sup>Pressure gradient force in the  $x$  direction ( $PGF_x$ ) is expressed as;

$$PGF_x = -\frac{1}{\rho} \left( \frac{\partial p}{\partial x} \right)$$

Using Maxwell's rule and the hydrostatic equation, the pressure gradient in the  $x$  direction is written as

$$\left( \frac{\partial p}{\partial x} \right)_z = - \left( \frac{\partial p}{\partial z} \right)_x \left( \frac{\partial z}{\partial x} \right)_p = \rho \left( \frac{\partial \phi}{\partial x} \right)_p$$

Eq. (6.9) is rewritten as;

$$-\frac{1}{\rho} \left( \frac{\partial p}{\partial x} \right) = - \left( \frac{\partial \phi}{\partial x} \right)$$

where the bar denotes the horizontal average and the prime denotes the deviation from the average.

Now we consider shallow water system. Substituting  $\bar{z} = H$  and  $z' = h$  into Eqs. (6.18), we finally obtain the equations of motion and mass conservation in the shallow water system as follows.

$$\frac{\partial u'}{\partial t} = -g \frac{\partial h}{\partial x} + f v' \quad (6.19)$$

$$\frac{\partial v'}{\partial t} = -g \frac{\partial h}{\partial y} - f u' \quad (6.20)$$

$$\left( \frac{\partial u'}{\partial x} + \frac{\partial v'}{\partial y} \right) H + \frac{dh}{dt} = 0 \quad (6.21)$$

## 6.2 Vertical mode transform of temperature, pressure velocity, and heating rate

### 6.2.1 Temperature

From the hydrostatic equation (Eq. (1.40)), temperature is written as

$$T = -\frac{1}{R} \frac{\partial \phi}{\partial \ln p} \quad (6.22)$$

The temperature is expressed in a discrete form as follows;

$$T = \sum_{n=0}^{\infty} T_n \quad (6.23)$$

where  $T_n$  is the  $n$ -th mode transform component of temperature. Here  $T_n$  and  $\phi_n$  are written as

$$\begin{aligned} T_n &= \hat{T}_n \psi_n \\ \phi_n &= \hat{\phi}_n h_n \end{aligned} \quad (6.24)$$

where  $\psi_n$  is the structure function of temperature. Substituting Eqs. (6.24) into (6.22) yields

$$T_n = -\frac{1}{R} \hat{\phi}_n \frac{\partial h_n}{\partial \ln p} \quad (6.25)$$

Here  $\psi_n$  (dimensionless) and  $\hat{T}_n$  ([K]) are written as

$$\begin{aligned} \psi_n &= a_n \frac{\partial h_n}{\partial \ln p} \\ \hat{T}_n &= -\frac{1}{R} \hat{\phi}_n \frac{1}{a_n} \end{aligned} \quad (6.26)$$

Normalize coefficient  $a_n$  (dimensionless) is calculated from the orthogonal condition ( $\langle \psi_n | \psi_n \rangle = 1$ ).

## 6.2.2 Pressure velocity

From the continuity equation (Eq. (1.42)), pressure velocity is written as

$$\omega(p) = - \int_{p_t}^p \left( \frac{\partial u}{\partial x} + \frac{\partial v}{\partial y} \right) dp \quad (6.27)$$

,where  $\omega(p_t) = 0$ . The pressure velocity is expressed in a discrete form as follows;

$$\omega = \sum_{n=0}^{\infty} \omega_n \quad (6.28)$$

where  $\omega_n$  is the  $n$ -th mode transform component of pressure velocity. Here,  $\omega_n$ ,  $u_n$ , and  $v_n$  are written as

$$\begin{aligned} \omega_n &= \hat{\omega}_n \psi_n \\ u_n &= \hat{u}_n h_n \\ v_n &= \hat{v}_n h_n \end{aligned} \quad (6.29)$$

where  $\psi_n$  is structure function of pressure velocity. Substituting Eqs. (6.29) into (6.27) yields

$$\omega_n = - \left( \frac{\partial \hat{u}_n}{\partial x} + \frac{\partial \hat{v}_n}{\partial y} \right) \int_{p_t}^p h_n dp \quad (6.30)$$

Then  $\psi_n$  (dimensionless) and  $\hat{\omega}_n$  ([pa/s]) are written as

$$\begin{aligned} \psi_n &= a_n \int_{p_t}^p h_n dp \\ \hat{\omega}_n &= -\frac{1}{a_n} \left( \frac{\partial \hat{u}_n}{\partial x} + \frac{\partial \hat{v}_n}{\partial y} \right) \end{aligned} \quad (6.31)$$

Normalize coefficient  $a_n$  ([1/pa]) is calculated from the orthogonal condition ( $\langle \psi_n | \psi_n \rangle = 1$ )

## 6.2.3 Heating rate

From the definition of forced divergence (Eq. (1.51)),

$$D = \frac{\partial}{\partial p} \left( \frac{Q}{Sc_p} \right) \quad (6.32)$$

Integrating both sides of Eq. (6.32) yields

$$\left( \frac{Q}{Sc_p} \right)_p = \left( \frac{Q}{Sc_p} \right)_{p_t} + \int_{p_t}^p D dp \quad (6.33)$$

Using the thermodynamic equation ((Eq. (1.41)), we obtain

$$\left( \frac{Q}{Sc_p} \right)_{p_t} = \left( \frac{1}{S} \frac{\partial T}{\partial t} - \omega \right)_{p_t} = 0 \quad (6.34)$$

,where we use the followings:

$$\omega(p_t) = 0 \quad (6.35)$$

$$\left(\frac{\partial T}{\partial t}\right)_{p_t} \propto \left(\frac{\partial h_n}{\partial p}\right)_{p_t} = 0 \quad (6.36)$$

Finally,  $Q$  is written as

$$Q = -Sc_p \int_{p_t}^p D dp \quad (6.37)$$

The heating rate is expressed in a discrete form as follows;

$$Q = \sum_{n=0}^{\infty} Q_n \quad (6.38)$$

The  $n$ -th mode transform component of heating rate  $Q_n$  and forced divergence  $D_n$  are written as

$$\begin{aligned} Q_n &= \hat{Q}_n \psi_n \\ D_n &= \hat{D}_n h_n \end{aligned} \quad (6.39)$$

where  $\psi_n$  is structure function of heating rate. Substituting Eqs. (6.39) into (6.37) yields

$$Q_n = -Sc_p D_n \int_{p_t}^p h_n dp \quad (6.40)$$

Then  $\psi_n$  (dimensionless) and  $\hat{Q}_n$  ([K/s]) are written as

$$\begin{aligned} \psi_n &= a_n S \int_{p_t}^p h_n dp \\ \hat{Q}_n &= \frac{1}{a_n} c_p D_n \end{aligned} \quad (6.41)$$

Normalize coefficient  $a_n$  ([1/K]) is calculated from the orthogonal condition ( $\langle \psi_n | \psi_n \rangle = 1$ )

### 6.3 Eigenvalue equation in discrete form

As described in section 1.4, the vertical modes are obtained by solving the eigenvalue equation (Eq. (2.5))

$$-\frac{\partial}{\partial p} \mu \frac{\partial}{\partial p} h_n = \lambda_n h_n \quad (6.42)$$

In this study, Eq. (6.42) is expressed in discrete form. The left hand side of Eq. (6.42) is rewritten as

$$\frac{\partial}{\partial p} \mu \frac{\partial}{\partial p} h_n = \frac{\partial \mu}{\partial p} \frac{\partial h_n}{\partial p} + \mu \frac{\partial^2 h_n}{\partial p^2} \quad (6.43)$$

As shown in Fig. 2.7,  $\mu$  and  $h_n$  are defined at the pressure level labeled with integer index  $k$ . Then,  $\partial\mu/\partial p$  and  $\partial h_n/\partial p$  are defined at the pressure level labeled with semi-integer index  $k + 1/2$ .

$$\left(\frac{\partial\mu}{\partial p}\right)_{k+1/2} = \frac{\mu_{k+1} - \mu_k}{\Delta p} \quad (6.44)$$

$$\left(\frac{\partial h_n}{\partial p}\right)_{k+1/2} = \frac{h_{n,k+1} - h_{n,k}}{\Delta p} \quad (6.45)$$

Also,  $\partial^2 h_n/\partial p^2$  is defined at pressure level labeled with integer index  $k$  and expressed as follows in the second order approximation.

$$\left(\frac{\partial^2 h_n}{\partial p^2}\right)_k = \frac{h_{n,k-1} - 2h_{n,k} + h_{n,k+1}}{\Delta p^2} \quad (6.46)$$

Consider Eq. (6.43) at the pressure level  $k$ :

$$\left(\frac{\partial}{\partial p}\mu\frac{\partial}{\partial p}h_n\right)_k = \left\langle\frac{\partial\mu}{\partial p}\frac{\partial h_n}{\partial p}\right\rangle_k^p + \mu_k\left(\frac{\partial^2 h_n}{\partial p^2}\right)_k \quad (6.47)$$

The first term of the rhs of Eq. (6.47) is defined as follows (see appendix in Durran (1999))

$$\begin{aligned} \left\langle\frac{\partial\mu}{\partial p}\frac{\partial h_n}{\partial p}\right\rangle_k^p &= \frac{1}{2}\left\{\left(\frac{\partial\mu}{\partial p}\frac{\partial h_n}{\partial p}\right)_{k+1/2} + \left(\frac{\partial\mu}{\partial p}\frac{\partial h_n}{\partial p}\right)_{k-1/2}\right\} \\ &= \frac{(\mu_{k+1} - \mu_k)(h_{n,k+1} - h_{n,k}) + (\mu_k - \mu_{k-1})(h_{n,k} - h_{n,k-1})}{2\Delta p^2} \\ &= \frac{(h_{n,k+1} - h_{n,k})\mu_{k+1} - (h_{n,k+1} - 2h_{n,k} + h_{n,k})\mu_k - (h_{n,k} - h_{n,k-1})\mu_{k-1}}{2\Delta p^2} \end{aligned} \quad (6.48)$$

The second term of the rhs of Eq. (6.47) is written as

$$\left(\mu\frac{\partial^2 h_n}{\partial p^2}\right)_k = \mu_k\frac{h_{n,k-1} - 2h_{n,k} + h_{n,k+1}}{\Delta p^2} \quad (6.49)$$

Substituting Eqs. (6.48) and (6.49) into (6.47) yields

$$\begin{aligned} \left(\frac{\partial}{\partial p}\mu\frac{\partial}{\partial p}h_n\right)_k &= -\frac{1}{2\Delta p^2}\left\{(\mu_{k+1} + \mu_k)h_{n,k+1} - (\mu_{k+1} + 2\mu_k + \mu_{k-1})h_{n,k} + (\mu_k + \mu_{k-1})h_{n,k-1}\right\} \\ &= -\frac{1}{\Delta p^2}\left\{\mu_{k+1/2}h_{n,k+1} - (\mu_{k+1/2} + \mu_{k-1/2})h_{n,k} + \mu_{k-1/2}h_{n,k-1}\right\} \end{aligned} \quad (6.50)$$

where  $\mu_{k+1/2}$  and  $\mu_{k-1/2}$  are defined as follows.

$$\mu_{k+1/2} = \frac{1}{2}(\mu_{k+1} + \mu_k) \quad (6.51)$$

$$\mu_{k-1/2} = \frac{1}{2}(\mu_k + \mu_{k-1}) \quad (6.52)$$

## 6.4 Boundary conditions in discrete form

The boundary conditions (Eq. (2.5)) are written as

$$\left(\frac{\partial h_n}{\partial p}\right)_{p_t} = 0 \quad (6.53)$$

$$\left(\frac{\partial h_n}{\partial p}\right)_{p_b} + \left(\frac{S h_n}{\bar{T}}\right)_{p_b} = 0 \quad (6.54)$$

where  $p_t$  and  $p_b$  locate at the pressure level  $k = -1/2$  and  $k = M + 1/2$ , respectively. In this section Eqs. (6.53) and (6.54) are expressed in discrete form. The upper boundary condition (Eq. (6.53)) in the difference form is expressed as

$$\left(\frac{\partial h_n}{\partial p}\right)_{-1/2} = \frac{h_{n,0} - h_{n,-1}}{\Delta p} = 0 \quad (6.55)$$

,which indicates  $h_{n,-1} = h_{n,0}$ . The bottom boundary condition (Eq. (6.54)) in the discrete form is

$$\left(\frac{\partial h_n}{\partial p}\right)_{M+1/2} + \left(\frac{S}{\bar{T}}\right)_{M+1/2} h_{n,M+1/2} = 0 \quad (6.56)$$

where

$$\begin{aligned} \left(\frac{\partial h_n}{\partial p}\right)_{M+1/2} &= \frac{h_{n,M+1} - h_{n,M}}{\Delta p} \\ h_{n,M+1/2} &= \frac{h_{n,M+1} + h_{n,M}}{2} \end{aligned} \quad (6.57)$$

Substituting Eqs. (6.57) into (6.56) yields

$$h_{n,M+1} = \frac{1 - a/2}{1 + a/2} h_{n,M} \quad (6.58)$$

where

$$a = \Delta p \left(\frac{S}{\bar{T}}\right)_{M+1/2} \quad (6.59)$$

The boundary conditions in discrete form are summarized as follows:

$$h_{n,-1} = h_{n,0} \quad (6.60)$$

$$h_{n,M+1} = \frac{1 - a/2}{1 + a/2} h_{n,M} \quad (6.61)$$

## 6.5 Temperature, pressure velocity, and heating rate in discrete form

### 6.5.1 Temperature

From Eq. (6.25),  $T_n$  is written as

$$T_n = -\frac{\hat{\phi}_n}{R} \frac{\partial h_n}{\partial \ln p} \quad (6.62)$$

Now  $T_n$  at the pressure level  $k$  is denoted by  $T_{n,k}$ .

$$\begin{aligned}
T_{n,k} &= -\frac{\hat{\phi}_n}{R} p_k \left\langle \frac{\partial h_n}{\partial p} \right\rangle_k^p \\
&= -\frac{\hat{\phi}_n}{R} p_k \frac{1}{2} \left\{ \left( \frac{\partial h_n}{\partial p} \right)_{k+1/2} + \left( \frac{\partial h_n}{\partial p} \right)_{k-1/2} \right\} \\
&= -\frac{\hat{\phi}_n}{R} p_k \frac{1}{2\Delta p} (h_{n,k+1} - h_{n,k} + h_{n,k} - h_{n,k-1}) \\
&= -\frac{\hat{\phi}_n}{R} \frac{p_k}{2\Delta p} (h_{n,k+1} - h_{n,k-1}) \tag{6.63}
\end{aligned}$$

$T_{n,k}$  ( $k = 0, \dots, M$ ) is written as follows.

$$\begin{aligned}
T_{n,0} &= -\frac{\hat{\phi}_n}{R} \frac{p_0}{2\Delta p} (h_{n,1} - h_{n,-1}) = -\frac{\hat{\phi}_n}{R} \frac{p_0}{2\Delta p} (h_{n,1} - h_{n,0}) \\
T_{n,1} &= -\frac{\hat{\phi}_n}{R} \frac{p_1}{2\Delta p} (h_{n,2} - h_{n,0}) \\
&\vdots \\
T_{n,M-1} &= -\frac{\hat{\phi}_n}{R} \frac{p_{M-1}}{2\Delta p} (h_{n,M} - h_{n,M-2}) \\
T_{n,M} &= -\frac{\hat{\phi}_n}{R} \frac{p_M}{2\Delta p} (h_{n,M+1} - h_{n,M-1}) = -\frac{\hat{\phi}_n}{R} \frac{p_M}{2\Delta p} (bh_{n,M} - h_{n,M-1}) \tag{6.64}
\end{aligned}$$

where  $b = (1 - a/2)/(1 + a/2)$  and  $a = \Delta p(S/\bar{T})_{pB}$ .

## 6.5.2 Pressure velocity

From Eq. (6.30),  $\omega_n$  is written as

$$\omega_n = -\nabla \cdot \hat{\mathbf{V}}_n \int_{p_t}^p h_n dp \tag{6.65}$$

where

$$\nabla \cdot \hat{\mathbf{V}}_n = \left( \frac{\partial \hat{u}_n}{\partial x} + \frac{\partial \hat{v}_n}{\partial y} \right) \tag{6.66}$$

Now  $\omega_n$  at the pressure level  $k$  is denoted by  $\omega_{n,k}$ .

$$\omega_{n,k} = -\nabla \cdot \hat{\mathbf{V}}_n \left\langle \int_{p_t}^p h_n dp \right\rangle_k^p \tag{6.67}$$

The rhs of Eq. (6.67) is expressed as

$$\begin{aligned}
\left\langle \int_{p_t}^p h_n dp \right\rangle_k^p &= \frac{1}{2} \left\{ \left( \int_{p_t}^p h_n dp \right)_{k+1/2} + \left( \int_{p_t}^p h_n dp \right)_{k-1/2} \right\} \\
&= \frac{1}{2} \left\{ \int_{p_{-1/2}}^{p_{k+1/2}} h_n dp + \int_{p_{-1/2}}^{p_{k-1/2}} h_n dp \right\} \\
&= \frac{1}{2} \left\{ \sum_{i=0}^k h_{n,i} \Delta p + \sum_{i=0}^{k-1} h_{n,i} \Delta p \right\} \\
&= \frac{1}{2} h_{n,k} \Delta p + \sum_{i=0}^{k-1} h_{n,i} \Delta p
\end{aligned} \tag{6.68}$$

$\omega_{n,k}$  ( $k = 0, \dots, M$ ) is written as follows.

$$\begin{aligned}
\omega_{n,0} &= -\nabla \cdot \hat{\mathbf{V}}_n \frac{1}{2} h_{n,0} \Delta p \\
\omega_{n,1} &= -\nabla \cdot \hat{\mathbf{V}}_n \left( \frac{1}{2} h_{n,1} + h_{n,0} \right) \Delta p \\
\omega_{n,2} &= -\nabla \cdot \hat{\mathbf{V}}_n \left( \frac{1}{2} h_{n,2} + \sum_{i=0}^1 h_{n,i} \right) \Delta p \\
&\vdots \\
\omega_{n,M} &= -\nabla \cdot \hat{\mathbf{V}}_n \left( \frac{1}{2} h_{n,M} + \sum_{i=0}^{M-1} h_{n,i} \right) \Delta p
\end{aligned} \tag{6.69}$$

### 6.5.3 Heating rate

From Eq. (6.40),  $Q_n$  is written as

$$Q_n = -c_p \hat{D}_n S \int_{p_t}^p h_n dp \tag{6.70}$$

Now  $Q_n$  at the pressure level  $k$  is denoted by  $Q_{n,k}$ .

$$Q_{n,k} = -c_p \hat{D}_n S_k \left\langle \int_{p_t}^p h_n dp \right\rangle_k^p \tag{6.71}$$

$Q_{n,k}$  ( $k = 0, \dots, M$ ) is written as follows.

$$\begin{aligned}
Q_{n,0} &= -c_p \hat{D}_n S_0 \frac{1}{2} h_{n,0} \Delta p \\
Q_{n,1} &= -c_p \hat{D}_n S_1 \left( \frac{1}{2} h_{n,1} + h_{n,0} \right) \Delta p \\
Q_{n,2} &= -c_p \hat{D}_n S_2 \left( \frac{1}{2} h_{n,2} + \sum_{i=0}^1 h_{n,i} \right) \Delta p \\
&\vdots \\
Q_{n,M} &= -c_p \hat{D}_n S_M \left( \frac{1}{2} h_{n,M} + \sum_{i=0}^{M-1} h_{n,i} \right) \Delta p
\end{aligned} \tag{6.72}$$

## 6.6 Budget equations of DSE, moisture, and MSE

In this section, derivation of the budget equations of dry static energy, moisture, and moist static energy is summarized following Yanai et al. (1973). Dry static energy (DSE) is conserved in dry adiabatic process and defined as

$$s = \phi + c_p T \quad (6.73)$$

where  $s$  is DSE,  $\phi = gz$  is geopotential,  $T$  is temperature, and  $c_p$  is dry air heat capacity at constant pressure (1004 J/K/kg).

Budget equations of DSE and moisture are expressed as:

$$\frac{D\bar{s}}{Dt} = \frac{\partial \bar{s}}{\partial t} + \overline{\nabla \cdot s\mathbf{v}} + \frac{\partial \overline{s\omega}}{\partial p} = \overline{Q_R} + L(\bar{c} - \bar{e}) \quad (6.74)$$

$$\frac{D\bar{L}q}{Dt} = \frac{\partial \bar{L}q}{\partial t} + \overline{\nabla \cdot Lq\mathbf{v}} + \frac{\partial \overline{Lq\omega}}{\partial p} = -L(\bar{c} - \bar{e}) \quad (6.75)$$

where  $Q_R$  is radiative heating rate,  $L$  is the latent heat of condensation ( $2.5 \times 10^6$  J/kg),  $q$  is water vapor mixing ratio,  $c$  is the rate of condensation,  $e$  is the rate of re-evaporation of cloud droplets, and over bar represents a horizontal average. Averaging Eqs. (6.74) and (6.75) over the horizontal area, and applying the Reynolds averaging technique (e.g.,  $\overline{AB} = \bar{A}\bar{B} + A'B'$ ) and the continuity equation

$$\overline{\nabla \cdot \mathbf{v}} + \frac{\partial \bar{\omega}}{\partial p} = 0 \quad (6.76)$$

we obtain

$$\frac{\partial \bar{s}}{\partial t} + \bar{\mathbf{v}} \cdot \nabla \bar{s} + \bar{\omega} \frac{\partial \bar{s}}{\partial p} = \overline{Q_R} + L(\bar{c} - \bar{e}) - \nabla \cdot \overline{s'\mathbf{v}'} - \frac{\partial \overline{s'\omega'}}{\partial p} \quad (6.77)$$

$$\frac{\partial \bar{L}q}{\partial t} + \bar{\mathbf{v}} \cdot \nabla \bar{L}q + \bar{\omega} \frac{\partial \bar{L}q}{\partial p} = -L(\bar{c} - \bar{e}) - \nabla \cdot \overline{Lq'\mathbf{v}'} - \frac{\partial \overline{Lq'\omega'}}{\partial p} \quad (6.78)$$

where the prime denotes the deviation from the horizontal average. Ignoring the horizontal eddy terms  $\nabla \cdot \overline{s'\mathbf{v}'}$  and  $\nabla \cdot \overline{Lq'\mathbf{v}'}$ , we finally obtain

$$\frac{\partial \bar{s}}{\partial t} + \bar{\mathbf{v}} \cdot \nabla \bar{s} + \bar{\omega} \frac{\partial \bar{s}}{\partial p} = \overline{Q_R} + L(\bar{c} - \bar{e}) - \frac{\partial \overline{s'\omega'}}{\partial p} \quad (6.79)$$

$$\frac{\partial \bar{L}q}{\partial t} + \bar{\mathbf{v}} \cdot \nabla \bar{L}q + \bar{\omega} \frac{\partial \bar{L}q}{\partial p} = -L(\bar{c} - \bar{e}) - \frac{\partial \overline{Lq'\omega'}}{\partial p} \quad (6.80)$$

The rhs of Eqs. (6.79) and (6.80) are rewritten as

$$Q_1 = \overline{Q_R} + L(\bar{c} - \bar{e}) - \frac{\partial \overline{s'\omega'}}{\partial p} \quad (6.81)$$

$$Q_2 = -L(\bar{c} - \bar{e}) - \frac{\partial \overline{Lq'\omega'}}{\partial p} \quad (6.82)$$

where  $Q_1$  and  $Q_2$  denote the apparent heat source and the apparent moisture sink, respectively. Combining Eqs. (6.79) and (6.80) yields the budget equation of moist static energy (MSE) which is nearly conserved in moist adiabatic process:

$$\frac{\partial \bar{m}}{\partial t} + \bar{\mathbf{v}} \cdot \nabla \bar{m} + \bar{\omega} \frac{\partial \bar{m}}{\partial p} = Q_1 - Q_2 \quad (6.83)$$

where  $m = s + Lq$  is MSE. The rhs in Eq. (6.83) is rewritten as

$$Q_1 - Q_2 = Q_R - \frac{\partial m' \omega'}{\partial p} \quad (6.84)$$

where the second term in the rhs in Eq. (6.84) is vertical eddy transport of MSE which is a measure of the activity of cumulus convection. Hereafter, the over bar is omitted for simplicity.

A mass-weighted vertical integration  $\langle A \rangle$  is defined as

$$\langle A \rangle = \frac{1}{g} \int_{p_t}^{p_s} A dp \quad (6.85)$$

where  $g$  is gravitational accretion,  $p_T$  is pressure at top of the atmosphere, and  $p_s$  is surface pressure. From Eqs. (6.79) and (6.80), the budget equations of vertical integrated DSE and moisture are written as

$$\frac{\partial \langle s \rangle}{\partial t} + \langle \mathbf{v} \cdot \nabla s \rangle + \langle \omega \frac{\partial s}{\partial p} \rangle = \langle Q_R \rangle + LP + SH \quad (6.86)$$

$$\frac{\partial \langle Lq \rangle}{\partial t} + \langle \mathbf{v} \cdot \nabla Lq \rangle + \langle \omega \frac{\partial Lq}{\partial p} \rangle = -LP + LH \quad (6.87)$$

where  $P = \langle L(c - e) \rangle$  is precipitation,  $SH = -\langle \partial s' \omega' / \partial p \rangle$  is surface sensible heat flux, and  $LH = -\langle \partial Lq' \omega' / \partial p \rangle$  is surface latent heat flux (evaporation). Combining Eqs. (6.86) and (6.87) gives

$$\frac{\partial \langle m \rangle}{\partial t} + \langle \mathbf{v} \cdot \nabla m \rangle + \langle \omega \frac{\partial m}{\partial p} \rangle = \langle Q_R \rangle + SH + LH \quad (6.88)$$

The budget equation of vertical integrated MSE is also obtained by mass-weighted vertical integration of Eq. (6.84). Therefore, it is confirmed that

$$\langle Q_1 - Q_2 \rangle = \langle Q_R \rangle + SH + LH \quad (6.89)$$

## 6.7 Vertical MSE advection and a large-scale circulation

Figure 6.1 shows a schematic picture of vertical MSE advection associated with shallow, deep, and stratiform modes (e.g., Peters and Bretherton 2006; Back and Bretherton 2006; Inoue and Back 2015ab; Handlos and Back 2014; Masunaga and L'Ecuyer 2014). A sign of the vertical advection is changed by that of pressure velocity and that of MSE gradient.

For example, we consider the deep mode. Since  $\omega = \Delta p / \Delta t$  is negative in the upward motion,  $\Delta p$  is negative (denoted by upward arrow). Then  $\Delta m = (\partial m) / (\partial p) \Delta p$  is negative (positive) in the lower half of the troposphere (the upper half of the troposphere). Since the vertical advection  $-\omega (\partial m) / (\partial p)$  has an opposite sign to  $\Delta m$ , positive and negative advection occur in the lower and upper half of the troposphere, respectively.

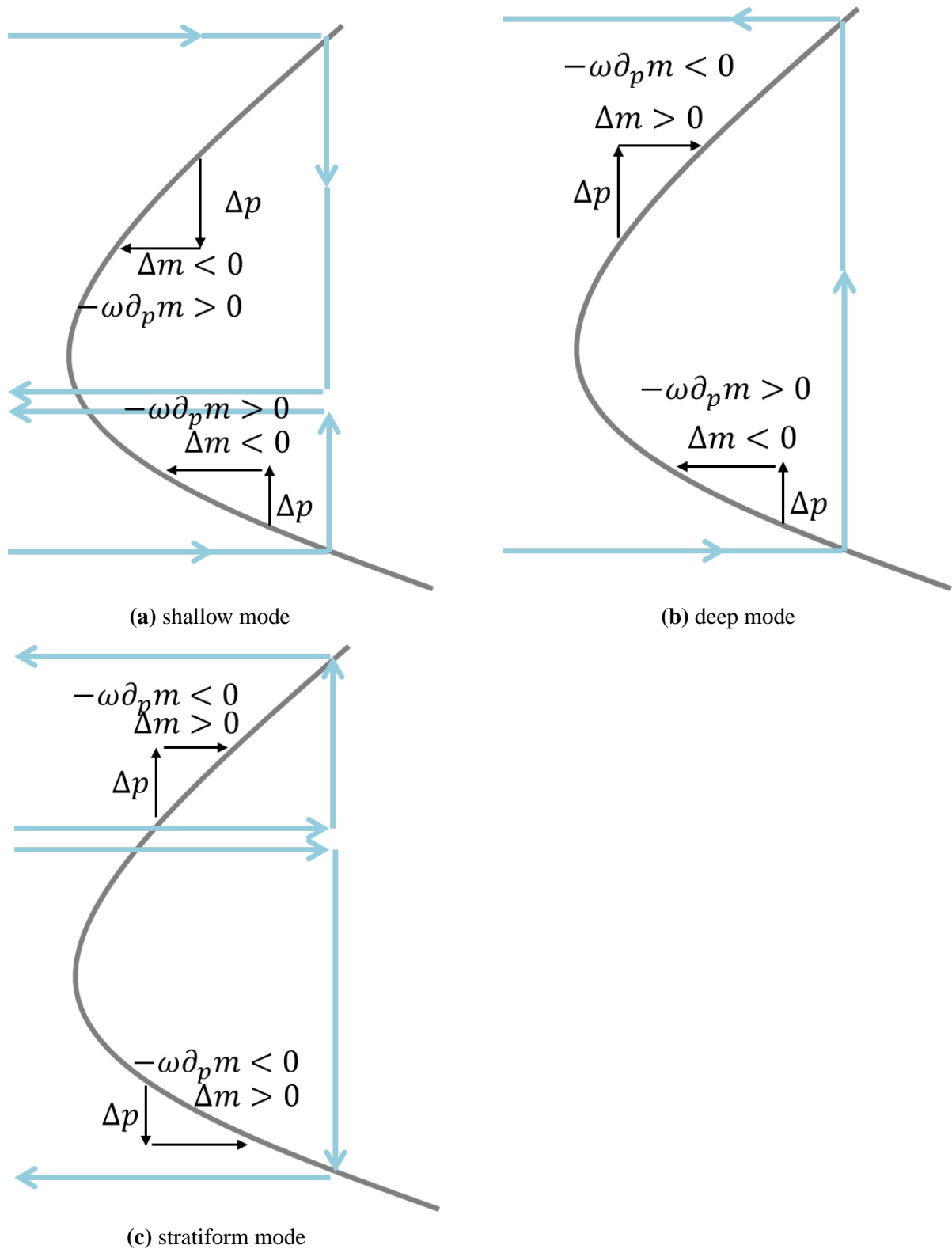


**Fig. 6.1:** Schematic picture of vertical MSE advection for the large-scale circulation (blue line) of (a) shallow mode, (b) deep mode, and (c) stratiform mode. Gray curve represents MSE profile in the tropics.

## References

- Andersen, J. A., and Z. Kuang, 2012: Moist Static Energy Budget of MJO-like Disturbances in the Atmosphere of a Zonally Symmetric Aquaplanet. *J. Climate*, **25**, 2782–2804.
- Back, L. E., and C. S. Bretherton, 2006: Geographic variability in the export of moist static energy and vertical motion profiles in the tropical Pacific. *Geophys. Res. Lett.*, **33**, L17810, doi:10.1029/2006GL026672.
- Back, L. E., and C. S. Bretherton, 2009: On the relationship between sst gradients, boundary layer winds, and convergence over the tropical oceans. *J. Climate*, **22** (15), 4182–4196.
- Benedict, J. J., E. D. Maloney, A. H. Sobel, and D. M. Frierson, 2014: Gross moist stability and MJO simulation skill in three full-physics GCMs. *J. Atmos. Sci.*, **71** (9), 3327–3349.
- Benedict, J. J., and D. A. Randall, 2007: Observed Characteristics of the MJO Relative to Maximum Rainfall. *J. Atmos. Sci.*, **64** (7), 2332–2354.
- Bretherton, C. S., M. E. Peters, and L. E. Back, 2004: Relationships between water vapor path and precipitation over the tropical oceans. *J. Climate*, **17** (7), 1517–1528.
- Chen, S. S., and R. A. Houze, 1997: Diurnal variation and life-cycle of deep convective systems over the tropical pacific warm pool. *Quart. J. Roy. Meteor. Soc.*, **123** (538), 357–388.
- Chen, S. S., R. A. Houze Jr, and B. E. Mapes, 1996: Multiscale variability of deep convection in relation to large-scale circulation in TOGA COARE. *J. Atmos. Sci.*, **53** (10), 1380–1409.
- Ciesielski, P. E., L. M. Hartten, and R. H. Johnson, 1997: Impacts of merging profiler and rawinsonde winds on toga coare analyses. *J. Atmos. Oceanic Technol.*, **14** (6), 1264–1279.
- Clayson, C. A., B. Strahl, and J. Schrage, 2002: 2-3-day convective variability in the tropical western pacific. *Mon. Wea. Rev.*, **130** (3), 529–548.
- Dias, J., and G. N. Kiladis, 2014: Influence of the basic state zonal flow on convectively coupled equatorial waves. *Geophys. Res. Lett.*, **41** (19), 6904–6913.
- Dias, J., and O. Pauluis, 2009: Convectively coupled waves propagating along an equatorial itcz. *J. Atmos. Sci.*, **66** (8), 2237–2255.
- Dias, J., and O. Pauluis, 2011: Modulations of the phase speed of convectively coupled kelvin waves by the itcz. *J. Atmos. Sci.*, **68** (7), 1446–1459.
- Dias, J., S. N. Tulich, and G. N. Kiladis, 2012: An object-based approach to assessing the organization of tropical convection. *J. Atmos. Sci.*, **69** (8), 2488–2504.
- Dias, S., W. H. Schubert, and M. DeMaria, 1983: Large-scale response of the tropical atmosphere to transient convection. *J. Atmos. Sci.*, **40**, 2689–2707.
- Durrant, D. R., 1999: Numerical methods for wave equations in geophysical fluid dynamics.
- Emanuel, K. A., J. David Neelin, and C. S. Bretherton, 1994: On large-scale circulations in convecting atmospheres. *Quart. J. Roy. Meteor. Soc.*, **120** (519), 1111–1143.
- Frierson, D. M., 2007: Convectively coupled kelvin waves in an idealized moist general circulation model. *J. Atmos. Sci.*, **64** (6), 2076–2090.

- Frierson, D. M., A. J. Majda, O. M. Pauluis, and Coauthors, 2004: Large scale dynamics of precipitation fronts in the tropical atmosphere: A novel relaxation limit. *J. Comm. Math. Sci.*, **2** (4), 591–626.
- Fuchs, Ž., and D. J. Raymond, 2007: A simple, vertically resolved model of tropical disturbances with a humidity closure. *Tellus*, **59A** (3), 344–354.
- Fulton, S. R., and W. H. Schubert, 1985: Vertical normal mode transforms: Theory and application. *Mon. Wea. Rev.*, **113** (4), 647–658.
- Gill, A., 1980: Some simple solutions for heat-induced tropical circulation. *Quart. J. Roy. Meteor. Soc.*, **106** (449), 447–462.
- Graham, N., and T. Barnett, 1987: Sea surface temperature, surface wind divergence, and convection over tropical oceans. *Science*, **238** (4827), 657–659.
- Haertel, P. T., and R. H. Johnson, 1998: Two-day disturbances in the equatorial western pacific. *Quart. J. Roy. Meteor. Soc.*, **124** (546), 615–636.
- Haertel, P. T., and G. N. Kiladis, 2004: Dynamics of 2-Day Equatorial Waves. *J. Atmos. Sci.*, **61**, 2707–2721.
- Haertel, P. T., G. N. Kiladis, A. Denno, and T. M. Rickenbach, 2008: Vertical-mode decompositions of 2-day waves and the Madden-Julian oscillation. *J. Atmos. Sci.*, **65** (3), 813–833.
- Handlos, Z. J., and L. E. Back, 2014: Estimating vertical motion profile shape within tropical weather states over the oceans. *J. Climate*, **27** (20), 7667–7686.
- Hannah, W. M., and E. D. Maloney, 2011: The Role of Moisture-Convection Feedbacks in Simulating the Madden-Julian Oscillation. *J. Climate*, **24**, 2754–2770.
- Hannah, W. M., and E. D. Maloney, 2014: The moist static energy budget in near cam5 hindcasts during dynamo. *Journal of Advances in Modeling Earth Systems*, **6** (2), 420–440.
- Hartmann, D. L., 2015: *Global physical climatology*, Vol. 103. Newnes.
- Holloway, C. E., and J. D. Neelin, 2009: Moisture vertical structure, column water vapor, and tropical deep convection. *J. Atmos. Sci.*, **66** (6), 1665–1683.
- Houze, R. A., 2004: Mesoscale convective systems. *Rev. Geophys.*, **42** (4), 4003, doi: 10.1029/2004RG000150.
- Iguchi, T., T. Kozu, R. Meneghini, J. Awaka, and K. Okamoto, 2000: Rain-profiling algorithm for the TRMM precipitation radar. *J. Appl. Meteor.*, **39** (12), 2038–2052.
- Inoue, K., and L. Back, 2015a: Column-integrated Moist Static Energy Budget Analysis on Various Time Scales during TOGA COARE. *J. Atmos. Sci.*, **72**, 1856–1871.
- Inoue, K., and L. E. Back, 2015b: Gross moist stability assessment during toga coare: Various interpretations of gross moist stability. *J. Atmos. Sci.*, **72** (11), 4148–4166.
- Janowiak, J. E., R. J. Joyce, and Y. Yarosh, 2001: A real-time global half-hourly pixel-resolution infrared dataset and its applications. *Bull. Amer. Meteor. Soc.*, **82** (2), 205–217.
- Johnson, R. H., T. M. Rickenbach, S. A. Rutledge, P. E. Ciesielski, and W. H. Schubert, 1999: Trimodal characteristics of tropical convection. *J. Climate*, **12** (8), 2397–2418.
- Kasahara, A., and K. Puri, 1981: Spectral representation of three-dimensional global data by expansion in normal mode functions. *Mon. Wea. Rev.*, **109** (1), 37–51.

- Khouider, B., and A. B. Majda, 2006a: A simple multicloud parameterization for convectively coupled tropical waves. part :linear analysis. *J. Atmos. Sci.*, **63** (3), 1308–1323.
- Khouider, B., and A. J. Majda, 2006b: Multicloud convective parametrizations with crude vertical structure. *Theor. Comput. Fluid Dyn.*, **20** (5-6), 351–375.
- Kikuchi, K., 2014: An introduction to combined fourier–wavelet transform and its application to convectively coupled equatorial waves. *Climate Dyn.*, **43** (5-6), 1339–1356.
- Kikuchi, K., and Y. N. Takayabu, 2004: The development of organized convection associated with the MJO during TOGA COARE IOP: Trimodal characteristics. *Geophys. Res. Lett.*, **31** (10), 10 101, doi:10.1029/2004GL019601.
- Kiladis, G. N., C. D. Thorncroft, and N. M. Hall, 2006: Three-dimensional structure and dynamics of african easterly waves. part i: Observations. *J. Atmos. Sci.*, **63** (9), 2212–2230.
- Kiladis, G. N., M. C. Wheeler, P. T. Haertel, K. H. Straub, and P. E. Roundy, 2009: Convectively coupled equatorial waves. *Rev. Geophys.*, **47** (2), 2003, doi:10.1029/2008RG000266.
- Kim, D., J.-S. Kug, and A. H. Sobel, 2014: Propagating versus nonpropagating madden–julian oscillation events. *J. Climate*, **27** (1), 111–125.
- Kiranmayi, L., and E. D. Maloney, 2011: Intraseasonal moist static energy budget in reanalysis data. *J. Geophys. Res.*, **116** (D21), doi:10.1029/2011JD016031.
- Kuang, Z., 2008a: Modeling the Interaction between Cumulus Convection and Linear Gravity Waves Using a Limited-Domain Cloud System-Resolving Model. *J. Atmos. Sci.*, **65**, 576–591.
- Kuang, Z., 2008b: A moisture-stratiform instability for convectively coupled waves. *J. Atmos. Sci.*, **65** (3), 834–854.
- Kuang, Z., 2011: The Wavelength Dependence of the Gross Moist Stability and the Scale Selection in the Instability of Column-Integrated Moist Static Energy. *J. Atmos. Sci.*, **68**, 61–74.
- Madden, R. A., and P. R. Julian, 1971: Detection of a 40-50 day oscillation in the zonal wind in the tropical pacific. *J. Atmos. Sci.*, **28** (5), 702–708.
- Madden, R. A., and P. R. Julian, 1972: Description of global-scale circulation cells in the tropics with a 40-50 day period. *J. Atmos. Sci.*, **29** (6), 1109–1123.
- Majda, A. J., B. Khouider, G. N. Kiladis, K. H. Straub, and M. G. Shefter, 2004: A model for convectively coupled tropical waves: Nonlinearity, rotation, and comparison with observations. *J. Atmos. Sci.*, **61** (17), 2188–2205.
- Majda, A. J., and M. G. Shefter, 2001: Models for stratiform instability and convectively coupled waves. *J. Atmos. Sci.*, **58** (12), 1567–1584.
- Maloney, E. D., 2009: The Moist Static Energy Budget of a Composite Tropical Intraseasonal Oscillation in a Climate Model. *J. Climate*, **22**, 711–729.
- Maloney, E. D., A. H. Sobel, and W. M. Hannah, 2010: Intraseasonal variability in an aquaplanet general circulation model. *J. Adv. Model. Earth Syst.*, **2** (2), 5, doi:10.3894/JAMES.2010.2.5.
- Mapes, B., S. Tulich, J. Lin, and P. Zuidema, 2006: The mesoscale convection life cycle: Building block or prototype for large-scale tropical waves? *Dyn. Atmos. Oceans*, **42**, 3–29.
- Mapes, B. E., 1998: The large-scale part of tropical mesoscale convective system circulations: A linear vertical spectral band model. *J. Meteor. Soc. Japan*, **76** (1), 29–55.

- Mapes, B. E., 2000: Convective Inhibition, Subgrid-Scale Triggering Energy, and Stratiform Instability in a Toy Tropical Wave Model. *J. Atmos. Sci.*, **57**, 1515–1535.
- Mapes, B. E., and R. A. Houze Jr, 1995: Diabatic divergence profiles in western pacific mesoscale convective systems. *J. Atmos. Sci.*, **52** (10), 1807–1828.
- Masunaga, H., 2012a: A satellite study of the atmospheric forcing and response to moist convection over tropical and subtropical oceans. *J. Atmos. Sci.*, **69** (1), 150–167.
- Masunaga, H., 2012b: Short-term versus climatological relationship between precipitation and tropospheric humidity. *J. Climate*, **25** (22), 7983–7990.
- Masunaga, H., and T. S. L’Ecuyer, 2014: A mechanism of tropical convection inferred from observed variability in the moist static energy budget. *J. Atmos. Sci.*, **71** (10), 3747–3766.
- Masunaga, H., T. S. L’Ecuyer, and C. D. Kummerow, 2006: The madden-julian oscillation recorded in early observations from the tropical rainfall measuring mission (trmm). *J. Atmos. Sci.*, **63** (11), 2777–2794.
- Matsuno, T., 1966: Quasi-geostrophic motions in the equatorial area. *J. Meteor. Soc. Japan*, **44**, 25–43.
- Nakazawa, T., 1988: Tropical super clusters within intraseasonal variations over the western pacific. *J. Meteor. Soc. Japan*, **66**, 823–839.
- Neelin, J. D., and I. M. Held, 1987: Modeling tropical convergence based on the moist static energy budget. *Mon. Wea. Rev.*, **115** (1), 3–12.
- Neelin, J. D., O. Peters, and K. Hales, 2009: The transition to strong convection. *J. Atmos. Sci.*, **66** (8), 2367–2384.
- Neelin, J. D., and J.-Y. Yu, 1994: Modes of tropical variability under convective adjustment and the madden-julian oscillation. part i: Analytical theory. *J. Atmos. Sci.*, **51** (13), 1876–1894.
- Peters, M. E., and C. S. Bretherton, 2006: Structure of tropical variability from a vertical mode perspective. *Theor. Comput. Fluid Dyn.*, **20**, 501–524.
- Peters, O., and J. D. Neelin, 2006: Critical phenomena in atmospheric precipitation. *Nature Physics*, **2** (6), 393–396.
- Raymond, D. J., and Ž. Fuchs, 2007: Convectively coupled gravity and moisture modes in a simple atmospheric model. *Tellus*, **59A** (5), 627–640.
- Raymond, D. J., S. L. Sessions, A. H. Sobel, and Ž. Fuchs, 2009: The mechanics of gross moist stability. *J. Adv. Model. Earth Syst.*, **1** (3).
- Roundy, P. E., 2008: Analysis of convectively coupled kelvin waves in the indian ocean mjo. *J. Atmos. Sci.*, **65** (4), 1342–1359.
- Roundy, P. E., and W. M. Frank, 2004: A Climatology of Waves in the Equatorial Region. *J. Atmos. Sci.*, **61**, 2105–2132.
- Schumacher, C., and R. A. Houze Jr, 2003: Stratiform rain in the tropics as seen by the trmm precipitation radar\*. *J. Climate*, **16** (11), 1739–1756.
- Schumacher, C., R. A. Houze Jr, and I. Kraucunas, 2004: The tropical dynamical response to latent heating estimates derived from the trmm precipitation radar. *J. Atmos. Sci.*, **61** (12), 1341–1358.
- Sessions, S. L., S. Sugaya, D. J. Raymond, and A. H. Sobel, 2010: Multiple equilibria in a cloud-resolving model using the weak temperature gradient approximation. *J. Geophys. Res.*, **115**, 12 110, doi:10.1029/2009JD013376.

- Sherwood, S. C., 1999: Convective precursors and predictability in the tropical western Pacific. *Mon. Wea. Rev.*, **127** (12), 2977–2991.
- Simmons, A., S. Uppala, D. Dee, and S. Kobayashi, 2007: ERA-Interim: New ECMWF reanalysis products from 1989 onwards. *ECMWF newsletter*, **110** (110), 25–35.
- Sobel, A., S. Wang, and D. Kim, 2014: Moist static energy budget of the MJO during DYNAMO. *J. Climate*, **71**, 4276–4291.
- Sobel, A. H., 2002: Water vapor as an active scalar in tropical atmospheric dynamics. *Chaos*, **12** (2), 451–459.
- Sobel, A. H., and C. S. Bretherton, 2003: Large-scale waves interacting with deep convection in idealized mesoscale model simulations. *Tellus*, **55A** (1), 45–60.
- Sobel, A. H., J. Nilsson, and L. M. Polvani, 2001: The Weak Temperature Gradient Approximation and Balanced Tropical Moisture Waves\*. *J. Atmos. Sci.*, **58** (23), 3650–3665.
- Stechmann, S. N., and A. J. Majda, 2009: Gravity waves in shear and implications for organized convection. *J. Atmos. Sci.*, **66** (9), 2579–2599.
- Straub, K. H., and G. N. Kiladis, 2002: Observations of a convectively coupled kelvin wave in the eastern pacific itcz. *J. Atmos. Sci.*, **59** (1), 30–53.
- Straub, K. H., and G. N. Kiladis, 2003: The observed structure of convectively coupled kelvin waves: Comparison with simple models of coupled wave instability. *J. Atmos. Sci.*, **60** (14), 1655–1668.
- Sumi, Y., and H. Masunaga, 2016: A moist static energy budget analysis of quasi-2-day waves using satellite and reanalysis data. *J. Atmos. Sci.*, **73** (4), 743–759.
- Takayabu, Y., 1994a: Large-scale cloud disturbances associated with equatorial waves. I: Spectral features of the cloud disturbances. *J. Meteor. Soc. Japan*, **72** (3), 433–449.
- Takayabu, Y., 1994b: Large-scale cloud disturbances associated with equatorial waves. Part II: Westward-propagating inertio-gravity waves. *J. Meteor. Soc. Japan*, **72**, 451–465.
- Takayabu, Y., K.-M. Lau, and C.-H. Sui, 1996: Observation of a quasi-2-day wave during TOGA COARE. *Mon. Wea. Rev.*, **124**, 1892–1913.
- Tian, B., and V. Ramanathan, 2003: A simple moist tropical atmosphere model: The role of cloud radiative forcing. *J. Climate*, **16** (12), 2086–2092.
- Tulich, S. N., and G. N. Kiladis, 2012: Squall Lines and Convectively Coupled Gravity Waves in the Tropics: Why Do Most Cloud Systems Propagate Westward? *J. Atmos. Sci.*, **69**, 2995–3012.
- Tulich, S. N., and B. E. Mapes, 2008: Multiscale convective wave disturbances in the tropics: Insights from a two-dimensional cloud-resolving model. *J. Atmos. Sci.*, **65** (1), 140–155.
- Tulich, S. N., and B. E. Mapes, 2010: Transient environmental sensitivities of explicitly simulated tropical convection. *J. Atmos. Sci.*, **67** (4), 923–940.
- Tulich, S. N., D. A. Randall, and B. E. Mapes, 2007: Vertical-mode and cloud decomposition of large-scale convectively coupled gravity waves in a two-dimensional cloud-resolving model. *J. Atmos. Sci.*, **64** (4), 1210–1229.
- Waliser, D. E., N. E. Graham, and C. Gautier, 1993: Comparison of the highly reflective cloud and outgoing longwave radiation datasets for use in estimating tropical deep convection. *J. Climate*, **6** (2), 331–353.

- Wheeler, M., and G. N. Kiladis, 1999: Convectively Coupled Equatorial Waves: Analysis of Clouds and Temperature in the Wavenumber-Frequency Domain. *J. Atmos. Sci.*, **56**, 374–399.
- Wheeler, M., G. N. Kiladis, and P. J. Webster, 2000: Large-Scale Dynamical Fields Associated with Convectively Coupled Equatorial Waves. *J. Atmos. Sci.*, **57**, 613–640.
- Yanai, M., S. Esbensen, and J.-H. Chu, 1973: Determination of bulk properties of tropical cloud clusters from large-scale heat and moisture budgets. *J. Atmos. Sci.*, **30** (4), 611–627.
- Yang, G.-Y., B. Hoskins, and J. Slingo, 2003: Convectively coupled equatorial waves: A new methodology for identifying wave structures in observational data. *J. Atmos. Sci.*, **60**, 1637–1654.
- Yang, G.-Y., B. Hoskins, and J. Slingo, 2007a: Convectively coupled equatorial waves. part i: Horizontal and vertical structures. *J. Atmos. Sci.*, **64** (10), 3406–3423.
- Yang, G.-Y., B. Hoskins, and J. Slingo, 2007b: Convectively coupled equatorial waves. part ii: Propagation characteristics. *J. Atmos. Sci.*, **64** (10), 3424–3437.
- Yano, J.-I., and K. Emanuel, 1991: An improved model of the equatorial troposphere and its coupling with the stratosphere. *J. Atmos. Sci.*, **48** (3), 377–389.
- Yasunaga, K., and B. Mapes, 2012: Differences between More Divergent and More Rotational Types of Convectively Coupled Equatorial Waves. Part I: Space-Time Spectral Analyses. *J. Atmos. Sci.*, **69**, 3–16.
- Yasunaga, K., and B. Mapes, 2014: Differences between faster versus slower components of convectively coupled equatorial waves. *J. Atmos. Sci.*, **71**, 98–111.
- Zhang, C., 1993: Large-scale variability of atmospheric deep convection in relation to sea surface temperature in the tropics. *J. Climate*, **6** (10), 1898–1913.